


March 2016

## **Solution, Interfacial, and Interlayer Studies of Electronically Active Polymers**

Hsin-Wei Wang  
*University of Massachusetts - Amherst*

Follow this and additional works at: [https://scholarworks.umass.edu/dissertations\\_2](https://scholarworks.umass.edu/dissertations_2)

 Part of the [Polymer and Organic Materials Commons](#), [Semiconductor and Optical Materials Commons](#), and the [Structural Materials Commons](#)

---

### **Recommended Citation**

Wang, Hsin-Wei, "Solution, Interfacial, and Interlayer Studies of Electronically Active Polymers" (2016).  
*Doctoral Dissertations*. 604.  
[https://scholarworks.umass.edu/dissertations\\_2/604](https://scholarworks.umass.edu/dissertations_2/604)

This Open Access Dissertation is brought to you for free and open access by the Dissertations and Theses at ScholarWorks@UMass Amherst. It has been accepted for inclusion in Doctoral Dissertations by an authorized administrator of ScholarWorks@UMass Amherst. For more information, please contact [scholarworks@library.umass.edu](mailto:scholarworks@library.umass.edu).

**SOLUTION, INTERFACIAL, AND INTERLAYER STUDIES  
OF ELECTRONICALLY ACTIVE POLYMERS**

A Dissertation Presented

by

HSIN-WEI WANG

Submitted to the Graduate School of the  
University of Massachusetts Amherst in partial fulfillment  
of the requirements for the degree of

DOCTOR OF PHILOSOPHY

February 2016

Polymer Science and Engineering

© Copyright by Hsin-Wei Wang 2016

All Rights Reserved

**SOLUTION, INTERFACIAL, AND INTERLAYER STUDIES  
OF ELECTRONICALLY ACTIVE POLYMERS**

A Dissertation Presented

by

HSIN-WEI WANG

Approved as to style and content by:

---

Todd Emrick, Co-chair

---

Thomas P. Russell, Co-chair

---

Michael M. Barnes, Member

---

David Hoagland, Department Head  
Polymer Science and Engineering

## ACKNOWLEDGEMENTS

I would like to thank my advisors, Professor Thomas Russell and Professor Todd Emrick for their mentoring and guidance, and my committee member, Professor Michael Barnes for his valuable suggestions and advice. During my thesis work, I have been fortunate to engage in both the physical and chemistry sides of material science. Although co-advisement has its ups and downs, it has been a great pleasure to be a member of both research groups. I am thankful for the opportunity to work with a great number of highly motivated lab members, and to mature as an independent researcher. It was really exciting to participate in a frontier research of polymer science, witnessing the conceived projects to grow and evolve over time.

I would like to extend my gratitude to my collaborators, without whom this thesis would not be possible: Chia-Chih Chang, Dr. Dean DeLongchamp, Dr. Vlodymyr Dzuhko, Dr. Feng Liu, Dr. Yao Liu, Dr. Dennis Nordlund, Dr. Emily Pentzer, Dr. Egle Puodziukynaite, and Dr. Adam Wise. They taught me the art of collaboration, and the importance of teamwork. I have learned many precious lessons from them, and those experiences shaped who I am today.

I would also like to thank the past and present group members, class 2010, and my dear “Conte friends”, who helped me, both physically and mentally, to survive the painful Ph.D. program. I would not be here without supports from them. Specifically, I would like to express my gratitude toward Dr. Yu Gu, Dr. Caroline Miesch, Dr. Sirinya Chantarak, Dr. Sunzida Ferdous for brightening up my earlier days; Minchao Zhang, Mengmeng Cui, Tao Feng, Gajin Jeong for enduring encouragements; Hyeyoung Kim, and Jaewon Choi for helping with the lab safety

and sharing the group responsibility; Tetsu Ouchi and Jooyoung Chang for food hunting; Dr. Daniel King, Chia-Chih Chang, Rachel Letteri, Brittany DeRonde, Kyle Bryson, Dr. Jon Pham, Anand Rahalkar, Rohit Kothari, for the laughter and tears we shared along the way. It was an honor to be in the class 2010 and surrounded by highly motivated individuals: a stimulating experience that will not fade over time.

Lastly, I would like to thank my family and Dr. Jimmy Lawrence, who have never forsaken me despite my lack of patience, sensitivity and sometimes, rationale; who always care about my well-being despite our arguments and quarrels; and who have been embracing my rebelliousness with kindness, trust and hope.

## **ABSTRACT**

### **SOLUTION, INTERFACIAL, AND INTERLAYER STUDIES OF ELECTRONICALLY ACTIVE POLYMERS**

FEBRUARY 2016

HSIN-WEI WANG, B.S., NATIONAL TSING-HUA UNIVERSITY, TAIWAN, R.O.C.

M.S., UNIVERSITY OF MASSACHUSETTS AMHERST

Ph.D., UNIVERSITY OF MASSACHUSETTS AMHERST

Directed by: Professor Todd Emrick and Professor Thomas P. Russell

This thesis describes the solution behavior and interfacial properties of electronically active polymers. The performance of such polymers in devices is often determined by their chain conformation and morphology in solution and in thin films. For example, the intricate balance between polymer domain size and crystalline packing of electron donor and acceptor components, as well as the properties at the polymer-metal interface, are crucial for achieving optimal performance in devices, such as solar cells.

Chapter 1 presents the current progress in polymer-based solar cells, their fundamental principles, and key factors to improve their efficiency. Literature precedents on the development of materials for the active layer and electrode modifiers are also described in detail.

Chapter 2 centers on the solution-driven assembly of a low band gap polymer (PCDTBT) in a marginal solvent to give semicrystalline nanofibers. In contrast to poly(3-alkylthiophene) nanowires prepared by similar techniques, these truncated nanostructures showed undulated features along the fiber axis. Such

morphology suggested the nanofibers were formed from packing of smaller crystalline units, giving valuable insight into the ordering of conjugated polymers in solution-processed thin films.

Chapter 3 highlights zwitterionic polymers bearing pendent azulene groups with unique optoelectronic properties. The orthogonal solubility of these polar copolymers is enabling for multilayer device fabrication, and proving useful for improved charge collection efficiency, affording high performance solar cells.

Chapter 4 describes sulfobetaine (SB) and phosphorylcholine (PC) functionalized zwitterionic poly(acetylene)s (ZIPAs). SB ZIPA proved amenable to nanofiber formation in solution upon addition of a non-solvent, while PC ZIPA remained well-solvated under similar conditions. Both of these polymers significantly reduced the work function of silver, rendering ZIPAs as promising cathode modifiers. Upon incorporating into polymer-based solar cells, the power conversion efficiency significantly increased from 2.5 % to 9.2%.

Lastly, chapter 5 summarizes the thesis and presents a perspective for utilizing interlayer materials to enhance the stability and lifetime of future solar cells. A recent work on employing zwitterionic nanoparticles as interlayer materials is discussed with preliminary results presented in the appendix.



## TABLE OF CONTENTS

	Page
ACKNOWLEDGEMENTS .....	iv
ABSTRACT .....	vi
LIST OF TABLES .....	x
LIST OF FIGURES .....	xi
LIST OF SCHEMES .....	xvi
CHAPTER	
1. CONJUGATED POLYMERS AND POLYMER-BASED SOLAR CELLS (PSCS) .....	1
1.1 Current Progress on Polymer-Based Solar Cells (PSCs) .....	1
1.2 PSC Operation Mechanism and Material Designs .....	3
1.3 Conjugated Polymers in Solution, and as Thin Films: Impact on Device Performance .....	8
1.4 Electrode Interfaces Engineering .....	12
1.5 Thesis Outline .....	19
1.6 References .....	20
2. PREPARATION OF SEMI-CRYSTALLINE PCDTBT NANOFIBERS THROUGH SOLVENT-INDUCED CRYSTALLIZATION .....	26
2.1 Introduction .....	26
2.2 PCDTBT: from Synthesis to Preparation of Nanofibers .....	28
2.3 Characterization of PCDTBT Nanofibers .....	31
2.4 PCDTBT Derivatives and Their Nanofibers .....	37
2.5 Impact of PCBM on PCDTBT Nanofibers .....	40
2.6 Conclusions .....	43
2.7 References .....	44
3. ZWITTERIONIC METHACRYLATE AND AZULENE COPOLYMERS .....	47
3.1 Introduction .....	47
3.2 Polysulfobetaine Methacrylate (PSBMA) as Cathode Modifiers .....	49

3.3	Azulene Copolymers: Synthesis and Cathode Modification.....	55
3.4	Conclusions .....	58
3.5	References .....	60
4.	SULFOBETAINE AND PHOSPHORYLCHOLINE ZWITTERIONIC POLYACEYTLLENES (ZIPAS).....	64
4.1	Introduction.....	64
4.2	Preparation and Characterization of ZIPAs .....	66
4.3	Solution-driven Assembly of ZIPAs .....	69
4.4	Electronic Properties of ZIPA films at Silver Interface.....	73
4.5	ZIPAs as Cathode Modifiers in PSCs .....	77
4.6	Conclusions .....	81
4.7	References .....	82
5.	SUMMARY AND OUTLOOK.....	84
6.	EXPERIMENTAL PROCEDURES.....	86
6.1	Preparation of PCDTBT Nanofibers .....	86
6.2	Solar Cell Fabrication Procedures .....	87
6.2.1	PSCs with azulene copolymers as the cathode interlayer .....	87
6.2.2	Devices with ZIPA as the cathode interlayer .....	88
6.3	Measuring Power Conversion Efficiency of Solar Cells.....	88
6.4	Instrumentation.....	89
6.4.1	Polymer molecular weight determination .....	89
6.4.2	Thermal analysis.....	89
6.4.3	Optical and electronic properties analysis.....	89
6.4.4	Morphology characterization.....	90
6.4.5	Interface characterization .....	90
	APPENDIX: UTILIZING GOLD NANOPARTICLES AS ELECTRODE MODIFIERS.....	92
	BIBLIOGRAPHY .....	95

## LIST OF TABLES

Table	Page
2.1 Summary of polymerization results for PCDTBT .....	29
4.1 Summary of synthesized ZIPA-PC and ZIPA-SB from M1 and M2, respectively .....	68
4.2 Summary of electronic energy levels of ZIPAs at Ag interfaces .....	75
4.3 XPS atomic analysis of the active layer surfaces before and after EGME washing.....	79
4.4 Summary of device performances.....	80

## LIST OF FIGURES

Figure	Page
1.1 The dark current ( <i>black</i> ) and the IV response of PSCs under light ( <i>red</i> ). $J_{sc}$ is the current measured at no external bias, $V_{oc}$ is the maximum potential generated by the cell, and the ratio of maximum device power ( $J_m \times V_m$ ) to the product of $J_{sc}$ and $V_{oc}$ (the ratio of blue to orange area) gives the fill factor (FF).....	4
1.2 A typical photovoltaic process in PSCs starts with (a) light generating an exciton, which diffuses to the donor-acceptor interface where (b) charge separates into electrons and holes. These free charge carriers are then (c) driven by the built-in potential to travel to the corresponding electrodes.....	5
1.3 Photon flux at AM1.5 as a function of wavelength ( <i>black line</i> ). The integrated number of photons and the corresponding obtainable current density is shown in red. <sup>13</sup> .....	7
1.4 Chemical structures of common donor polymers and fullerene acceptors used in PSCs.....	7
1.5 (a) Bilayer device and (b) bulk heterojunction (BHJ) device configurations. The white and maroon domains represent the donor and the acceptor components, respectively...	9
1.6 SEM images showing the cross-section of PPV/PC <sub>61</sub> BM films processed from (a) chlorobenzene, and (b) toluene. <sup>22</sup> TEM images of PPV/PC <sub>61</sub> BM films with (c) 60 wt % and (d) 90 wt % of PC <sub>61</sub> BM. <sup>28</sup> .....	10
1.7 TEM images of pDPP/PC <sub>71</sub> BM based active layer prepared from (a) chloroform (host solvent), and (b) a co-solvent of chloroform:chlorobenzene at 4:1 volume ratio. <sup>29</sup> Similar trends were observed in PTB7/PC <sub>71</sub> BM — (c) prepared from chlorobenzene (CB) (host) and (d) a co-solvent of CB and 1,8-diiodooctane at 3 vol % as the additive. <sup>30,31</sup> .....	11
1.8 TEM images of (a) P3HT nanowires prepared from dichloromethane, (b) P3HT nanowires blended with PC <sub>61</sub> BM. (c) Hole-electron mobility of solar cells composed of PC <sub>61</sub> BM/P3HT nanowires, prepared from various aging time in dichloromethane. <sup>43</sup> .....	12

1.9	The WF difference between anode and cathode establishes a potential bias across the cell. This is analogous to (b) potential difference between the beakers causing water flowing through the connection. (c) The energy diagram upon reaching equilibrium.....	13
1.10	The effect of dipole orientation on work function of Ag with corresponding energy diagrams. (a) Dipoles pointing away and (b) toward Ag. <sup>58</sup> .....	15
1.11	(a) Experimental setup to measure surface potential. (b) The topology and (c) the surface potential of the active layer without ( <i>left</i> ) and with PFN ( <i>right</i> ) measured by scanning Kelvin probe microscopy.....	17
1.12	Examples of polymeric electrode modifiers with (a) amines and ethers functionalities, (b) conjugated polyelectrolytes, and (c) conjugated polyzwitterions. ....	19
2.1	TEM images of drop cast solution of PCDTBT prepared by (a) heating in anisole (120 °C) and cooling to RT, (b) heating in <i>p</i> -xylene (120 °C) and cooling to RT, (c) dissolving in chloroform and then diluting with anisole.....	30
2.2	TEM image of PCDTBT nanofibers prepared from Scheme 2. The corresponding GI-WAXS data ( <i>right</i> ) indicates these structures are semicrystalline with lattice spacings comparable to bulk PCDTBT.....	31
2.3	AFM images of PCDTBT nanofibers showing granular texture along the fiber axis. Similar crystalline texture was also observed in crystalline isotactic polypropylenes (lower right).....	33
2.4	AFM height ( <i>left</i> ) and phase ( <i>right</i> ) images showing the disappearance of granular structures after annealing at 260 °C for 30 min. ....	33
2.5	Nanostructures of PCDTBT ( $M_n = 55$ kDa, $\bar{D} = 1.55$ ) after (a) 3 min, (b) 1 day aging, and (c) PCDTBT ( $M_n = 20$ kDa and $\bar{D} = 2.1$ ) nanofibers solution after 1-day aging in ambient. ....	34
2.6	PCDTBT nanofibers (0.05 mg/mL) after quenched to room temperature and aged for (a) 3 min and (b) 1 day. ....	36
2.7	(a) UV/Vis and (b) photoluminescence spectra of solvated PCDTBT in chloroform ( <i>black</i> ) and PCDTBT nanofibers in DCM ( <i>red</i> ). ....	37
2.8	(a) UV/Vis spectra of PCD <sup>6</sup> TBT in chlorobenzene ( <i>black</i> ) and PCD <sup>6</sup> TBT nanostructures in DCM ( <i>red</i> ). TEM images showing (b) PCD <sup>6</sup> TBT nanofibers, and (c) PCD <sup>6</sup> TBT nanosheets.....	39

2.9	(a) UV/Vis spectra of PCD <sup>8,12</sup> TBT in chlorobenzene ( <i>black</i> ) and PCD <sup>8,12</sup> TBT nanostructures ( <i>red</i> ) in DCM. (b) TEM and (c) AFM images of PCD <sup>8,12</sup> TBT nanocoils and nanofibers. ....	40
2.10	GI-WAXS and TEM of PCDTBT fibers before and after blending with PCBM at weight ratios of 1:2 and 1:4. Increasing PCBM concentration diminished the (100) and (010) reflections. ....	42
2.11	<i>In situ</i> GI-WAXS profiles of the bilayer film composed of semicrystalline PCDTBT ( <i>top layer</i> ) and PCBM ( <i>bottom layer</i> ) from room temperature to 160°C at 5°C/min. As (100) and (200) peaks of PCDTBT disappear, the PCBM reflection increased in intensity. ....	43
3.1	(a) A typical UPS spectrum of Ag showing the secondary electron energy cutoff ( $E_{\text{Sec, Ag}}$ ), Fermi level ( $E_{\text{F, Ag}}$ ) and the vacuum level ( $E_{\text{Vac}}$ ). The difference between $E_{\text{Vac}}$ and $E_{\text{F, Ag}}$ gives the work function of Ag ( $\Phi_{\text{Ag}} = -4.5$ eV). (b) Overlaying UPS spectra obtained from Ag and PSBMA/Ag substrates showed a shift in $E_{\text{Sec}}$ . ....	51
3.2	Normalized XPS spectra showing (a) C(1s) and (b) Ag(3d) signals from Ag ( <i>black</i> ) and PSBMA/Ag ( <i>red</i> ) substrate. ....	52
3.3	(a) UPS spectra of Ag ( <i>black</i> ) and PSBMA/Ag ( <i>red</i> ) showed $E_{\text{Sec}}$ shifted to higher binding energy by ~1 eV. (b) UPS spectra showing the $E_{\text{Sec}}$ values of both PMMA/Ag and PnBMA/Ag are comparable to that of PSBMA/Ag. ....	52
3.4	(a) Device configuration (inset: chemical structures of PTB7 (donor), PC <sub>71</sub> BM (acceptor), and PSBMA (cathode modifier)). (b) The representative IV curves of unmodified ( <i>black</i> ) and PSBMA-modified ( <i>red</i> ) PSCs. ....	53
3.5	(a) Cyclopentadienyl anion and trophium cation resonance contributed to the vibrant blue color of azulene as found in <i>Lactarius indigo</i> mushrooms. (b) Synthetic routes to azulene containing sulfobetaine copolymers. ....	56
3.6	UPS spectra of (a) PATSB/Ag and (b) PASB/Ag substrates. PATSB1, PATSB2, and PATSB3 have an azulene composition of 25, 50 and 75 mol %. PASB1 and PASB2 have 25 and 50 mol % of azulene, respectively. ....	57
3.7	(a) Device configuration and the chemical structure of PASB (cathode modifier). (b) Representative IV curves of PASBs modified devices. (c) No obvious trend was observed between the device performance and degree of work function reduction at the cathode interface. ....	59

3.8	(a) Device configuration and the chemical structure of PATSB. (b) Representative IV curves of PATSBs modified solar cells. (c) Work function reduction of the electrode was found not correlate to the device efficiency.....	60
3.9	AFM height images showing the device PCEs increase with the film quality of PASBs and PATSBs interlayer. Scale bars 1 $\mu\text{m}$ .....	60
4.1	(a) Synthetic route to 1,6-heptadiyne monomers with PC ( <b>3</b> ) and SB ( <b>6</b> ) functionalities. (b) $^{13}\text{C}$ NMR spectra of ZIPA-PC in $\text{MeOD-}d_4$ . The inset shows a representative GPC trace of ZIPA-PC. ....	67
4.2	$^{13}\text{C}$ NMR spectra of (a) ZIPA-SB and (b) ZIPA-PC in $\text{TFE-}d_6$ . Peaks between 120-130 ppm and at 60 ppm are from TFE. ....	67
4.3	(a) TGA traces of ZIPA-SB ( <i>black</i> ) and ZIPA-PC ( <i>red</i> ) showing the polymers are thermal stable up to 240 $^{\circ}\text{C}$ . (b) DSC traces showing the $T_g$ of ZIPA-PC is at $\sim 95$ $^{\circ}\text{C}$ .....	69
4.4	TEM images showing the evolution of ZIPA-SB nanostructures in 100 $\mu\text{L}$ of ZIPA-SB at 1 mg/mL in TFE after adding (a) 15 $\mu\text{L}$ , (b) 30 $\mu\text{L}$ , and (c) 60 $\mu\text{L}$ of IPA. (d) The corresponding AFM image of (c). Scale bars 500 nm.....	71
4.5	Preparation of ZIPA-SB nanofibers and representative TEM images of ZIPA-SB nanostructures at fixed final ZIPA-SB concentration (a' and a'' at 0.15 mg/mL and b series at 0.35 mg/mL) with different vol % of IPA as indicated on the images.....	71
4.6	Adding IPA to ZIPA-PC solution in TFE (1 mg/mL) led to change in solution color, but no distinct features were observed by TEM from drop-casted solution samples. Scale bar 500 nm.....	72
4.7	UV/Vis absorption spectra of (a) ZIPA-SB and ZIPA-PC in TFE, methanol and water. (b) The evolution of UV/Vis/IR absorption upon doping ZIPA-PC in TFE solution with TFA. ....	73
4.8	(a) UV/Vis absorption spectra of ZIPA-SB and ZIPA-PC thin films, where the tangential lines suggest identical bandgap $\sim 1.8$ eV. Representative UPS spectra showing (b) the $E_{\text{Sec}}$ onset, and (c) HOMO energy level of ZIPA-SB and ZIPA-PC.....	74
4.9	(a) The mono-substituted phenyl poly(1,6-heptadiyne) (P-PA). (b) UV/Vis spectra of P-PA ( <i>red</i> ) in comparison to ZIPAs ( <i>black</i> and <i>grey</i> ). (c) UPS spectra showing the $E_{\text{Sec}}$ of Ag ( <i>blue</i> ), P-PA/Ag ( <i>red</i> ), and ZIPA/Ag ( <i>grey</i> and <i>black</i> ).....	76

4.10	The NEXAFS spectra of (a) ZIPA-SB and (b) ZIPA-PC film (~ 5 nm) on Ag. ....	77
4.11	AFM height images of active layer (a) before and (a') after EGME washing. (b) and (c) show the surface of ZIPA-PC and ZIPA-SB coated on active layer, respectively. (b') and (c') are ZIPA-PC and ZIPA-SB coated on EGME washed active layer, respectively.....	79
4.12	(a) The solar cell configuration, and the chemical structure of PTB7-Th (donor) and PC <sub>71</sub> BM (acceptor) (b) The device performances (averaged over 6 devices) with and without ZIPA interlayers.....	80
4.13	The representative IV curves of PSCs with varied ZIPA-PC thickness at the active layer-Ag cathode interface. The optimal thickness at ~ 5 nm gave ZIPA-PC modified solar cells an average performance of 9.2 %. ....	81
6.1	The metal vessel used in preparing the PCDTBT nanofibers .....	87
A. 1	The graph showing the decrease in solar cell performance upon successive measurements. PATSBs were used as cathode modifiers. It was found that increasing the azulene density improves interlayer uniformity as well as device stability.....	92
A. 2	Chemical structures and TEM images of (a) sulfobetaine functionalized gold nanoparticles (SB Au-NPs), and (b) phosphorylcholine functionalized gold nanoparticles (PC Au-NPs).....	92
A. 3	(a) UPS spectra of Ag ( <i>black</i> ) and SB Au-NP/Ag ( <i>red</i> ) substrate. A 0.4 eV WF reduction of Ag was observed. (b) TEM image revealing non-uniform coverage of SB Au-NPs on active layer.....	93
A. 4	(a) Device configuration and chemical structures of PTB7-Th (donor) and PC <sub>71</sub> BM (acceptor). (b) Summary of solar cell performances.....	93
A. 5	TEM images showing the dispersion of PC Au-NPs in corresponding polymer matrixes.....	94
A. 6	Performance of solar cells employing hybrid interlayers: PC Au-NPs with PS-P4VP block copolymers and P4VP. ....	94



## LIST OF SCHEMES

Scheme	Page
2.1 Synthesis route to PCDTBT using Suzuki coupling. <sup>18</sup> .....	29
2.2 Preparation of PCDTBT nanofibers. ....	30
2.3 Proposed mechanism of PCDTBT nanofiber formation.....	36
2.4 PCDTBT derivatives: PCD <sup>6</sup> TBT ( <i>left</i> ) and PCD <sup>8,12</sup> TBT ( <i>right</i> ) .....	39

## CHAPTER 1

### CONJUGATED POLYMERS AND POLYMER-BASED SOLAR CELLS (PSCS)

#### 1.1 Current Progress on Polymer-Based Solar Cells (PSCs)

Developing renewable energy sources to alleviate the dependence on fossil fuels is critical for building a sustainable future. Towards such a goal, solar energy has been explored as an alternative energy source due to its abundance and minimum environmental impact. In the 2000 World Energy Assessment by the United Nations Development Program, the annual potential of solar energy was estimated as 1,500-49,000 exajoules (EJ), at least 3 times more than the total world energy consumption of  $\sim 560$  EJ in 2012.<sup>1</sup> Early attempts to commercialize solar energy date back to 1915, where solar radiation was used to power steam engines for irrigation. This concept has since evolved into modern concentrated solar power systems, where concentrated sunlight heats a working fluid to generate electricity.

A more direct method to convert sunlight into electricity is found in photovoltaic devices (PVs), also known as solar cells, via the photoelectric effect. This phenomenon was discovered by Edmond Becquerel in 1839,<sup>2</sup> and the first solid state PV was prepared by Charles Fritts from a bilayer of selenium and gold in 1883.<sup>3</sup> The power conversion efficiency (PCE, the ratio between the output and the input of energy) of such cells was approximately 1%. Today, the solar panels commonly seen on rooftops consist of crystalline silicon, which were developed by Gerald Pearson, Calvin Fuller and Daryl Chapin in 1954 at Bell labs.<sup>4</sup> Those early cells cost 286 USD/watt, and provided PCE values between 4.5-6.0 %.<sup>5</sup> Further, due

to the oil-gas crisis, man-made climate change and strong government support in searching for alternative energy resources, PVs have gained research momentum and experienced exponential growth, both in performance and market share, in the last two decades. PVs are anticipated to become the mainstream electricity source by 2050.<sup>6</sup>

Today, silicon-based PVs have PCE values of 15–25 %.<sup>7,8</sup> In contrast, polymer-based solar cells (PSCs) lag behind, with single digit PCEs when fabricated on a lab scale. Nevertheless, scientists and engineers have continuously developed novel materials and new fabrication methods for PSCs. Their potential as low-cost, lightweight, and flexible PV modules presents new application possibilities that are not given by the rigid inorganic solar cells. Further, PSCs can be fabricated by high throughput manufacturing processes, such as ink-jet printing and roll-to-roll processing,<sup>9</sup> significantly reducing the production cost and energy consumption. These devices are typically thin and flexible, and therefore can be integrated into appliances and building materials with better performance under interior lightings (low light levels) in comparison to inorganic counterparts.<sup>10</sup> Moreover, PSCs benefit from a myriad of available materials that the molecular structure and bandgap can be tailored through synthesis.

Building efficient PSCs relies on multidisciplinary efforts to understand the energy conversion mechanism, to synthesize new materials and, to engineer morphology and interfaces. This introduction chapter describes the basic principles of PSCs, morphology-performance relationships, and electrode interface designs to enable efficient charge extraction.

## 1.2 PSC Operation Mechanism and Material Designs

The first PSCs were prepared in an electron donor-acceptor bilayer configuration by Sariciftci in 1993. It consisted of successive layers of poly[2-methoxy,5-(2'-ethyl-hexyloxy)-1,4-phenylene-vinylene] (MEH-PPV) and buckminsterfullerene ( $C_{60}$ ), and afforded  $\sim 0.04\%$  efficiency.<sup>11</sup> Similar to a typical diode, PV operates as a p-n junction where charge diffusion formed a depletion zone, generating an internal electric field (from electron rich (n-type) to hole rich (p-type) region). Applying a forward bias (connecting the positive terminal to the p-type side and the negative terminal to the n-type side) to the cell reduces the built-in electric field, establishes a new charge distribution, and results in a current ('dark current') flowing through the device. This response can be recorded by measuring the output current against the applied external voltage, giving a current-to-voltage (IV) curve. Unlike a typical diode, when under illumination, free carriers are generated and transported to the corresponding electrodes, creating a vertical translation in the IV curve as shown in Figure 1.1. To simulate device operation under sunlight, the illumination source is calibrated to match the solar irradiance at air mass (AM) 1.5, a standard set to correspond to the solar spectrum in North America and Europe at  $45^\circ$  above the horizon. The IV curve recorded under such conditions is subsequently used to calculate the PCE from Equation 1.1. Specifically, the short circuit current ( $J_{sc}$ ) refers to the current collected at the electrodes with no applied voltage, the open circuit voltage ( $V_{oc}$ ) gives the maximum potential generated from the cell, and the fill factor (FF) is the ratio of maximum device power ( $J_m \times V_m$ ) to the product of  $J_{sc}$  and  $V_{oc}$  (Equation 1.2).

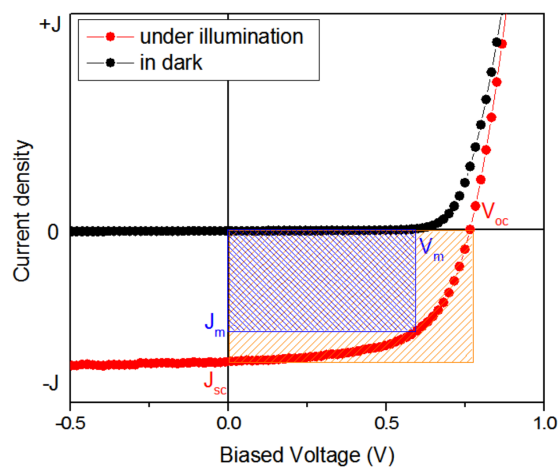


Figure 1.1 The dark current (*black*) and the IV response of PSCs under light (*red*).  $J_{sc}$  is the current measured at no external bias,  $V_{oc}$  is the maximum potential generated by the cell, and the ratio of maximum device power ( $J_m \times V_m$ ) to the product of  $J_{sc}$  and  $V_{oc}$  (the ratio of blue to orange area) gives the fill factor (FF).

$$PCE = \frac{P_{out}}{P_{in}} = FF \times \frac{J_{sc} \times V_{oc}}{P_{in}} \quad (\text{Equation 1.1})$$

$$FF = \frac{J_m \times V_m}{J_{sc} \times V_{oc}} \quad (\text{Equation 1.2})$$

To date, the most successful PSCs utilize fullerene derivatives as the electron acceptor and conjugated polymers as the electron donor in the photoactive layer.<sup>12</sup> In contrast to conventional polymers, conjugated polymers contain alternating single and double carbon bonds in the backbone, resulting in delocalized electrons with a specific energy bandgap ( $E_g$ ).  $E_g$  is defined by the difference between the highest occupied molecular orbital (HOMO) and the lowest unoccupied molecular orbital (LUMO), analogous to the valence band maximum and conduction band minimum in inorganic semiconductors. In contrast to their inorganic counterparts, polymer semiconductors have relatively low dielectric constants ( $\epsilon_r \sim 2-4$ ) such that

light excitation generates bonded electron-hole pairs (Frenkel excitons) instead of free charge carriers. An offset in the HOMO of polymer donors and the LUMO of fullerene acceptors (0.3-1 eV) is required to dissociate excitons into holes and electrons, and another offset ( $> 0.3$  eV) between the LUMOs of the donor and acceptor components is needed to transfer the electrons to the acceptor phase. The charge separated electrons and holes subsequently travel via the acceptor and donor network, respectively, to the corresponding electrodes. The charge collection efficiency at the electrodes depends on both the charge transport and extraction processes, which are affected by factors such as the ordering of the donor/acceptor domains and the strength of the built-in potential bias given by the energy level difference between the electrodes (Figure 1.2).

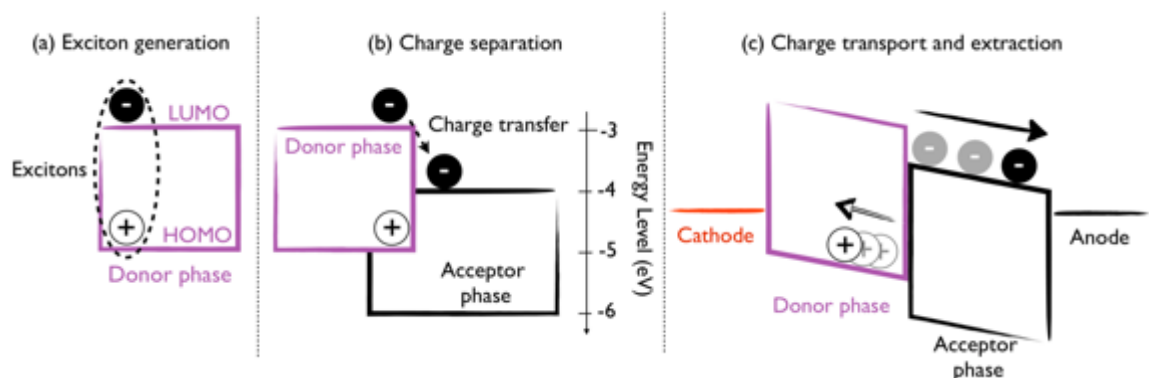


Figure 1.2 A typical photovoltaic process in PSCs starts with (a) light generating an exciton, which diffuses to the donor-acceptor interface where (b) charge separates into electrons and holes. These free charge carriers are then (c) driven by the built-in potential to travel to the corresponding electrodes.

The open circuit voltage ( $V_{oc}$ ) and the short circuit current ( $J_{sc}$ ) of PSCs provide insight into the inner workings of the PV cells. The value of the  $V_{oc}$  in PSCs is proportional to the difference between the HOMO and LUMO of the donor and

acceptor and is estimated using Equation 1.3. The value of  $J_{sc}$  is the integral of the photon flux ( $\phi$ ) and device external quantum efficiency (EQE), which is the ratio of carriers collected by the solar cell to the number of photons at a given incident energy (Equation 1.4). As the wavelength of the solar spectrum at AM 1.5 spans from 100 nm to  $\sim 1$  mm, with most photons populating the low energy (long wavelength) end, lowering the bandgap of the donor polymer leads to increased  $J_{sc}$  (Figure 1.3). Thus, an ideal donor conjugated polymer should have a low HOMO to obtain high  $V_{oc}$ , and a narrow band gap ( $< 2$  eV) to increase light absorption.

Following this rationale, many high-performance donor materials have been developed in the last decade. A common strategy to achieve low band gap donor polymers involves coupling an electron rich and an electron deficient moiety.<sup>13</sup> Some examples of these conjugated polymers include poly[2,6-(4,4-bis-(2-ethylhexyl)-4H-cyclopenta[2,1-*b*;3,4-*b'*]dithiophene)-alt-4,7-(2,1,3-benzothiadiazole)] (PCPDTBT), which absorbs light up to 900 nm, and poly[*N*-9''-heptadecanyl-2,7-carbazole-alt-5,5-(4',7'-di-2-thienyl-2',1',3'-benzothiadiazole)] (PCDTBT)-based PSCs, which provided 100 % quantum efficiency (after removing optical loss from device reflection and transmission), and thieno[3,4-*b*]-thiophene and benzodithiophene alternating copolymers (*i.e.*, poly[[4,8-bis[(2-ethylhexyl)oxy]benzo[1,2-*b*:4,5-*b'*]dithiophene-2,6-diyl][3-fluoro-2-[(2-ethylhexyl) carbonyl]thieno[3,4-*b*]thiophenediyl]] (PTB7)<sup>14</sup> and poly[[2,6'-4,8-di(5-ethylhexylthienyl)benzo[1,2-*b*:3,3-*b*]dithiophene] [3-fluoro-2-[(2-ethylhexyl)carbonyl]thieno[3,4-*b*]thiophenediyl]] (PTB7-Th)),<sup>12</sup> which gave devices with PCEs reaching 10 %.

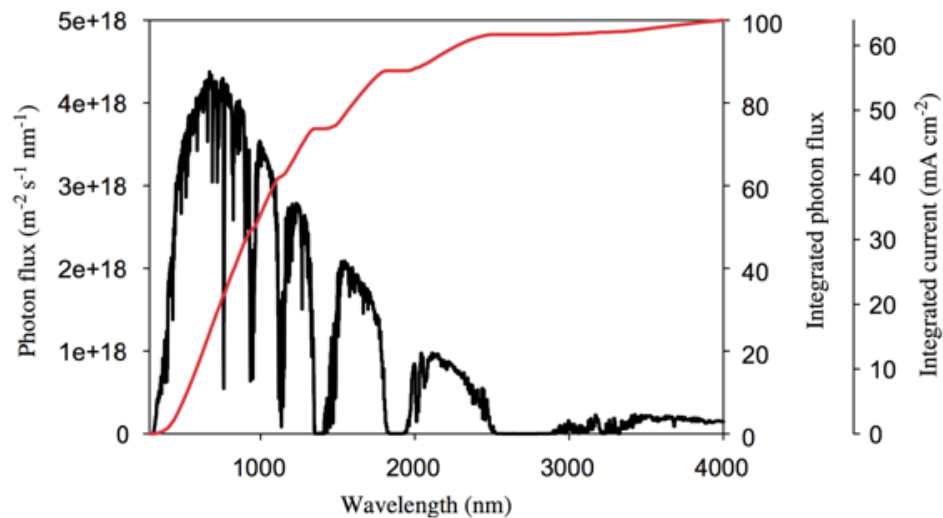


Figure 1.3 Photon flux at AM1.5 as a function of wavelength (*black line*). The integrated number of photons and the corresponding obtainable current density is shown in red.<sup>13</sup>

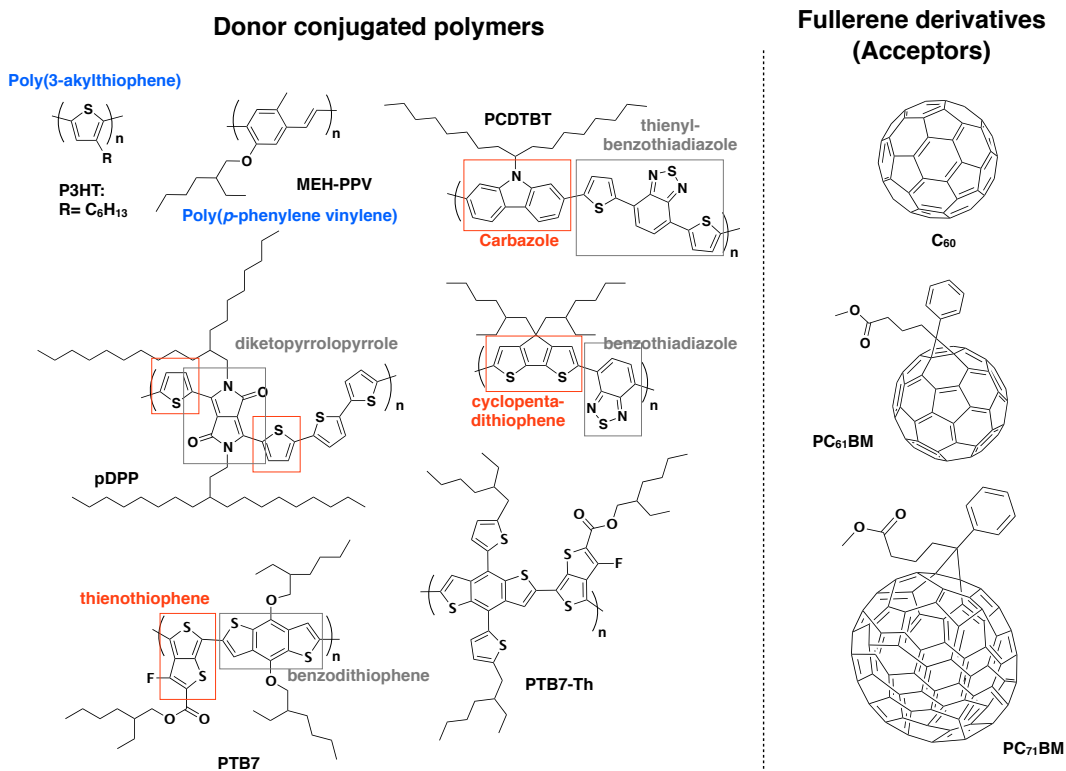


Figure 1.4 Chemical structures of common donor polymers and fullerene acceptors used in PSCs.



$$V_{oc} = \frac{(|E_{HOMO}^{donor}| - |E_{LUMO}^{acceptor}| - 0.3 \text{ eV})}{e} \quad (\text{Equation 1.3})$$

$$J_{sc} \sim \int \phi(\lambda) \cdot EQE(\lambda) d\lambda \quad (\text{Equation 1.4})$$

### 1.3 Conjugated Polymers in Solution, and as Thin Films: Impact on Device Performance

Tailoring the morphology of conjugated polymers, in solution as well as in thin films, is critical for advancing the fundamental science and technology of these materials.<sup>15</sup> In addition to the intrinsic optoelectronic properties of organic materials, an efficient photoactive layer requires the electron donor and acceptor components to form continuous domains at the length scale of exciton diffusion lifetime (~10 nm) over large areas. Such domains facilitate charge separation and transport while suppressing charge recombination. The low efficiency observed in the first solution processed PSC was partially due to the bilayer device geometry, in which the donor and acceptor formed an interface with limited area and a long carrier lifetime was required for charge collection.<sup>16</sup> To increase the surface area of the donor-acceptor interface, Hiramoto co-evaporated donor and acceptor molecules and prepared the first so-called bulk heterojunction (BHJ) devices (Figure 1.5).<sup>17</sup> Such approach was later transferred to all-solution processed PSCs,<sup>18,19</sup> where the active layer was prepared from co-dissolved donor and acceptors, providing the foundation for subsequent PSC development.

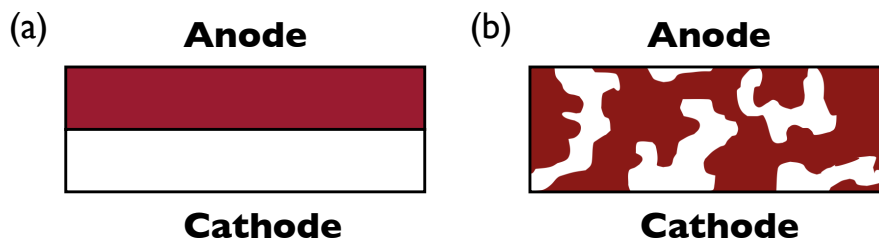


Figure 1.5 (a) Bilayer and (b) bulk heterojunction (BHJ) device configurations. The white and maroon domains represent the donor and the acceptor components, respectively.

The performance of BHJ devices depends heavily on the device fabrication conditions. The selection of solvents,<sup>20</sup> additives,<sup>21-23</sup> and annealing temperatures<sup>24,25</sup> was found to influence crystallinity and phase separation of organic and polymer components of thin films, which impacted the final device efficiency. These factors gained appreciable attention in the morphological investigation of poly(1,4-phenylene vinylene) (PPV)-based PSCs, one of the early promising PSC systems affording PCE values of 3 %. Examining the morphology of PPV/phenyl-C<sub>61</sub>-butyric acid methyl ester (PC<sub>61</sub>BM) films, and its influence on device performance as a function of processing conditions led to the conclusion that the presence of PC<sub>61</sub>BM aggregates in the active layer diminishes device efficiency. Such features could be avoided either by increasing the concentration of PC<sub>61</sub>BM in the thin films, or by using chlorobenzene instead of toluene as the casting solvent.<sup>26,27</sup> Moreover, the formation of fibrillar PPV networks was found to enhance device efficiency (Figure 1.6).<sup>28</sup> These pioneering studies reached many important conclusions that proved influential for the design and fabrication of organic/polymer solar cells by numerous researchers over the ensuing years.

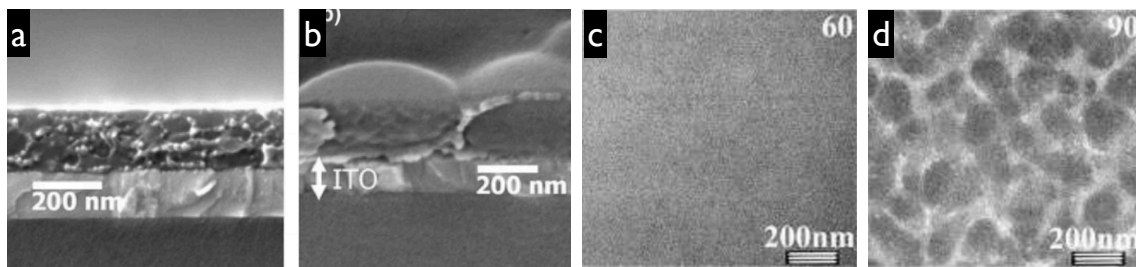


Figure 1.6 SEM images showing the cross-section of PPV/PC<sub>61</sub>BM films processed from (a) chlorobenzene, and (b) toluene.<sup>22</sup> TEM images of PPV/PC<sub>61</sub>BM films with (c) 60 wt % and (d) 90 wt % of PC<sub>61</sub>BM.<sup>28</sup>

Low band gap polymers, similar to PPV derivatives, often bear long substituted alkyl side chains to improve the solubility of the rigid backbones. Such molecular architectures, however, render the polymers less crystalline, forming either intimately mixed domains or large phase-separated structures with PCBM, unfavorable for charge extraction, separation and transport.<sup>15</sup> To achieve the desired morphology with percolated nanonetworks to maximize electronic performance, active layers are cast from co-solvents solutions, where one solvent is a good solvent (host) for both the donor polymer and PCBM, while the other is a PCBM-selective solvent. Typically, the host solvent induces crystallization of the donor polymer as it evaporates, and the selective solvent prevents the formation of PCBM aggregates. The first example of using solvent additives was in cyclopentadithiophene-based polymer PSCs (*i.e.*, PCPDTBT), where 1,8-octanedithiol was added to sequester phenyl-C<sub>71</sub>-butyric acid methyl ester (PC<sub>71</sub>BM) and induce crystallization of the polymer, improving the performance from 3 to 5%.<sup>21,23</sup> For materials with stronger ordering capability, such as copolymers of diketopyrrolopyrrole (DPP)-quarterthiophene (*i.e.*, pDPP)<sup>29</sup> and thienothiophene-benzodithiophene (*i.e.*, PTB7

and PTB7-Th),<sup>30,31</sup> additives decrease the domain sizes and afford hierarchical morphology with the formation of a fibrillar donor network (Figure 1.7).

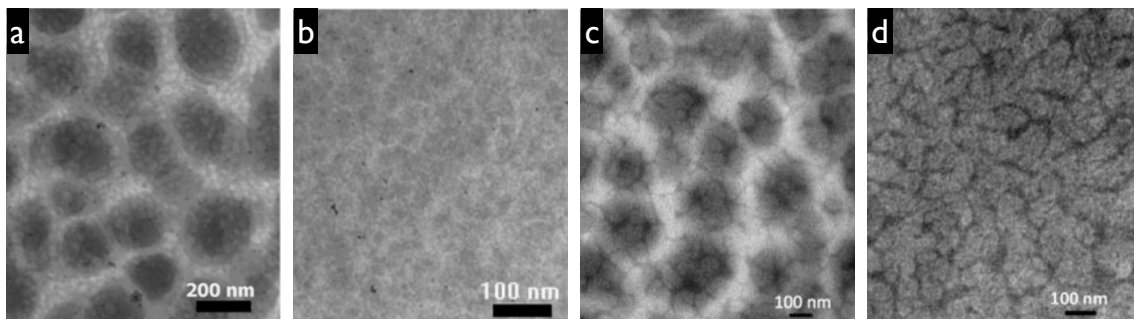


Figure 1.7 TEM images of pDPP/PC<sub>71</sub>BM based active layer prepared from (a) chloroform (host solvent), and (b) a co-solvent of chloroform:chlorobenzene at 4:1 volume ratio.<sup>29</sup> Similar trends were observed in PTB7/PC<sub>71</sub>BM — (c) prepared from chlorobenzene (CB) (host) and (d) a co-solvent of CB and 1,8-diiodooctane at 3 vol % as the additive.<sup>30,31</sup>

The most extensive morphological research was performed on poly(3-alkylthiophene)s, especially on the benchmark system, poly(3-hexylthiophene) (P3HT) in conjunction with PC<sub>61</sub>BM. While the optoelectronic properties of P3ATs are determined by the thiophene backbone, its solid-state packing is governed by the interplay between the alkyl-substituents and the conjugated backbone. Competition between alkyl-alkyl side-chain interactions and  $\pi$ - $\pi$  backbone stacking affords P3AT nanowires and nanosheets in poor solvents,<sup>32</sup> with corresponding lattice spacings of  $\sim 16$  Å (100) and 3.8 Å (010), respectively.<sup>33</sup> Such ordered structures reduce the electron-hopping barrier, and dramatically improve the hole mobility by two orders of magnitude (Figure 1.8).<sup>32,34-38</sup> The propensity for P3HT to crystallize while being miscible with PC<sub>61</sub>BM made it a unique system in contrast to other PSCs. A brief thermal or solvent annealing was found to form an interconnected fibrillar P3HT nanonetwork in the blended P3HT/PC<sub>61</sub>BM film<sup>39</sup>— a

morphology that is challenging to obtain in low-band-gap PSCs without employing additives. However, prolonged thermal annealing leads to domain coarsening and decreases device efficiency. Alternative methods that avoid post-annealing of devices while reach comparable morphology and device performance include blending PC<sub>61</sub>BM with preformed P3AT semicrystalline fibers prepared from solution,<sup>40-43</sup> adding high boiling solvents as additives to induce crystallization,<sup>44,45</sup> or diffusing PC<sub>61</sub>BM into crystallized P3HT in a bilayer configuration.<sup>39</sup>

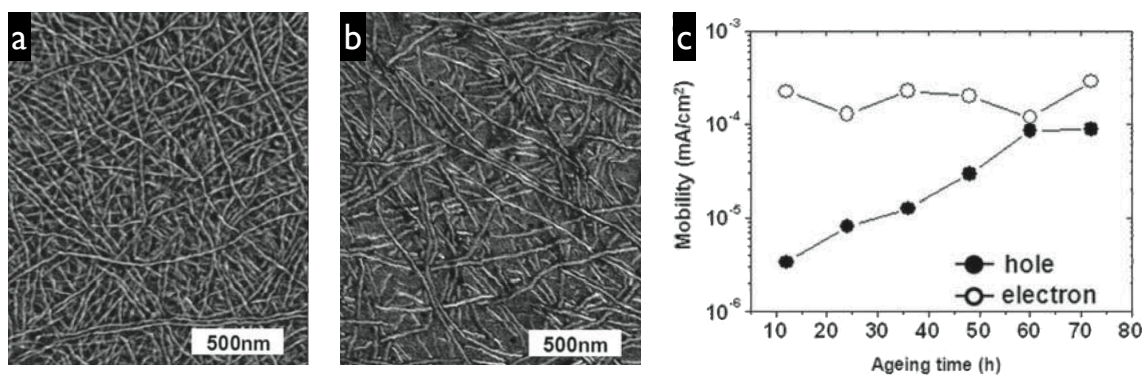


Figure 1.8 TEM images of (a) P3HT nanowires prepared from dichloromethane, (b) P3HT nanowires blended with PC<sub>61</sub>BM. (c) Hole-electron mobility of solar cells composed of PC<sub>61</sub>BM/P3HT nanowires, prepared from various aging time in dichloromethane.<sup>43</sup>

#### 1.4 Electrode Interfaces Engineering

Tailoring active layer-electrode interfaces affords better charge collection, maximizes the active layer performance, and increases device stability and lifetime.<sup>46</sup> An ideal interface aligns the energy levels between the organic active layer and the inorganic electrode (forming an Ohmic contact), and ensures a strong built-in potential across the device to drive charge transport and suppress charge recombination. In the early development of PSCs, air-sensitive metals with low work functions were used as cathodes (*i.e.*, Ca, Ba, and Al) to generate high potential bias.

However, these cathodes are prone to oxidation and led to short device lifetime. To overcome this, new materials and fabrication methods are required to allow the use of inert metal as cathodes, while maintaining substantial potential bias across the device for efficient charge collection.

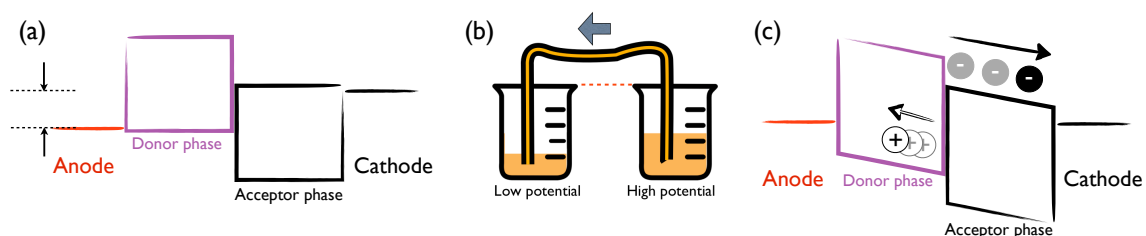


Figure 1.9 (a) The WF difference between anode and cathode establishes a potential bias across the cell. This is analogous to (b) potential difference between the beakers causing water flowing through the connection. (c) The energy diagram upon reaching equilibrium.

The potential bias in the device is generated by the difference in the energy levels of the cathode and the anode. This energy level is also known as the work function (WF) of the metal, which is defined as the energy to move an electron from the metal surface to infinity (vacuum level). The metal work function depends on the bulk chemical potential and electrostatic potential across the metal surface.<sup>47</sup> When a PSC is connected to an external circuit, the electrons in the anode and cathode are redistributed to reach equilibrium, creating a built-in potential difference across the device. (Figure 1.9) This is analogous to connecting two water buckets with a straw, where the water flows from the bucket with higher potential energy to the other (Figure 1.9 (b)). Since a high built-in potential across the device is desirable for efficient charge collection, reducing the WF of inert metals is expected to render

inert metals as promising cathodes, reaching device performance equal to those using air-sensitive low WF metals.

Attempts to tune metal WF involve coating a thin layer of polar organic materials on metals, known as an interlayer. In addition to a small WF reduction, arising from the push-back effect,<sup>47</sup> the mechanism for WF modification at metal-organic interfaces has been attributed to doping, charge-transfer, and dipole formation.<sup>47-51</sup> LiF was one of the early materials used to modify electrodes to improve the efficiency of organic electronics.<sup>52</sup> However, LiF and many other small molecule-based electrode modifiers require costly vacuum deposition procedures, and their moisture sensitivity leads to short device lifetime. Recent advances describe the success in overcoming these disadvantages by applying a thin layer of polar polymer on air-stable metal electrodes to reduce their work functions to that of air-sensitive metals.

Dipole alignment of polar polymers at the organic-metal interface is the most accepted model to explain the abrupt and rigid change in metal WF.<sup>53,54</sup> This has been proposed because the change of WF is independent of polymer film thickness,<sup>50</sup> type of metal substrates,<sup>46,50,55</sup> and energy alignment between the organic-metal is not required.<sup>50,54,56,57</sup> This allows scientists to explore many classes of polymers, ranging from insulators to conductors, as electrode modifiers. The influence of dipole alignment on the metal WF was first studied in chemisorbed self-assembled monolayers (SAMs) of small molecules on metal substrates. It was found that a net dipole moment oriented away from the metal surface decreases the WF,

and vice versa (Figure 1.10).<sup>58</sup> In addition, the change in work function ( $\Delta\phi$ ) can be estimated by the Helmholtz equation as follows:<sup>59</sup>

$$\Delta\phi = \frac{N \times \mu_{mol}}{\epsilon_r \times \epsilon_0} \quad \text{(Equation 1.5)}$$

where  $N$  is the areal density of absorbed molecules,  $\mu_{mol}$  is the net vertical component of the interfacial dipole moment of an individual molecule,  $\epsilon_r$  is the relative dielectric constant of the molecules, and  $\epsilon_0$  is the permittivity of vacuum.<sup>58,59</sup>

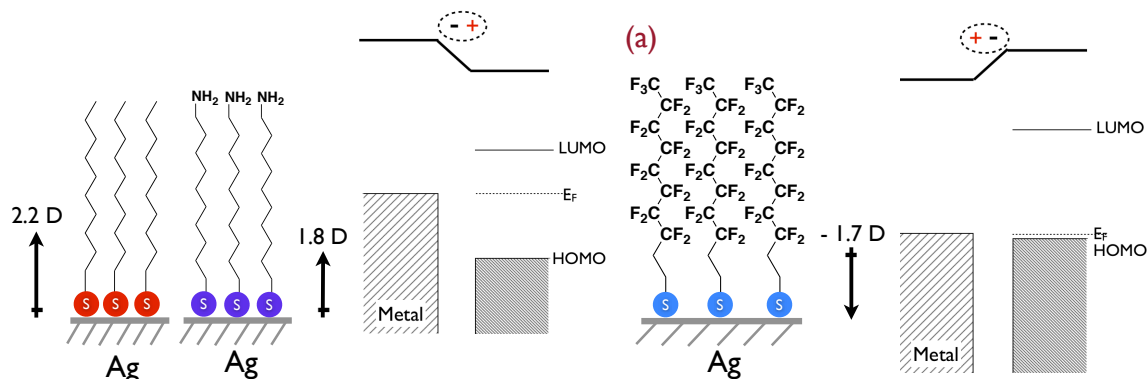


Figure 1.10 The effect of dipole orientation on work function of Ag with corresponding energy diagrams. (a) Dipoles pointing away and (b) toward Ag.<sup>58</sup>

One of the most widely reported polymeric cathode modifiers consists of a fluorene backbone with pendent polar substituents. Initially developed by Bazan for organic light emitting diodes (OLED), this class of polymers was later utilized by Cao as cathode modifiers in PSCs. Within this class of polyfluorenes, poly [(9,9-bis(3'-(*N,N*-dimethylamino) propyl)-2,7-fluorene)-*alt*-2,7-(9,9-dioctylfluorene)] (PFN) emerged as a promising cathode modifier.<sup>60-62</sup> A significant increase in PCE (from 4.0 % to 6.0 %), was observed for devices containing PFN between the metal electrode



and the active layer (poly[(4,5-ethylene-2,7-carbazole)-5,8-bis(2'-thienyl)-2,3-bis(4-octyloxyphenyl) quinoxaline] (PECz-DTQx) and PC<sub>71</sub>BM).<sup>63</sup> Even higher PCEs of 6.8 and 8.4 % were achieved upon inserting PFN in PCDTBT/PC<sub>71</sub>BM-based PSCs and PTB7/PC<sub>71</sub>BM-based PSCs, respectively.<sup>64</sup> Scanning Kelvin probe microscopy (SKPM) revealed PFN-covered PCDTBT/PC<sub>71</sub>BM to be +300 mV higher in surface potential than the unmodified active layer.<sup>60</sup> This suggests the presence of an interfacial dipole moment where the positive end points to the electrode (Figure 1.11). Such dipole orientation afforded a built-in electric field of  $\sim 6 \times 10^5$  Vcm<sup>-1</sup> across the cell, approximately an order higher than devices without the PFN interlayer. Interestingly, although charge selectivity has been suggested to be crucial for modifying electrodes, both n-type and p-type polymers were found to be effective cathode modifiers.<sup>65</sup> For example, Duan *et al.* compared zwitterionic conjugated polymers with electron-rich backbones (poly[(9,9-bis((N-(4-sulfonate-1-butyl)-N,N-dimethylammonium)propyl)-2,7-fluorene)-alt-(N-phenyl-4,40-diphenylamine)] (PFNSO-TPA), poly[(9,9-bis((N-(4-sulfonate-1-butyl)-N,N-dimethylammonium)propyl)-2,7-fluorene)-alt-2,7-(9,9-dioctylfluorene)] (PFNSO)) and, electron-deficient backbones (poly[(9,9-bis((N-(4-sulfonate-1-butyl)-N,N-dimethylammonium)propyl)-2,7-fluorene)-alt-4,7-(2,1,3-benzothiadiazole)] (PFNSO-BT)), and found all these polymeric zwitterions gave satisfactory device performance.<sup>66</sup> This is possibly due to the typical thickness of these modifiers is  $\sim 5$  nm that electrons can still inject efficiently into the metal cathode through tunneling or thermionic injection, as observed in insulating polymer electrode modifiers.<sup>54</sup>

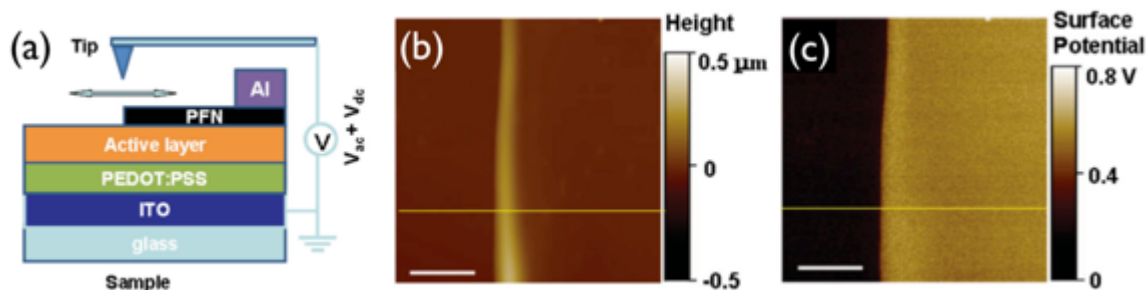


Figure 1.11(a) Experimental setup to measure surface potential. (b) The topology and (c) the surface potential of the active layer without (*left*) and with PFN (*right*) measured by scanning Kelvin probe microscopy.

Although  $\Delta\phi$  is independent of the modifier thickness, the performance of solar cells is strongly influenced by the thickness variation in the electrode modifiers.<sup>54,67,68</sup> Increasing the thickness by a few nm from the optimal thickness ( $\sim$  5-8 nm) led to an S-shaped IV curve, indicating increased charge accumulation and recombination at the active layer-electrode interface. Decreasing the modifier thickness from the optimal value gave insufficient built-in potential with smaller  $V_{oc}$ ,  $J_{sc}$ , and FF.<sup>67</sup> Such thickness-performance dependence is more pronounced in materials with lower charge mobility, such as in insulating<sup>54</sup> and p-type polymers.<sup>67,68</sup> Fortunately, several reports show that increasing the mobility of the cathode modifier leads to higher tolerance for thickness variation, giving robust performance.<sup>46,69,70</sup>

Surprisingly, the performance of electrode modifiers showed a stronger dependence on the active layer than on the metal cathode. The same interlayer/electrode pair, which is expected to have the same WF, impacts PSCs containing various active layers in different ways. For example, PFN/Al increased the efficiency of PCDTBT/PCBM by  $\sim$ 68 %, yet no improvement was seen when it was

used as cathode in P3HT/PCBM or MEH-PPV/PCBM-based devices.<sup>71</sup> In a typical device fabrication, the modifiers are spin-coated on the active layer before cathode evaporation, therefore, a uniform and complete coverage of the interlayer on the top of the active layer is important. Indeed, the coating quality of the cathode modifier depends on the surface energy of the active layer. As the surface energy of P3HT/PCBM and MEH-PPV/PCBM are lower than other low-band-gap polymer/PCBM blended films, obtaining pinhole free interlayers in the P3HT or MEH-PPV system is challenging. To overcome the film instability, Chang *et al.* used an anionic surfactant, sodium dodecylbenzenesulfonate (SDS), as the counter ion of poly[3-(6-trimethylammoniumhexyl)thiophene] (PTMAHT) to form an electrostatically stable complex, which doubled the PCE.<sup>72</sup> These studies suggest that in addition to molecular design, uniform coating of interlayer is also critical to obtain high performance devices.

In addition to conjugated polyelectrolytes with ammonium cations, polymers with primary, secondary and tertiary amines, such as PFN,<sup>64</sup> polyethyleneimine (PEI)<sup>54</sup> and polyallylamine (PAA)<sup>73</sup> have been used to modify cathodes. Kang *et al.* suggested that the origin of WF reduction by these materials is the dipole formation between the positively charged amines (protonated amines) and the negatively charged electrode surfaces.<sup>73</sup> Other commonly reported functional groups include phosphonates<sup>74,75</sup> and ethers, such as in polyethylene oxide (PEO) and poly[(9,9-bis((6'-(N,N,N-trimethylammonium)hexyl)-2,7-fluorene)-alt-(9,9-bis(2-(2-(2-methoxyethoxy)ethoxy)ethyl)-9-fluorene))] dibromide (WPF-6-oxy-F).<sup>76</sup> Some examples of cathode modifiers are shown in Figure 1.12.

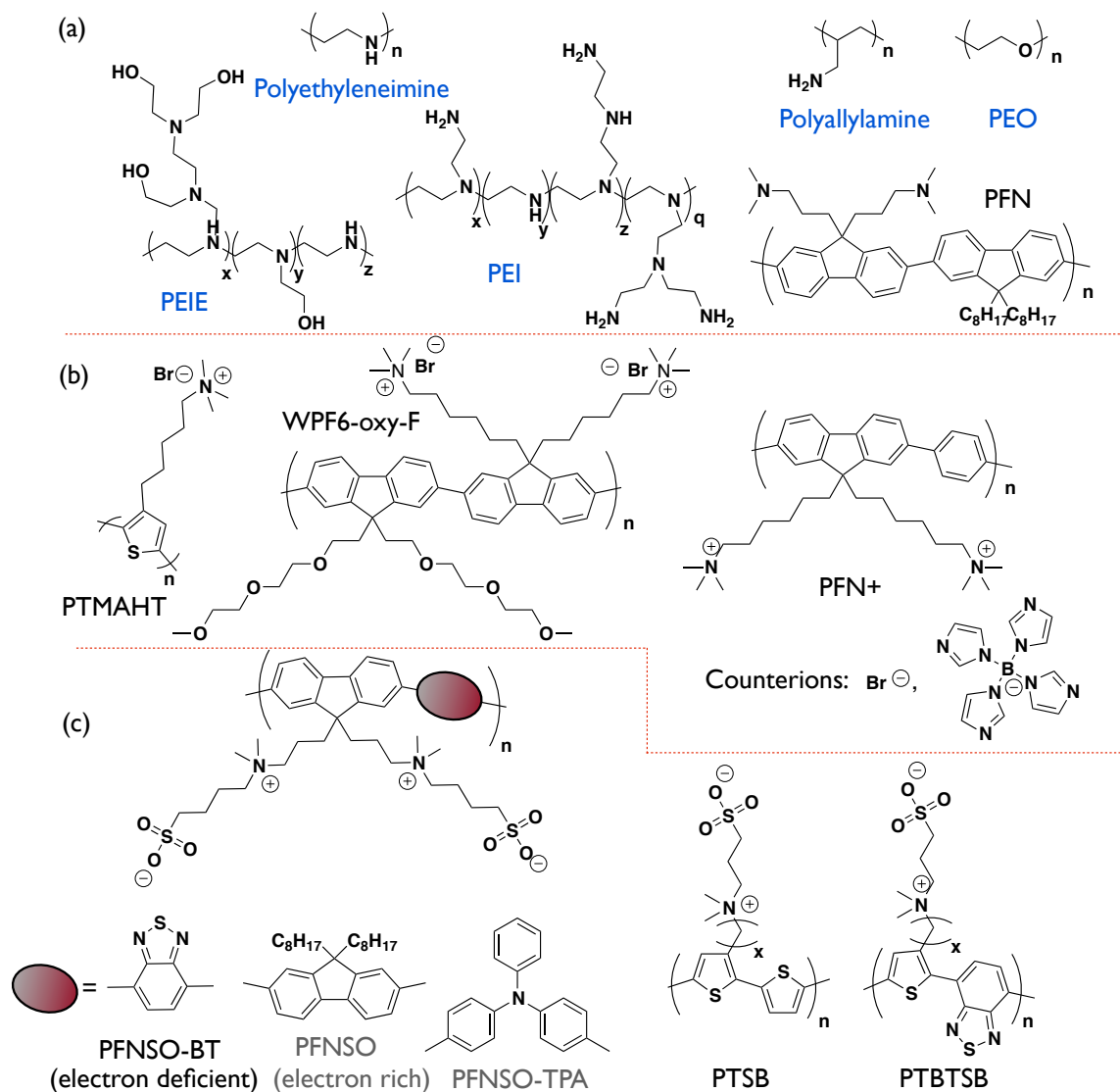


Figure 1.12 Examples of polymeric electrode modifiers with (a) amines and ethers functionalities, (b) conjugated polyelectrolytes, and (c) conjugated polyzwitterions.

## 1.5 Thesis Outline

Prior studies of the morphology of electronically active polymers in solution, in thin films and at interfaces have contributed to the remarkable advances in PSCs. Exercising control over polymer nanostructure and crystallization enabled efficient device fabrication, eliminating the need for post-treatment of conventional P3HT/PC<sub>61</sub>BM devices. Inserting amphiphilic polymers between the electrode and

active layer improves charge collection, and consequently enhances device performance. My thesis work investigates the crystallization of conjugated polymers in solution, and examines the properties of novel polymer zwitterions at the electrode/active layer interface.

**Chapter 2** describes the solvent-induced crystallization of a low band gap polymer, PCDTBT. A metal vessel was used to heat PCDTBT in dichloromethane, ultimately affording semi-crystalline PCDTBT nanofibers in solution. These structures were characterized by grazing-incident wide angle X-ray scattering (GI-WAXS), atomic force microscopy (AFM) and transmission electron microscopy (TEM). **Chapter 3** highlights novel azulene-containing zwitterionic sulfobetaine methacrylate copolymers as cathode modifiers to achieve high performance solar cells, where the wettability of the copolymers on the active layer was found critical for enhancing device efficiency. **Chapter 4** describes zwitterionic polyacetylenes (ZIPAs), in which phosphorylcholine groups were observed to be effective for modifying the PSC cathode. Lastly, **Chapter 5** presents a summary and brief perspective for interlayer materials in enhancing solar cell stability and lifetime to realize commercialization in the near future. Opportunities for using zwitterion-functionalized gold nanoparticles as electrode modifiers are also discussed with preliminary results presented in the appendix.

## 1.6 References

1. Energy and the challenge of sustainability <http://www.undp.org/content/dam/aplaws/publication/en/publications/environment-energy/www-ee-library/sustainable-energy/world-energy-assessment-energy-and-the-challenge-of-sustainability/World%20Energy%20Assessment-2000.pdf>.

2. Becquerel, A. E. *Annalen der Physick und Chemie* **1841**, *54*, 35–42.
3. Fritts, C. E. *American Journal of Science* **1883**, *s3-26*, 465–472.
4. Chapin, D. M.; Fuller, C. S.; Pearson, G. L. *J. Appl. Phys.* **1954**, *25*, 676–677.
5. Perlin, J. *From Space to Earth — The Story of Solar Electricity*; Harvard Univeristy Press, 1999.
6. Technology Roadmap: Solar Photovoltaic Energy [http://www.iea.org/publications/freepublications/publication/TechnologyRoadmapSolarPhotovoltaicEnergy\\_2014edition.pdf](http://www.iea.org/publications/freepublications/publication/TechnologyRoadmapSolarPhotovoltaicEnergy_2014edition.pdf).
7. Green, M. A.; Emery, K.; Hishikawa, Y.; Warta, W.; Dunlop, E. D. *Progress in Photovoltaics* **2015**, *23*, 1–9.
8. Saga, T. *NPG Asia Mater.* **2010**, *2*, 96–102.
9. Krebs, F. C. *Solar Energy Materials and Solar Cells* **2009**, *93*, 394–412.
10. Steim, R.; Ameri, T.; Schilinsky, P.; Waldauf, C.; Dennler, G.; Scharber, M.; Brabec, C. J. *Solar Energy Materials and Solar Cells* **2011**, *95*, 3256–3261.
11. Sariciftci, N. S.; Braun, D.; Zhang, C.; Srdanov, V. I. *Appl. Phys. Lett.* **1993**, *62*, 585.
12. He, Z.; Xiao, B.; Liu, F.; Wu, H.; Yang, Y.; Xiao, S.; Wang, C.; Russell, T. P.; Cao, Y. *Nature Photon.* **2015**, *9*, 174–179.
13. Bundgaard, E.; Krebs, F. C. *Solar Energy Materials and Solar Cells* **2007**, *91*, 954–985.
14. Liang, Y.; Xu, Z.; Xia, J.; Tsai, S.-T.; Wu, Y.; Li, G.; Ray, C.; Yu, L. *Adv. Mater.* **2010**, *22*, E135–E138.
15. Liu, F.; Gu, Y.; Jung, J. W.; Jo, W. H.; Russell, T. P. *J. Polym. Sci. B Polym. Phys.* **2012**, *50*, 1018–1044.
16. Tang, C. W. *Appl. Phys. Lett.* **1986**, *48*, 183.
17. Hiramoto, M.; Fujiwara, H.; Yokoyama, M. *J. Appl. Phys.* **1992**, *72*, 3781.
18. Halls, J. J. M.; Walsh, C. A.; Greenham, N. C.; Marseglia, E. A.; Friend, R. H.; Moratti, S. C.; Holmes, A. B. *Nature* **1995**, *376*, 498–500.
19. Yu, G.; Gao, J.; Hummelen, J. C.; Wudl, F.; Heeger, A. J. *Science* **1995**, *270*, 1789–1791.

20. Zhang, F.; Jespersen, K. G.; Björström, C.; Svensson, M.; Andersson, M. R.; Sundström, V.; Magnusson, K.; Moons, E.; Yartsev, A.; Inganäs, O. *Nature Mater.* **2007**, *6*, 497–500.
21. Peet, J.; Kim, J. Y.; Coates, N. E.; Ma, W. L.; Moses, D.; Heeger, A. J.; Bazan, G. C. *Nature Mater.* **2007**, *6*, 497–500.
22. Di Nuzzo, D.; Aguirre, A.; Shahid, M.; Gevaerts, V. S.; Meskers, S. C.; Janssen, R. A. *Adv. Mater.* **2010**, *22*, 4321–4324.
23. Gu, Y.; Wang, C.; Russell, T. P. *Adv. Energy Mater.* **2012**, *2*, 683–690.
24. Padinger, F.; Rittberger, R. S.; Sariciftci, N. S. *Adv. Funct. Mater.* **2003**, *13*, 85–88.
25. Chen, D.; Nakahara, A.; Wei, D.; Nordlund, D.; Russell, T. P. *Nano Lett.* **2011**, *11*, 561–567.
26. Hoppe, H.; Glatzel, T.; Niggemann, M.; Schwinger, W. *Thin Solid Films* **2006**, *511-512*, 585–592.
27. Hoppe, H.; Niggemann, M.; Winder, C.; Kraut, J. *Adv. Funct. Mater.* **2004**, *14*, 1005–1011.
28. van Duren, J. K. J.; Yang, X.; Loos, J.; Bulle-Lieuwma, C. W. T.; Sieval, A. B.; Hummelen, J. C.; Janssen, R. A. J. *Adv. Funct. Mater.* **2004**, *14*, 425–434.
29. Liu, F.; Gu, Y.; Wang, C.; Zhao, W.; Chen, D.; Briseno, A. L.; Russell, T. P. *Adv. Mater.* **2012**, *24*, 3947–3951.
30. Liu, F.; Zhao, W.; Tumbleston, J. R.; Wang, C.; Gu, Y.; Wang, D.; Briseno, A. L.; Ade, H.; Russell, T. P. *Adv. Energy Mater.* **2013**, *4*, 1301377.
31. Chen, W.; Xu, T.; He, F.; Wang, W.; Wang, C.; Strzalka, J.; Liu, Y.; Wen, J.; Miller, D. J.; Chen, J.; Hong, K.; Yu, L.; Darling, S. B. *Nano Lett.* **2011**, *11*, 3707–3713.
32. Liu, J.; Arif, M.; Zou, J.; Khondaker, S. I.; Zhai, L. *Macromolecules* **2009**, *42*, 9390–9393.
33. Sirringhaus, H.; Brown, P. J.; Friend, R. H.; Nielsen, M. M.; Bechgaard, K.; Langeveld-Voss, B. M. W.; Spiering, A. J. H.; Janssen, R. A. J.; Meijer, E. W.; Herwig, P.; de Leeuw, D. M. *Nature* **1999**, *401*, 685–688.
34. Samitsu, S.; Shimomura, T.; Heike, S.; Hashizume, T.; Ito, K. *Macromolecules* **2008**, *41*, 8000–8010.
35. Samitsu, S.; Shimomura, T.; Ito, K. *Thin Solid Films* **2008**, *516*, 2478–2486.

36. Samitsu, S.; Shimomura, T.; Heike, S.; Hashizume, T.; Ito, K. *Macromolecules* **2010**, *43*, 7891–7894.
37. Wu, P.-T.; Xin, H.; Kim, F. S.; Ren, G.; Jenekhe, S. A. *Macromolecules* **2009**, *42*, 8817–8826.
38. Qiu, L.; Lee, W. H.; Wang, X.; Kim, J. S.; Lim, J. A.; Kwak, D.; Lee, S.; Cho, K. *Adv. Mater.* **2009**, *21*, 1349–1353.
39. Chen, D.; Liu, F.; Wang, C.; Nakahara, A.; Russell, T. P. *Nano Lett.* **2011**, *11*, 2071–2078.
40. Xin, H.; Kim, F. S.; Jenekhe, S. A. *J. Am. Chem. Soc.* **2008**, *130*, 5424–5425.
41. Oh, J. Y.; Shin, M.; Lee, T. I.; Jang, W. S.; Min, Y.; Myoung, J.-M.; Baik, H. K.; Jeong, U. *Macromolecules* **2012**, *45*, 7504–7513.
42. Berson, S.; De Bettignies, R.; Bailly, S.; Guillerez, S. *Adv. Funct. Mater.* **2007**, *17*, 1377–1384.
43. Kim, J. S.; Lee, J. H.; Park, J. H.; Shim, C.; Sim, M.; Cho, K. *Adv. Funct. Mater.* **2010**, *21*, 480–486.
44. Li, G.; Shrotriya, V.; Huang, J.; Yao, Y.; Moriarty, T.; Emery, K.; Yang, Y. *Nature Mater.* **2005**, *4*, 864–868.
45. Li, G.; Yao, Y.; Yang, H.; Shrotriya, V.; Yang, G.; Yang, Y. *Adv. Funct. Mater.* **2007**, *17*, 1636–1644.
46. Page, Z. A.; Liu, Y.; Duzhko, V. V.; Russell, T. P.; Emrick, T. *Science* **2014**, *346*, 441–444.
47. Braun, S.; Salaneck, W. R.; Fahlman, M. *Adv. Mater.* **2009**, *21*, 1450–1472.
48. Li, C.-Z.; Chueh, C.-C.; Ding, F.; Yip, H.-L.; Liang, P.-W.; Li, X.; Jen, A. K. Y. *Adv. Mater.* **2013**, *25*, 4425–4430.
49. Ishii, H.; Sugiyama, K.; Ito, E.; Seki, K. *Adv. Mater.* **1999**, *11*, 605–625.
50. van Reenen, S.; Kouijzer, S.; Janssen, R. *Adv. Mater. Interfaces* **2014**, *1*, 1400189.
51. Xavier Crispin; Victor Geskin; Annica Crispin; Jérôme Cornil; Roberto Lazzaroni; William R Salaneck, A.; Jean-Luc Brédas. *J. Am. Chem. Soc.* **2002**, *124*, 8131–8141.
52. Hung, L. S.; Tang, C. W.; Mason, M. G. *Appl. Phys. Lett.* **1997**, *70*, 152–154.



53. He, Z.; Wu, H.; Cao, Y. *Adv. Mater.* **2014**, *26*, 1006–1024.
54. Zhou, Y.; Fuentes-Hernandez, C.; Shim, J.; Meyer, J.; Giordano, A. J.; Li, H.; Winget, P.; Papadopoulos, T.; Cheun, H.; Kim, J.; Fenoll, M.; Dindar, A.; Haske, W.; Najafabadi, E.; Khan, T. M.; Sojoudi, H.; Barlow, S.; Graham, S.; Bredas, J. L.; Marder, S. R.; Kahn, A.; Kippelen, B. *Science* **2012**, *336*, 327–332.
55. Tang, Z.; Tress, W.; Bao, Q.; Jafari, M. J.; Bergqvist, J.; Ederth, T.; Andersson, M. R.; Inganäs, O. *Adv. Energy Mater.* **2014**, *4*, 1400643.
56. Greiner, M. T. *Nature Mater.* **2011**, *11*, 76–81.
57. Puodziukynaite, E.; Wang, H.-W.; Lawrence, J.; Wise, A. J.; Russell, T. P.; Barnes, M. D.; Emrick, T. *J. Am. Chem. Soc.* **2014**, *136*, 11043–11049.
58. Campbell, I.; Rubin, S.; Zawodzinski, T.; Kress, J.; Martin, R.; Smith, D.; Barashkov, N.; Ferraris, J. *Phys. Rev., B Condens. Matter* **1996**, *54*, R14321–R14324.
59. Ellison, D. J.; Lee, B.; Podzorov, V. *Adv. Mater.* **2011**, *23*, 502–507.
60. He, Z.; Zhong, C.; Huang, X.; Wong, W.-Y.; Wu, H.; Chen, L.; Su, S.; Cao, Y. *Adv. Mater.* **2011**, *23*, 4636–4643.
61. Oh, S.-H.; Na, S.-I.; Jo, J.; Lim, B.; Vak, D.; Kim, D.-Y. *Adv. Funct. Mater.* **2010**, *20*, 1977–1983.
62. Guan, X.; Zhang, K.; Huang, F.; Bazan, G. C.; Cao, Y. *Adv. Funct. Mater.* **2012**, *22*, 2846–2854.
63. He, Z.; Zhang, C.; Xu, X.; Zhang, L.; Huang, L.; Chen, J.; Wu, H.; Cao, Y. *Advanced Materials* **2011**, *23*, 3086–3089.
64. He, Z.; Zhong, C.; Su, S.; Xu, M.; Wu, H.; Cao, Y. *Nature Photon.* **2012**, *6*, 591–595.
65. Cho, N.; Yip, H.-L.; Hau, S. K.; Chen, K.-S.; Kim, T.-W.; Davies, J. A.; Zeigler, D. F.; Jen, A. K. Y. *J. Mater. Chem.* **2011**, *21*, 6956–6961.
66. Duan, C.; Wang, L.; Zhang, K.; Guan, X.; Huang, F. *Adv. Mater.* **2011**, *23*, 1665–1669.
67. Liu, F.; Page, Z. A.; Duzhko, V. V.; Russell, T. P.; Emrick, T. *Adv. Mater.* **2013**, *25*, 6868–6873.
68. Zhang, K.; Guan, X.; Huang, F.; Cao, Y. *Acta Chim. Sinica* **2012**, *70*, 2489.

69. Liu, S.; Zhang, K.; Lu, J.; Zhang, J.; Yip, H.-L.; Huang, F.; Cao, Y. *J. Am. Chem. Soc.* **2013**, *135*, 15326–15329.
70. Liu, Y.; Page, Z. A.; Russell, T. P.; Emrick, T. *Angew. Chem. Int. Ed.* **54**, 11485–11489.
71. He, C.; Zhong, C.; Wu, H.; Yang, R.; Yang, W.; Huang, F.; Bazan, G. C.; Cao, Y. *J. Mater. Chem.* **2010**, *20*, 2617–2622.
72. Chang, Y.-M.; Zhu, R.; Richard, E.; Chen, C.-C.; Li, G.; Yang, Y. *Adv. Funct. Mater.* **2012**, *22*, 3284–3289.
73. Kang, H.; Hong, S.; Lee, J.; Lee, K. *Adv. Mater.* **2012**, *24*, 3005–3009.
74. Du, C.; Li, W.; Duan, Y.; Li, C.; Dong, H.; Zhu, J.; Hu, W.; Bo, Z. *Polym. Chem.* **2013**, *4*, 2773–2782.
75. Sun, J.; Zhu, Y.; Xu, X.; Lan, L.; Zhang, L.; Cai, P.; Chen, J.; Peng, J.; Cao, Y. *J. Phys. Chem. C* **2012**, *116*, 14188–14198.
76. Na, S.-I.; Kim, T.-S.; Oh, S.-H.; Kim, J.; Kim, S.-S.; Kim, D.-Y. *Appl. Phys. Lett.* **2010**, *97*, 223305.

## CHAPTER 2

### PREPARATION OF SEMI-CRYSTALLINE PCDTBT NANOFIBERS THROUGH SOLVENT-INDUCED CRYSTALLIZATION

#### 2.1 Introduction

The morphology of organic materials impacts their optoelectronic behavior, and thus the performance of corresponding electronic devices. Examining molecular packing of conjugated polymers, phase separation of the donor and the acceptor components, and fibrillar polymer networks provides insight into designing next generation materials and developing new device fabrication method. Precise description of molecular and microstructure is enabled by state-of-art X-ray/neutron techniques, as well as electron and scanning force microscopies.<sup>1</sup> Combining this valuable information with electronic characterization and modeling, early pioneering research revealed that ordered packing of conjugated polymers improves charge transport and charge-carrier mobility<sup>2</sup>— the enhanced  $\pi$  stacking in the conjugated backbone reduces electron hopping energy, and facilitating inter-chain charge transport.<sup>3</sup> For example, the hole mobility of poly-3-hexylthiophene (P3HT) thin films significantly increases after thermal<sup>4</sup> or solvent annealing as a result of improved crystallinity.<sup>5</sup> Applying such post-treatment to a blend of donor and acceptor components (such as in BHJ solar cells), however, coarsens the phase-separated domains, and decreases the device performance. Hence, new device

fabrication methods are required to optimize crystallization of the donor polymers while preserving nanoscale phase separated domains (10-30 nm).

A particular appealing strategy to enhance packing of conjugated polymers involves tuning solubility to induce crystallization. Methods such as cooling a polymer from a warm marginal solvent,<sup>7,9-12</sup> and adding a non-solvent to a well-solvated polymer,<sup>13,14</sup> lead to nucleation and crystal growth. Interestingly, the aromatic backbone of conjugated polymers often leads to a stronger preference for  $\pi$ - $\pi$  stacking, affording 1D semicrystalline nanostructures. A classic example is found in P3HT nanowires (P3HT-NWs), where the  $\pi$ - $\pi$  interaction from the thiophene backbone leads to crystal growth along the (010) plane, affording high aspect ratio nanofibers. Similar to solution-grown crystals of conventional aliphatic polymers, such as polyethylene, the thickness and width of P3HT-NWs depend on the crystallization temperature. Films prepared from these suspended P3HT-NWs showed dramatic increase in the hole mobility, surpassing values obtained from as-casted P3HT films.<sup>6-8</sup> Moreover, solar cells based on P3HT-NWs/PCBM reached similar performance as those thermally annealed cells. Such new device fabrication method not only eliminated the need to post-anneal, but also enhanced the performance of other poly-3-alkylthiophene derivatives, giving superior electronic devices that was not obtainable from conventional device fabrication methods.<sup>15,16</sup>

Ideally, principles underpinning the solution-based crystallization of P3HT will be applicable to low band gap polymers. However, reports to date on the morphology of low band gap polymers and their crystallization from solution are very limited. This chapter describes a simple solution-based preparation of

crystalline nanofibers from a low bandgap polymer, poly[N-9''-heptadecanyl-2,7-carbazole-alt-5,5-(4',7'-di-2-thienyl-2',1',3'-benzothiadiazole)] (PCDTBT). These solution-formed PCDTBT fibrils were characterized by transmission electron microscopy (TEM), atomic force microscopy (AFM), grazing-incidence wide-angle X-ray scattering (GI-WAXS), and steady-state absorption and fluorescence emission spectroscopies. We found the PCDTBT nanofibers exhibit granular texture along the fiber axis, suggesting they are formed from self-assembled nanocrystallites, possibly through  $\pi$ - $\pi$  or alkyl-alkyl interactions.

## 2.2 PCDTBT: from Synthesis to Preparation of Nanofibers

PCDTBT, developed by Leclerc and co-workers in 2007, has emerged as a promising donor material. The alternating donor-acceptor structures on the polymer backbone narrowed the band gap, allowing a broader absorption of the solar spectrum.<sup>17,18</sup> Indeed, organic solar cells based on PCDTBT/PC<sub>71</sub>BM reached 6-7 % PCE with 100 % internal quantum efficiency<sup>19</sup> and an estimated lifetime of > 6 years,<sup>20</sup> surpassing the benchmark P3HT/PCBM-based devices. However, compared to P3HT, PCDTBT has only weak short-range molecular order such that annealing above the glass transition temperature (~130 °C) disrupts the  $\pi$ - $\pi$  ordering.<sup>21</sup> High performing devices are usually thin films (< 80 nm) composed of amorphous PCDTBT and PC<sub>71</sub>BM. Thermal annealing drastically deteriorates PCE, likely due to coarsening of PCBM domains and reduced coherence length of the  $\pi$ -stacked chains in the polymer. Thus, developing new protocols for preparing semi-crystalline

PCDTBT in solution prior to mixing with PCBM may lead to device performance beyond 6-7 % PCE.

PCDTBT was readily synthesized by Suzuki polymerization of 2,7-bis(4',4',5',5'-tetramethyl-1',3',2'-dioxaborolan-2'-yl)-N-9''-heptadecanylcarbazole and 4,7-di(2'-bromothiophen-5'-yl)-2,1,3-benzothiadiazole, as previously reported (Scheme 2.1).<sup>17</sup> The number-average molecular weights ( $M_n$  values) were estimated relative to polystyrene standards by gel permeation chromatography (GPC) performed at 135 °C with trichlorobenzene as the mobile phase (Table 2.1).

Scheme 2.1 Synthesis route to PCDTBT using Suzuki coupling.<sup>18</sup>

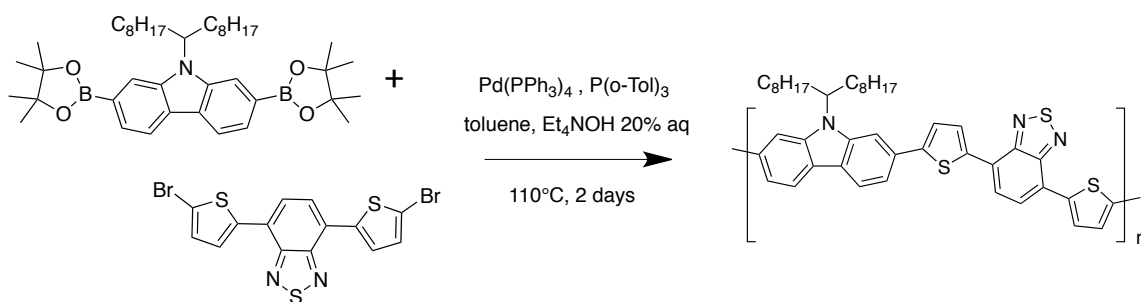


Table 2.1 Summary of polymerization results for PCDTBT.

Sample Code	$M_n$ (g/mol)	Polydispersity ( $\bar{D}$ )
PCD00	25 600	1.55
PCD01	4500	1.53
PCD02	60 100	1.62
PCD03	35 600	1.78
PCD04	55 000	1.55
PCD05	27 100	1.97
PCD06	5900	1.61
PCD07	12 600	2.42

Attempts to form PCDTBT fibrils using protocols established for P3HT were unsuccessful. For example, PCDTBT was dissolved in a marginal solvent, such as

anisole, and slowly cooled from elevated temperatures. In another case, PCDTBT was first dissolved in a good solvent, such as chloroform, followed by addition of a marginal solvent, like anisole. In each case, random aggregates or featureless structures were observed by transmission electron microscopy (TEM) (Figure 2.1). PCDTBT fibers were ultimately obtained by heating the polymer in a marginal solvent (dichloromethane, DCM) at 110°C in a sealed vessel (Scheme 2.2).

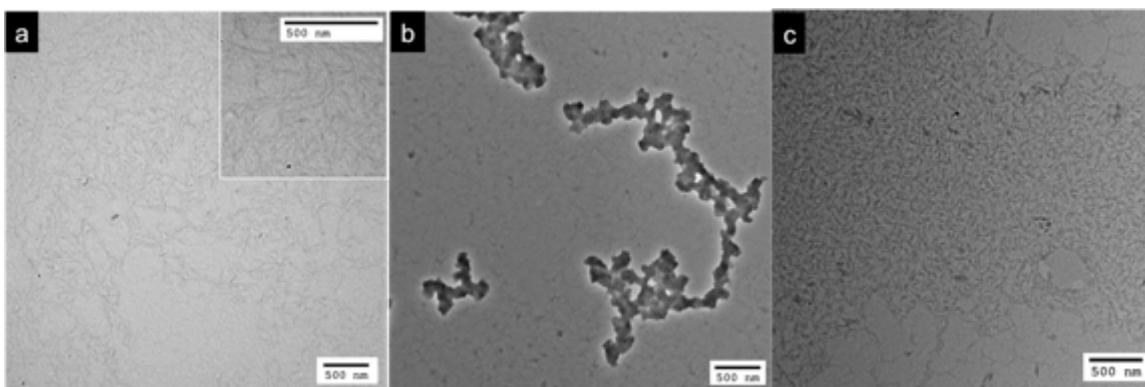
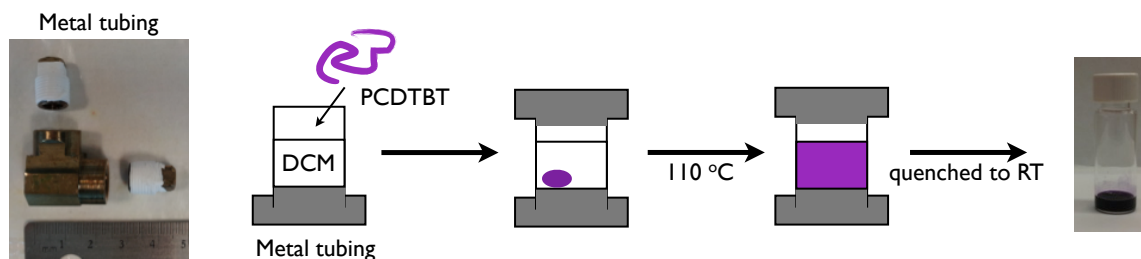


Figure 2.1 TEM images of drop cast solution of PCDTBT prepared by (a) heating in anisole (120 °C) and cooling to RT, (b) heating in *p*-xylene (120 °C) and cooling to RT, (c) dissolving in chloroform and then diluting with anisole.

Scheme 2.2 Preparation of PCDTBT nanofibers.



### 2.3 Characterization of PCDTBT Nanofibers

The influence of processing on the morphology of PCDTBT was first characterized by drop-casting the DCM solution onto a carbon-coated grid for TEM imaging. Individual PCDTBT fibril-like structures were observed, having widths of  $\sim 40\text{--}60$  nm and lengths of  $\sim 0.5$   $\mu\text{m}$  (Figure 2.2). The truncated lengths of these PCDTBT fibrils relative to P3HT fibrils ( $\sim 0.5$   $\mu\text{m}$  vs. multiple micrometers) suggest that the interchain packing is less well-defined or that multiple nucleation sites are present, preventing the formation of extended structures ( $> 1$   $\mu\text{m}$ ). GI-WAXS characterization of the PCDTBT fibrils, drop-cast on silicon wafer, revealed  $(h00)$  and  $(010)$  reflections in the  $q_z$  (out-of-plane) direction, giving an interchain separation distance of  $16.5$   $\text{\AA}$  ( $0.38$   $\text{\AA}^{-1}$ ) and an interchain  $\pi$ - $\pi$  stacking distance of  $4.3$   $\text{\AA}$  ( $1.46$   $\text{\AA}^{-1}$ ). These distances are comparable to those of thermally annealed films of PCDTBT.<sup>22</sup>

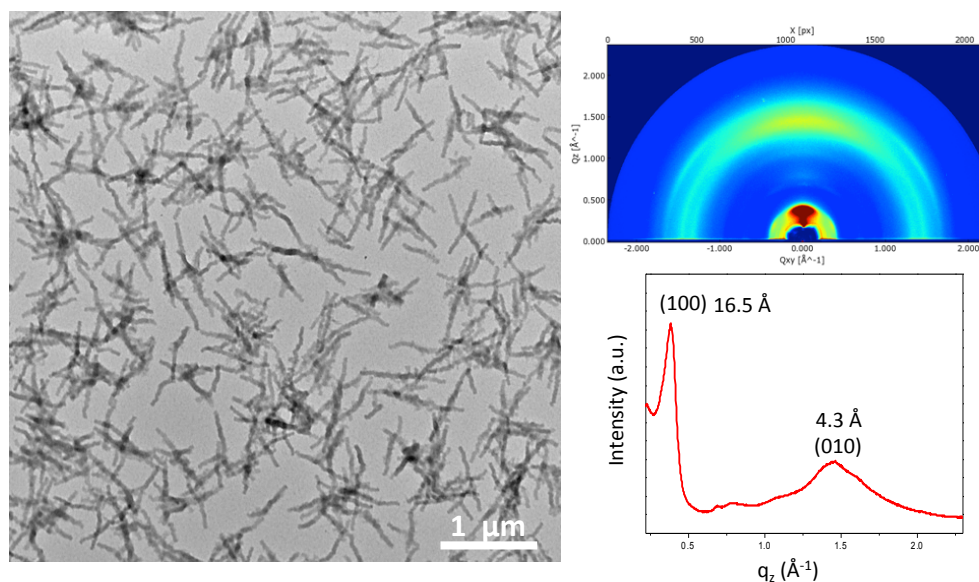


Figure 2.2 TEM image of PCDTBT nanofibers prepared from Scheme 2. The corresponding GI-WAXS data (*right*) indicates these structures are semicrystalline with lattice spacings comparable to bulk PCDTBT.



Further characterization of these PCDTBT nanostructures by atomic force microscopy (AFM) indicated that the dominant morphology consists of fibrillar structures 60–80 nm in width (Figure 2.3). The slightly larger values obtained relative to those obtained by TEM are attributed to the edge effect of the AFM probe. Interestingly, both height and phase images acquired in tapping mode showed these fibers are composed of substructures, implying that the fibrillar structure consists of smaller crystalline units. As shown in Figure 2.4, these granular substructures disappears upon annealing at 260 °C for 30 min (~10 °C above melting point of PCDTBT). The sub-structured nature of the PCDTBT fibrils suggests the assembly of individual PCDTBT chains into crystallites, either by  $\pi$ - $\pi$  stacking or alkyl-alkyl interactions, which further assemble, possibly by preferential interactions of different surfaces of the crystallites, to give the undulated fibrillar structures seen by AFM (Scheme 2.3).

If the polymer chains in PCDTBT fibrils are stacked and oriented perpendicular to the fibril axis, as in P3HT fibers, then the fiber width of 40–60 nm observed by TEM corresponds to approximately 20–30 repeat units of PCDTBT (given a repeat unit length ~2 nm). GPC of the PCDTBT samples suggested a higher DP (~ 35 or 25.6 kDa), a reasonable estimate given that the molecular weight of conjugated polymers of this type will be overestimated relative to polystyrene standards due to the rigid backbone. If the substructures are single crystals and the  $\pi$ - $\pi$  stacking direction is along the fibril axis, then the height of these modular features will correspond to an integral number of (100) planes, and the aspect ratio of the crystalline nanofiber is dictated by the relative rates of crystallization along

the (100) and (010) directions, while the fibril width is fixed by the length of the PCDTBT chains.

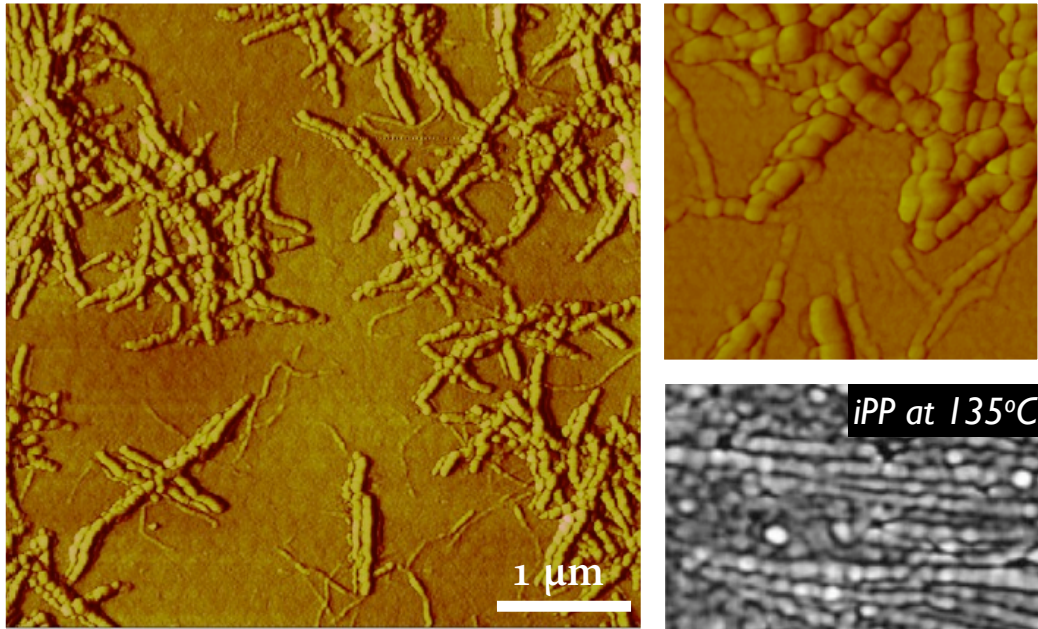


Figure 2.3 AFM images of PCDTBT nanofibers showing granular texture along the fiber axis. Similar crystalline texture was also observed in crystalline isotactic polypropylenes (lower right).

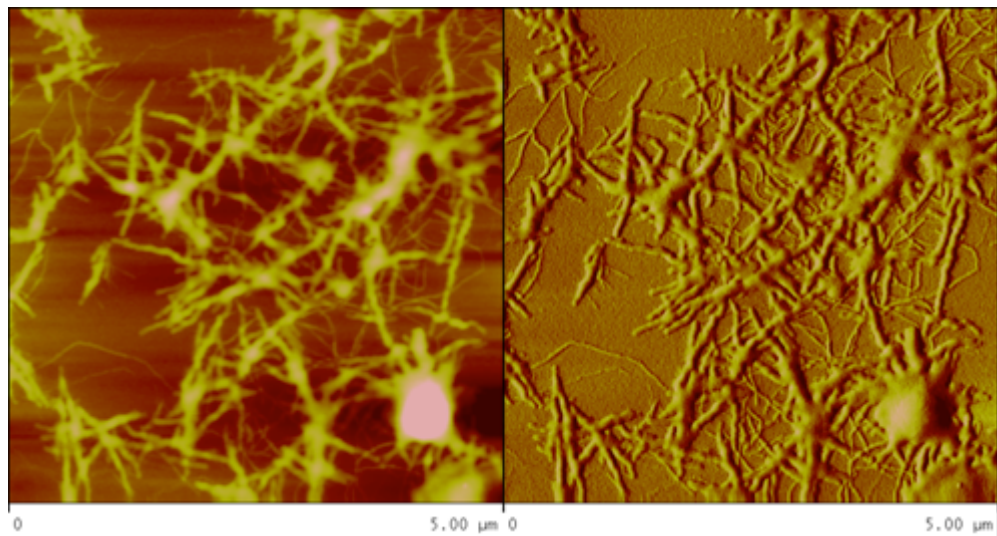


Figure 2.4 AFM height (*left*) and phase (*right*) images showing the disappearance of granular structures after annealing at 260 °C for 30 min.

Attempts to form fibrils from the higher molecular weight sample of PCDTBT using the same protocol were unfortunately unsuccessful. While PCDTBT with  $M_n < 6$  kDa is fully soluble in DCM at room temperature, PCDTBT with  $M_n > 60$  kDa was insoluble in DCM at 110°C. As for PCDTBT with  $M_n = 55$  kDa and PDI = 1.55, nanocrystallites initially formed after quenching to room temperature, aggregated with weak orientation preference and precipitated overtime (Figure 2.5). It was not possible to separate such clusters by dilution or sonication, suggesting that PCDTBT chains are partially incorporated into multiple nanofibers, generating intercrystalline links. This may result in less distinct surface energy between each crystallite surface, weakening the directional packing preference. Meanwhile, samples of PCDTBT with a higher polydispersity ( $\mathcal{D}$ ) ( $> 2$ ) showed decreased fiber lengths and less defined morphologies, presumably due to a broader distribution of polymer chain lengths preventing (010) growth.

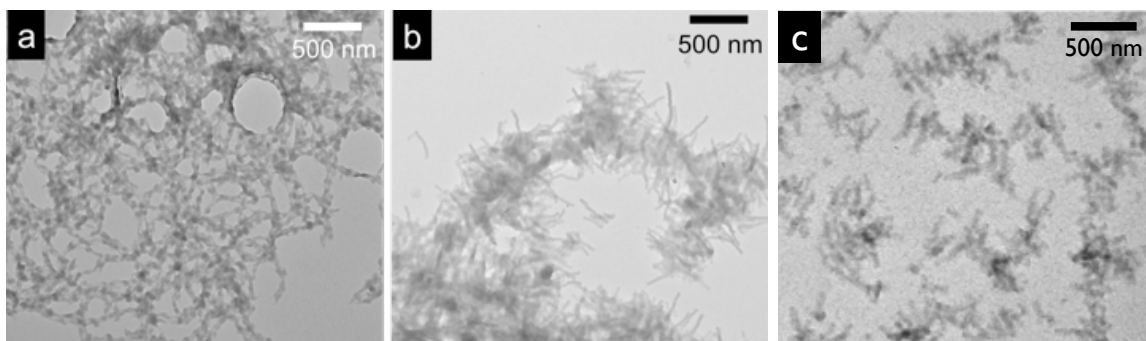


Figure 2.5 Nanostructures of PCDTBT ( $M_n = 55$  kDa,  $\mathcal{D} = 1.55$ ) after (a) 3 min, (b) 1 day aging, and (c) PCDTBT ( $M_n = 20$  kDa and  $\mathcal{D} = 2.1$ ) nanofibers solution after 1-day aging in ambient.

Distinct well-defined PCDTBT fibers were prepared from PCDTBT with  $M_n$  ranging from 15.6-35 kDa and  $\mathcal{D} < 2$ . Within this range, the width of the nanofibers

was between 40-60 nm, independent of the  $M_n$  and aging temperature. This is in strong contrast to P3HT nanofibers, where increasing the crystallization temperature and the polymer  $M_n$  widens the nanofibers.<sup>7</sup> It is possible that PCDTBT with a broader  $\bar{D}$  gives nanofibers a wider distribution of width, thus, makes studying the  $M_n$  effect on the fiber width challenging and inconclusive. P3HT, on the other hand, is not a typical conjugated polymer<sup>23</sup> because its persistence length is as low as 2.9 nm,<sup>24</sup> comparable to that of aliphatic polymers such as polyethylene (1.92 nm) and polystyrene (3.34 nm).<sup>23</sup>

To study the growth mechanism of PCDTBT fibers, a solution of PCDTBT was prepared at a much lower concentration (0.05 mg/mL). The solution was sampled at different time intervals for TEM studies. While samples taken 3 min after quenching showed the presence of two types of structures, one  $10 \times 50 \text{ nm}^2$  and the other  $40 \times 40 \text{ nm}^2$  (Figure 2.6 (a)), samples taken after aging at room temperature for 1 day showed bigger fibrils, as the dominant species (Figure 2.6 (b)). If these structures were grown from the initial crystallites in Figure 2.6 (a), then the density of the nanofibers in the solution would remain the same. In our case, however, the growth of the fibers occurred at the expense of the smaller structures, suggesting that these fibers were from fused smaller crystallites, in contrast to the general accepted mechanism for solution-grown P3HT fibers.

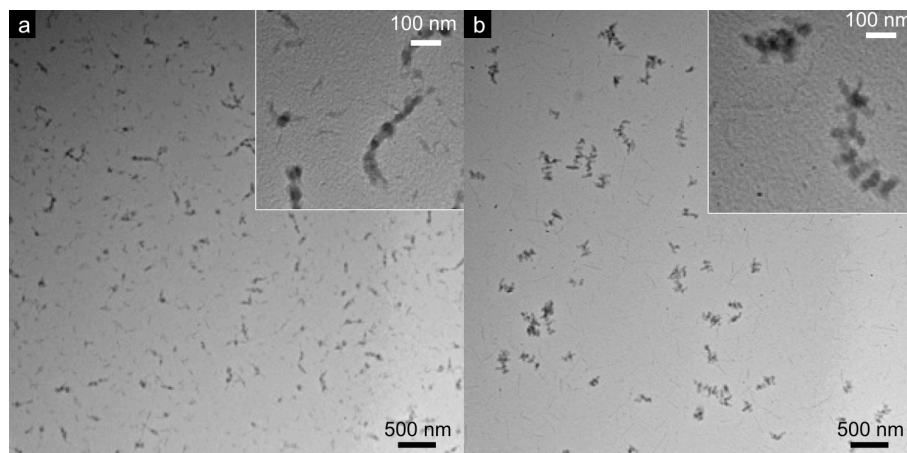
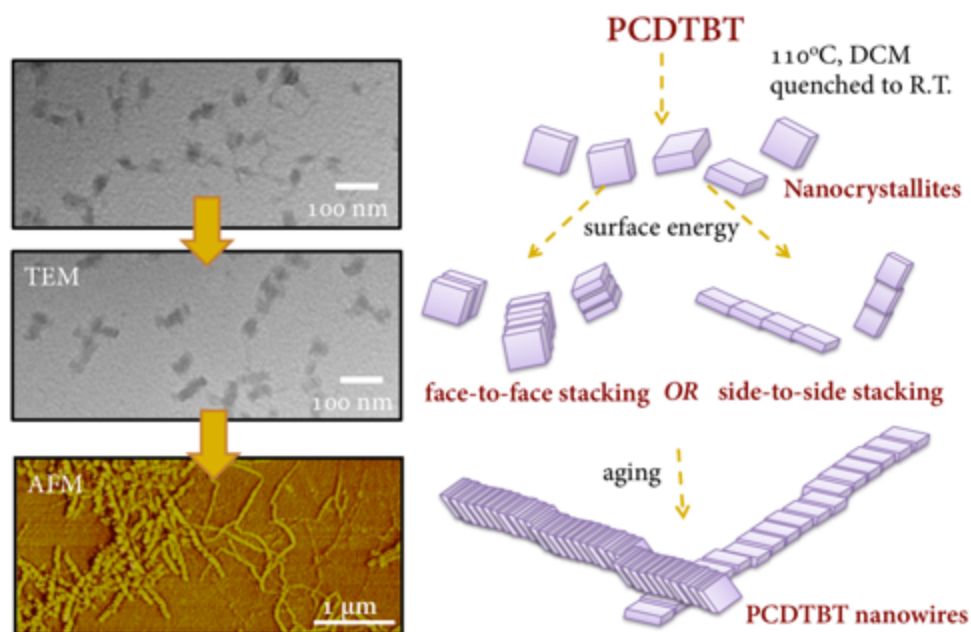


Figure 2.6 PCDTBT nanofibers (0.05 mg/mL) after quenched to room temperature and aged for (a) 3 min and (b) 1 day.

Scheme 2.3 Proposed mechanism of PCDTBT nanofiber formation.



Characterization of PCDTBT fibrils by absorption and fluorescence emission spectroscopy showed little change between the solvated polymer and the fibrils (Figure 2.7). This markedly contrasts the changes in absorption spectra observed upon P3HT fibril formation. The fluorescence emission spectrum of PCDTBT fibrils

shows essentially no change compared to the solvated polymer. In crystalline P3HT, strong intrachain and interchain electronic coupling produce spectral changes relative to solvated polymer; hence, the lack of significant spectral signatures of the PCDTBT fibrils implies that  $\pi$ - $\pi$  stacking and alkyl-alkyl interactions in these crystals have little influence on the electronic structure within the polymer chains or between neighboring chains. Moreover, it should be noted that P3HT contains only one vibronic band, while PCDTBT has over 15; thus, if vibronic bands do appear upon PCDTBT crystallization, their overlapping nature may lead to a featureless spectrum. The lack of spectroscopic signatures in the absorption spectrum further reflects the uniqueness of P3HT from these low band gap polymer structures.

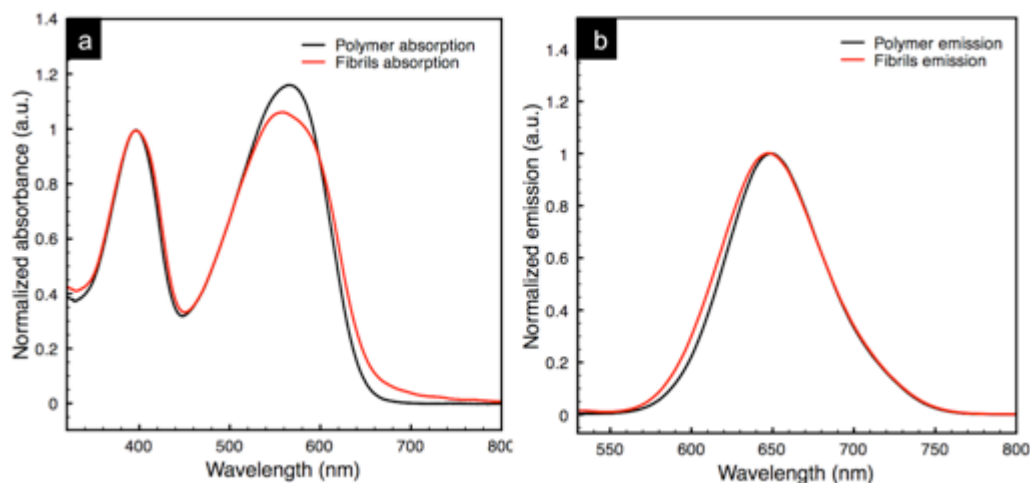


Figure 2.7 (a) UV/Vis and (b) photoluminescence spectra of solvated PCDTBT in chloroform (*black*) and PCDTBT nanofibers in DCM (*red*).

## 2.4 PCDTBT Derivatives and Their Nanofibers

The final morphology of solvent induced semicrystalline conjugated polymers often depends on the competition between  $\pi$ - $\pi$  stacking and alkyl-alkyl interactions. For example, the aspect ratio of P3HT nanowires increases as the

molecular weight increases due to stronger intermolecular  $\pi$ - $\pi$  interactions. On the other hand, if van der Waals intermolecular interactions between the pendent alkyl groups dominate, crystal growth along the ( $h00$ ) plane will be promoted, affording 2D semi-crystalline nanosheets. Lengthening the linear alkyl side chains on the thiophene backbone was found to increase the (100) spacing (the alkyl-alkyl distance), while attaching branched pendent chains increases (010) spacing. For example, poly-(3-(2'-ethyl)hexyl)thiophene displays a much bigger (010) spacing than that of P3HT (4.1 > 3.8 Å). This behavior was also observed in a low band gap copolymers based on thieno[3,-*b*]thiophene (TT) and benzodithiophene (BDT) units.<sup>25</sup> Thus, it is expected that tailoring the alkyl pendent side chains on the carbazole unit can lead to different molecular packing and crystal morphologies.

We chose to first explore the effect of linear pendent groups on PCDTBT crystallization by replacing the branched di-octyl chains to linear hexyl groups. Such polymer architecture resembles that of P3HT with linear substituents attached to the conjugated backbones. The resultant polymer, referred to as PCD<sup>6</sup>TBT (Scheme 2.4), showed significant reduced solubility. It crashed out in toluene during synthesis, and almost non-soluble in chlorinated solvents such as chloroform, chlorobenzene, and dichlorobenzene at room temperature. Interestingly, employing the same protocol described in the previous section affords 1D PCD<sup>6</sup>TBT nanostructures with a few flat lamellar nanosheets. These high aspect ratio nanofibers were smooth without undulation texture along the fiber axis. This suggests the shorter linear hexyl-side chains rendered PCD<sup>6</sup>TBT more amenable to ordering in contrast to PCDTBT (Figure 2.8).

Scheme 2.4 PCDTBT derivatives: PCD<sup>6</sup>TBT (*left*) and PCD<sup>8,12</sup>TBT (*right*)

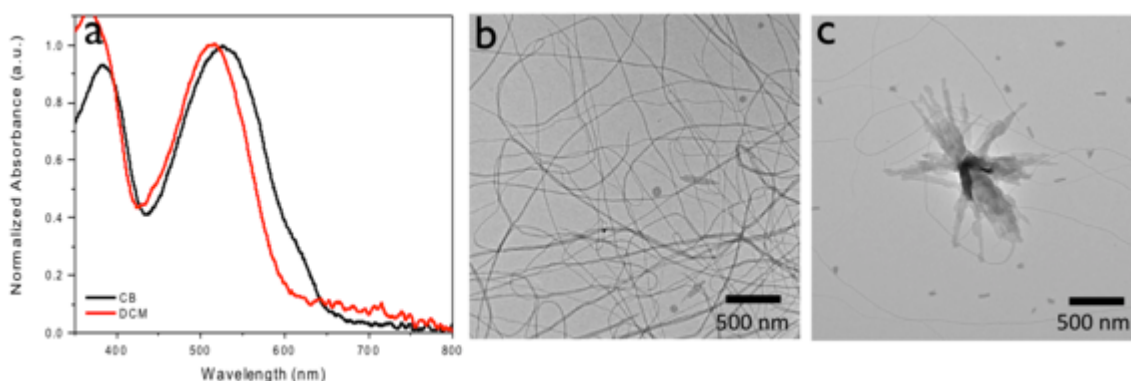
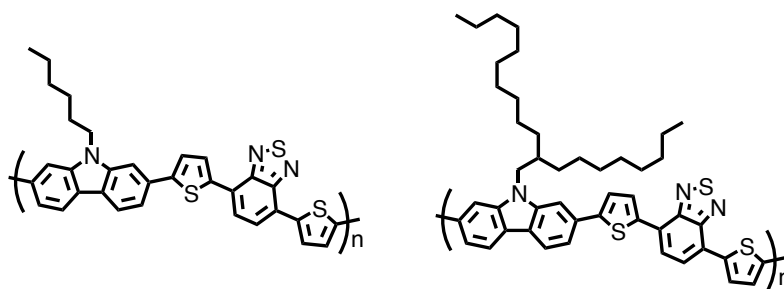


Figure 2.8 (a) UV/Vis spectra of PCD<sup>6</sup>TBT in chlorobenzene (*black*) and PCD<sup>6</sup>TBT nanostructures in DCM (*red*). TEM images showing (b) PCD<sup>6</sup>TBT nanofibers, and (c) PCD<sup>6</sup>TBT nanosheets.

Indeed, incorporating branched pendent chains is known to induce steric hinderance in the  $\pi$ - $\pi$  stacking of conjugated polymer backbone. Due to the synthesis constrain, many of these studies employ thiophene backbone with pendent alkyls branched at  $\beta$  position. PCDTBT presents a rare opportunity where the influence of the branching point on the crystal morphology, to the best of our knowledge, could be studied for the first time. By replacing the di-octyl ( $\alpha$  position) chains with 2-octyldodecyl ( $\beta$  position) groups afford PCD<sup>8,12</sup>TBT, a PCDTBT derivative with different branching point in the side-chain architecture. Similar to



PCD<sup>6</sup>TBT, PCB<sup>8,12</sup>TBT is less soluble in chlorinated solvents in comparison to PCDTBT. Utilizing the same protocol also gives PCD<sup>8,12</sup>TBT nanostructures. In contrast to fibers grown from PCDTBT and PCD<sup>6</sup>TBT, PCD<sup>8,12</sup>TBT fibers displayed darker contrast around the edges with the presence of smaller coiled fibers (Figure 2.9). We surmise that these smaller nanocoils assembled to form the larger fibers, which are anticipated to be hollow nanotubes as TEM images showed darker contrast at the rim. Unfortunately, lack of solubility in 1,2,4-trichlorobenzene precluded PCD<sup>6</sup>TBT and PCD<sup>8,12</sup>TBT from detailed molecular weight analysis by using high temperature GPC. Further investigation is needed to understand these intriguing structures.

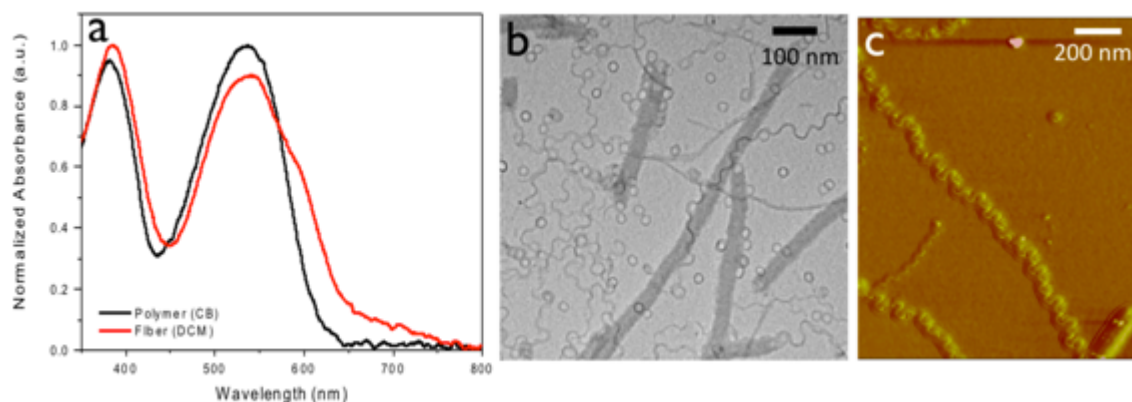


Figure 2.9 (a) UV/Vis spectra of PCD<sup>8,12</sup>TBT in chlorobenzene (*black*) and PCD<sup>8,12</sup>TBT nanostructures (*red*) in DCM. (b) TEM and (c) AFM images of PCD<sup>8,12</sup>TBT nanocoils and nanofibers.

## 2.5 Impact of PCBM on PCDTBT Nanofibers

The initiative of grow PCDTBT semicrystalline fibers in solution was intended to achieve semicrystalline donor domains in the active layer, without the tedious post-annealing process that improves ordering at the expense of domain coarsening. Thus, an improvement of the device efficiency in the PCBM/PCDTBT nanofibers

based PSCs was anticipated. However, our attempt in fabricating devices with PCDTBT nanofibers was unsuccessful, mainly due to the limitations arose from the nanofiber fabrication protocol. First, PCDTBT nanofibers were prepared at a low concentration (1 mg/mL) that casting films with thickness required for active layers (~ 80-100 nm) remained challenging. Second, the boiling point of DCM is so low that the solvent evaporated too fast that uniform films could not be achieved.

To examine other possible mechanisms for low device performance, we used TEM and GI-WAXS to study the effect of PCBM on PCDTBT nanofibers. Specifically, PCBM was mixed in solution with suspended PCDTBT fibers and stirred overnight at room temperature at 2 different blending ratios, PCDTBT/PCBM = 1:2 and 1:4. The latter ratio was reported to give the optimal device performance. In both solutions, TEM images revealed the presence of sharp PCDTBT fibers and ill-defined “swollen” fibers (lighter in contrast). This suggests a decrease in the chain packing density for the lighter PCDTBT fibers. In accord with this result, GI-WAXS revealed a pronounced reduction in the (100) intensity of semicrystalline PCDTBT nanofibers upon blending with PCBM. At the low PCBM concentration (PCDTBT/PCBM = 1:2), the (100) peak shifted to lower  $q$ , implying a larger (100) spacing. Such phenomenon has been observed in other conjugated polymers when PCBM diffuses into the alkyl regions. Further increasing the PCBM ratio from 66% to 80% resulted in the disappearance of the (100) peak (Figure 2.10). This observation suggests that the presence of PCBM disrupts the ordering of PCDTBT. This is in strong contrast to P3HT/PCBM, where the diffusion of PCBM into P3HT did not disrupt the morphology established by the semicrystalline P3HT.<sup>26</sup>

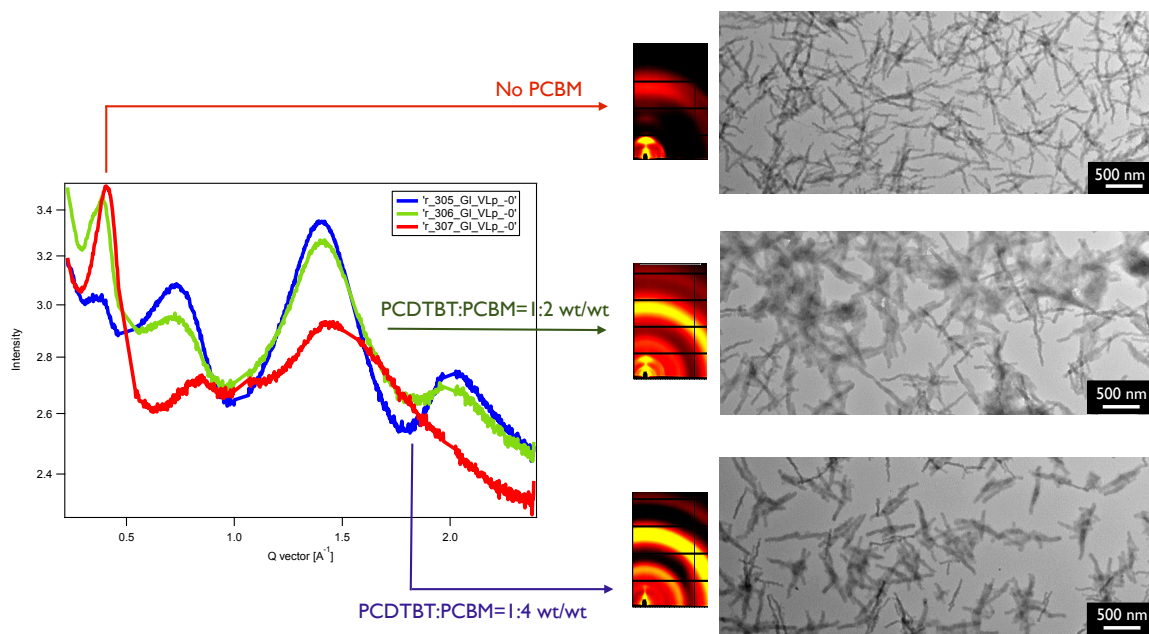


Figure 2.10 GI-WAXS and TEM of PCDTBT fibers before and after blending with PCBM at weight ratios of 1:2 and 1:4. Increasing PCBM concentration diminished the (100) and (010) reflections.

To understand the interaction between PCDTBT and PCBM, a bilayer system was prepared from a thin film of semicrystalline PCDTBT ( $\sim 80$  nm) on top of a PCBM thin film ( $\sim 40$  nm). Specifically, the semicrystalline PCDTBT films were prepared by annealing spin-coated PCDTBT film on PEDOT:PSS coated glass slides at  $250^\circ\text{C}$  for 30 min. The PCDTBT films were subsequently lifted from the substrates by slowly immersing the PCDTBT-coated substrate in water, and transferred onto PCBM-coated substrates. GI-WAXS performed on the bilayer films, at an  $18^\circ$  incident angle, revealed intense crystalline peaks arising from the (100) and (010) lattice spacings at  $15.6 \text{ \AA}$  and  $4.5 \text{ \AA}$ , respectively. There were also two off axis peaks at  $q_x \sim 0.15 \text{ (\AA}^{-1}\text{)}$ , which was suggested by Ocko and coworkers as an indicator of orthorhombic packing of the conjugated backbone.<sup>22</sup> Interestingly, *in situ* GI-WAXS patterns taken during annealing of the thin films at  $160^\circ\text{C}$  showed that the (100)

spacing initially intensified, but then diminished, at the same time, the maximum peak shifted to a lower  $q$ . This was accompanied by the appearance of amorphous peaks at  $0.78, 1.42,$  and  $2.12 \text{ \AA}^{-1}$ , corresponding to PCBM halos, indicating that PCBM diffused to the top of the film during annealing (Figure 2.11). This result supports our hypothesis that PCBM disrupts the ordering of PCDTBT that resulting in the loss of crystallinity in PCDTBT nanofibers upon blending with PCBM.

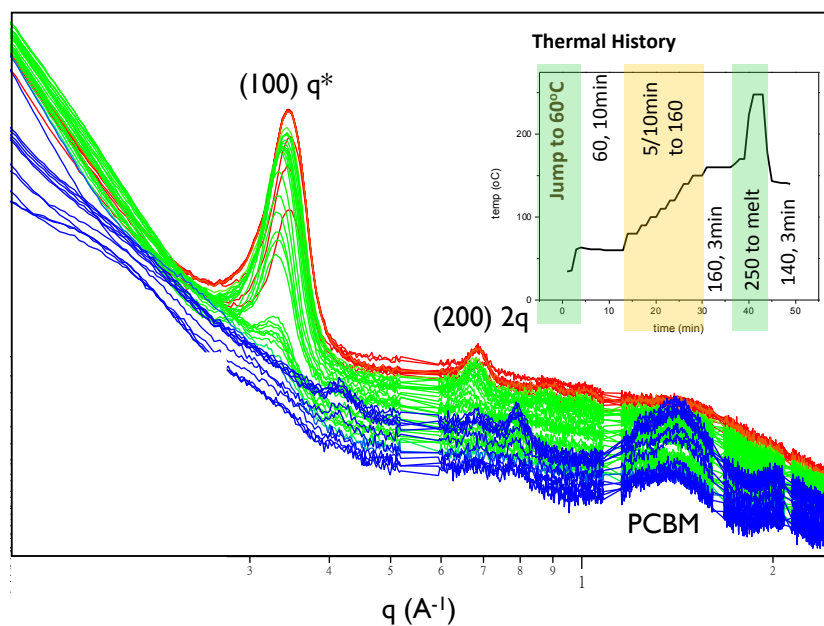


Figure 2.11 *In situ* GI-WAXS profiles of the bilayer film composed of semicrystalline PCDTBT (*top layer*) and PCBM (*bottom layer*) from room temperature to  $160^{\circ}\text{C}$  at  $5^{\circ}\text{C}/\text{min}$ . As (100) and (200) peaks of PCDTBT disappear, the PCBM reflection increased in intensity.

## 2.6 Conclusions

PCDTBT semicrystalline fibers were prepared by solvent-induced crystallization. These nanostructures were truncated with undulated features along the fiber axis. Their X-ray scattering patterns suggest similar crystalline motif as

those in bulk semicrystalline PCDTBT thin films. From the granular texture, and time dependent studies, these fibers are speculated to arise from packing of smaller crystals due to the  $\pi$ - $\pi$  interactions of the backbone or the alkyl-alkyl interaction between the side chains. As expected, changing the alkyl substituents on the cabarzole afforded different fiber morphology. However, upon blending PCDTBT fibers with PCBM, the crystallinity of the nanofiber was lost. PCBM is suspected to penetrate into the alkyl region of PCDTBT and disrupt the crystalline motif. This is supported *in-situ* scattering of PCDTBT/PCBM bilayers, where upon heating to 160 °C (below the melting point of PCDTBT), the (100) peak diminished with increasing scattering intensity from PCBM.

## 2.7 References

1. Rivnay, J.; Mannsfeld, S. C.; Miller, C. E.; Salleo, A.; Toney, M. F. *Chem. Rev.* **2012**, *112*, 5488–5519.
2. Bao, Z.; Dodabalapur, A.; Lovinger, A. J. *Appl. Phys. Lett.* **1996**, *69*, 4108–4110.
3. Sirringhaus, H.; Brown, P. J.; Friend, R. H.; Nielsen, M. M.; Bechgaard, K.; Langeveld-Voss, B. M. W.; Spiering, A. J. H.; Janssen, R. A. J.; Meijer, E. W.; Herwig, P.; de Leeuw, D. M. *Nature* **1999**, *401*, 685–688.
4. Cho, S.; Lee, K.; Yuen, J.; Wang, G.; Moses, D.; Heeger, A. J.; Surin, M.; Lazzaroni, R. *J. Appl. Phys.* **2006**, *100*, 114503.
5. Li, G.; Shrotriya, V.; Huang, J.; Yao, Y.; Moriarty, T.; Emery, K.; Yang, Y. *Nature Mater.* **2005**, *4*, 864–868.
6. Briseno, A. L.; Mannsfeld, S. C. B.; Shamberger, P. J.; Ohuchi, F. S.; Bao, Z.; Jenekhe, S. A.; Xia, Y. *Chem. Mater.* **2008**, *20*, 4712–4719.
7. Liu, J.; Arif, M.; Zou, J.; Khondaker, S. I.; Zhai, L. *Macromolecules* **2009**, *42*, 9390–9393.
8. Traiphol, R.; Charoenthai, N.; Srihirin, T.; Kerdeharoen, T.; Osotchan, T.; Maturros, T. *Polymer* **2007**, *48*, 813–826.

9. Berson, S.; De Bettignies, R.; Bailly, S.; Guillerez, S. *Adv. Funct. Mater.* **2007**, *17*, 1377–1384.
10. Kim, J. S.; Lee, J. H.; Park, J. H.; Shim, C.; Sim, M.; Cho, K. *Adv. Funct. Mater.* **2010**, *21*, 480–486.
11. Qiu, L.; Lee, W. H.; Wang, X.; Kim, J. S.; Lim, J. A.; Kwak, D.; Lee, S.; Cho, K. *Adv. Mater.* **2009**, *21*, 1349–1353.
12. Ihn, K. J.; Moulton, J.; Smith, P. *J. Polym. Sci. B Polym. Phys.* **1993**, *31*, 735–742.
13. Kiriya, N.; Jähne, E.; Adler, H.-J.; Schneider, M.; Kiriya, A.; Gorodyska, G.; Minko, S.; Jehnichen, D.; Simon, P.; Fokin, A. A.; Stamm, M. *Nano Lett.* **2003**, *3*, 707–712.
14. Li, L.; Lu, G.; Yang, X. *J. Mater. Chem.* **2008**, *18*, 1984–1990.
15. Xin, H.; Kim, F. S.; Jenekhe, S. A. *J. Am. Chem. Soc.* **2008**, *130*, 5424–5425.
16. Wu, P.-T.; Xin, H.; Kim, F. S.; Ren, G.; Jenekhe, S. A. *Macromolecules* **2009**, *42*, 8817–8826.
17. Blouin, N.; Michaud, A.; Gendron, D.; Wakim, S.; Blair, E.; Neagu-Plesu, R.; Belletête, M.; Durocher, G.; Tao, Y.; Leclerc, M. *J. Am. Chem. Soc.* **2008**, *130*, 732–742.
18. Blouin, N.; Michaud, A.; Leclerc, M. *Adv. Mater.* **2007**, *19*, 2295–2300.
19. Park, S. H.; Roy, A.; Beaupré, S.; Cho, S.; Coates, N.; Moon, J. S.; Moses, D.; Leclerc, M.; Lee, K.; Heeger, A. J. *Nature Photon.* **2009**, *3*, 297–302.
20. Peters, C. H.; Sachs-Quintana, I. T.; Kastrop, J. P.; Beaupré, S.; Leclerc, M.; McGehee, M. D. *Adv. Energy Mater.* **2011**, *1*, 491–494.
21. Beiley, Z. M.; Hoke, E. T.; Noriega, R.; Dacuña, J.; Burkhard, G. F.; Bartelt, J. A.; Salleo, A.; Toney, M. F.; McGehee, M. D. *Adv. Energy Mater.* **2011**, *1*, 954–962.
22. Lu, X.; Hlaing, H.; Germack, D. S.; Peet, J.; Jo, W. H.; Andrienko, D.; Kremer, K.; Ocko, B. M. *Nat. Commun.* **2012**, *3*, 795.
23. Treat, N. D.; Chabinyo, M. L. *Annu Rev Phys Chem* **2014**, *65*, 59–81.
24. McCulloch, B.; Ho, V.; Hoarfrost, M.; Stanley, C.; Do, C.; Heller, W. T.; Segalman, R. A. *Macromolecules* **2013**, *46*, 1899–1907.
25. Szarko, J. M.; Guo, J.; Liang, Y.; Lee, B.; Rolczynski, B. S.; Strzalka, J.; Xu, T.; Loser, S.; Marks, T. J.; Yu, L.; Chen, L. X. *Adv. Mater.* **2010**, *22*, 5468–5472.

26. Chen, D.; Liu, F.; Wang, C.; Nakahara, A.; Russell, T. P. *Nano Lett.* **2011**, *11*, 2071–2078.

## CHAPTER 3

### ZWITTERIONIC METHACRYLATE AND AZULENE COPOLYMERS

#### 3.1 Introduction

The performance and the lifetime of organic-based electronics rely heavily on both the photoactive layer and the interface between the active layer and the electrodes. Surprisingly, the significant advances in fabricating efficient photoactive layers has not been balanced by an equal progress in engineering the organic-electrode interfaces.<sup>1</sup> While intensive research afforded highly efficient photoactive layers, reaching unity in internal quantum efficiency,<sup>2</sup> methods leading to robust organic-electrode interfaces are still under development. Careful interface designs to align energy levels of the photoactive layer with the metal electrode (allowing Ohmic contact), to reduce charge injection/extraction barrier, and to improve charge collection efficiency are essential to reach high performance organic electronics. Specifically, achieving effective charge transport and extraction in polymer-based solar cells (PSCs) requires a strong built-in potential across the cell.<sup>3,4</sup> In fact, if the difference between the work functions (WF) of the cathode and the anode is less than the energy difference between the lowest unoccupied molecular orbital (LUMO) of the acceptor ( $E_{\text{LUMO}}^{\text{acceptor}}$ ) and the highest occupied molecular orbital (HOMO) of the donor ( $E_{\text{HOMO}}^{\text{donor}}$ ), then the  $V_{\text{oc}}$  of the PSC will be limited by the electrodes instead of the energy offset between  $E_{\text{LUMO}}^{\text{acceptor}}$  and  $E_{\text{HOMO}}^{\text{donor}}$ .<sup>5</sup> This implies in addition to designing novel materials allowing higher offset between



$E_{\text{LUMO}}^{\text{acceptor}}$  and  $E_{\text{HOMO}}^{\text{donor}}$ , tailoring the electronic properties at the organic-electrode interfaces are important in constructing more efficient PSCs.

To date, many low WF metals (*i.e.*, calcium (Ca),<sup>6</sup> barium (Ba),<sup>6</sup> and magnesium (Mg)) have been explored as cathodes to provide a high potential bias across the PSCs. However, their susceptibility to atmospheric oxidation often led to short device lifetime.<sup>7,8</sup> Pioneering studies showed that by inserting small inorganic molecules such as lithium fluoride (LiF) and cesium fluoride (CsF) at the organic-electrode interface could achieve similar or better device performance as those employing low WF metals. For example, Tang *et al.* demonstrated LiF/Al afforded high performance organic light emitting diodes (OLEDs) as those using Ca/Al as cathodes.<sup>7</sup> This was attributed to the formation of dipole layer at the organic-metal interface, lowering the WF of Al and the charge injection energy barrier. In a typical device fabrication, these small molecules were evaporated on the organic photoactive layer, followed by deposition of the metal cathode. However, this costly vacuum processing, and the moisture sensitivity of these small molecules limited their applications.<sup>9</sup> Another approach to reach long-term device stability involves utilizing polymers with permanent dipoles to modify air-stable metal electrodes (*i.e.*, silver (Ag), gold (Au) and copper (Cu)). The orthogonal solution processibility of these polymers enables multilayer device fabrications, presenting a potential platform for roll-to-roll processing of flexible solar cells.

In this chapter, we examine methacrylate copolymers bearing zwitterionic functionalities as electrode modifiers. Polyzwitterions are promising candidates due to their strong permanent dipoles and orthogonal solubility with respect to the

active layer.<sup>10-17</sup> Furthermore, being pH-insensitive, charge neutral and counterion free, they serve as more robust alternatives than polyelectrolytes for work function reduction and device implementation. While most explored polymeric sulfobetaine cathode modifiers possess conjugated backbone,<sup>10,12,13,18-20</sup> the polymers investigated here are synthesized from free radical polymerization, easily scalable to multi-gram production.

### **3.2 Polysulfobetaine Methacrylate (PSBMA) as Cathode Modifiers**

Polysulfobetaine methacrylate (PSBMA) can be readily synthesized from commercially available [2-(Methacryloyloxy)ethyl]dimethyl-(3-sulfopropyl) ammonium hydroxide (SB-methacrylate) through reversible addition-fragmentation chain-transfer polymerization (RAFT), using 4-cyano-4-(phenylcarbonothioylthio) pentanoic acid as the chain transfer agent and 4,4'-azobis(4-cyanovaleric acid) as the initiator. The reaction is typically performed under nitrogen in 2,2,2-trifluoroethanol (TFE) (2 mL) at 70 °C overnight, followed by precipitation in acetone. The PSBMA used in the following study has  $M_n = 26.0$  kDa and  $\bar{D} = 1.1$ .

Photoelectron spectroscopy was employed to study the impact of PSBMA coating on the electronic properties of silver (Ag) substrate. Ag is a good electrode material for PSCs applications, offering high reflectance (thus high  $J_{sc}$ ), long-term device stability,<sup>21</sup> and solution processibility for roll-to-roll processing.<sup>9,22,23</sup> The kinetic energy of photoelectrons escaping from illuminated PSBMA/Ag surface was probed by the photoelectron spectroscopy to determine the core-energy and molecular valance levels of the sample.<sup>7,24</sup> As the probability of electrons escaping

from the surface decreases drastically with the sampling depth, the spectrum is generally overwhelmed with signals originated within 3 times of the inelastic mean free path ( $3\lambda$ ), rendering the technique extremely surface sensitive. Typically, for X-ray photoelectron spectroscopy (XPS)  $\lambda$  is on the order of 10 angstroms ( $\text{\AA}$ ), and for ultraviolet photoelectron spectroscopy (UPS)  $\lambda < 10 \text{\AA}$ .<sup>25</sup>

XPS and UPS probe electrons at different energy levels. Specifically, XPS utilizes soft-X-ray at  $\sim 1$  keV, where the photoionization cross section of C(2s) electrons is an order of magnitude stronger than C(2p) electrons, affording spectra dominated with C(2s)-derived valence states. Thus, XPS reflects chemical bonding, doping, or band bending as a result of equilibrating Fermi levels across interfaces. For example, if charge transfer from the metal to the organic molecules, a shift in the binding energy would be detected by XPS. On the other hand, UPS utilizes lower photon energy ( $\sim 20$  eV), resulting in a 10 times stronger photoionization cross section for C(2p) than C(2s) electrons, rendering UPS ideal for examining the vacuum level, work function of metals and HOMO of semiconductors. In short, XPS probes core-energy level electrons, while UPS detects  $\pi$  spectroscopic features.

The representative UPS spectra of Ag and PSBMA coated Ag substrates (PSBMA/Ag) are shown in Figure 3.1. The higher energy onset is referred to as the secondary electron energy cutoff ( $E_{\text{Sec, Ag}}$ ), corresponding to the energy of excited electrons escaped from deep occupied states. The energy level where both the binding and kinetic energy of electrons are zero is defined as the vacuum level ( $E_{\text{Vac}}$ ). It is calculated by subtracting the energy of the light source ( $h\nu = 21.2$  eV) from the  $E_{\text{Sec, Ag}}$ . On the other hand, Fermi level of Ag ( $E_{\text{F, Ag}}$ ) is given by the lower energy onset

of the Ag UPS spectrum. The difference between  $E_{F, Ag}$  and  $E_{Vac}$  determines the work function (WF) of Ag ( $\Phi_{Ag}$ ): the minimum energy required to remove an electron from the Ag surface to the  $E_{Vac}$ . Figure 3.1 (b) showed a significant shift in the  $E_{Sec}$  (from 16.5 eV to 17.5 eV) for PSBMA ( $\sim 5$  nm)/Ag, indicating an offset of vacuum level at the PSBMA/Ag interface. This implies PSBMA induced a  $\sim 1$  eV change in  $\Phi_{Ag}$ . Such dramatic change is unlikely solely due to the push-back effect. Thus, we utilized XPS to monitor the C(1s) and Ag (3d) spectrum features to detect band bending at the interface. Interestingly, these peaks remained at the same position after applying PSBMA coating, suggesting negligible charge transfer and band bending (Figure 3.2). In fact, alignment of polar functionalities at the interface (e.g., carbonyl ( $\mu \sim 1.7$  D) and sulfobetaine ( $\mu \sim 24$  D)) may be the key to such work function reduction. Studies of poly(methyl methacrylate) (PMMA) and poly(n-butyl methacrylate) (PnBMA) coated Ag also showed similar  $\Delta\phi \sim 1$  eV (Figure 3.3).

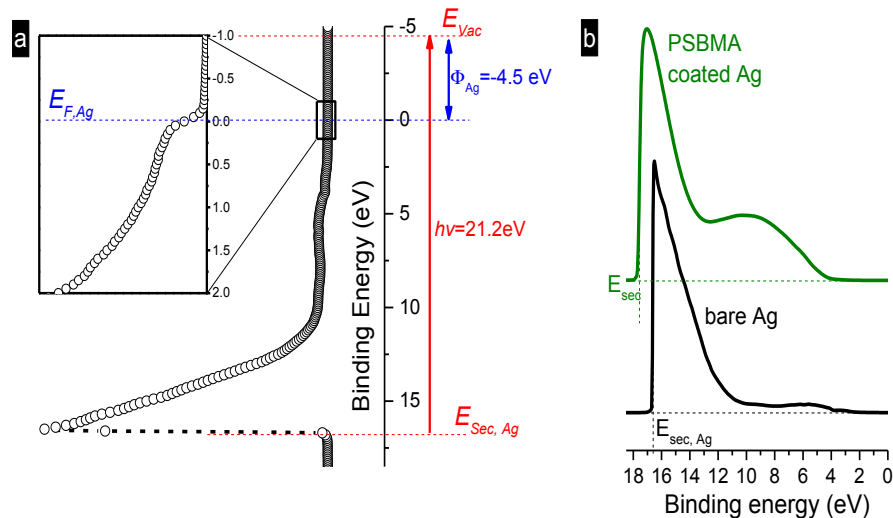


Figure 3.1 (a) A typical UPS spectrum of Ag showing the secondary electron energy cutoff ( $E_{Sec, Ag}$ ), Fermi level ( $E_{F, Ag}$ ) and the vacuum level ( $E_{Vac}$ ). The difference between  $E_{Vac}$  and  $E_{F, Ag}$  gives the work function of Ag ( $\Phi_{Ag} = -4.5$  eV). (b) Overlaying UPS spectra obtained from Ag and PSBMA/Ag substrates showed a shift in  $E_{Sec}$ .

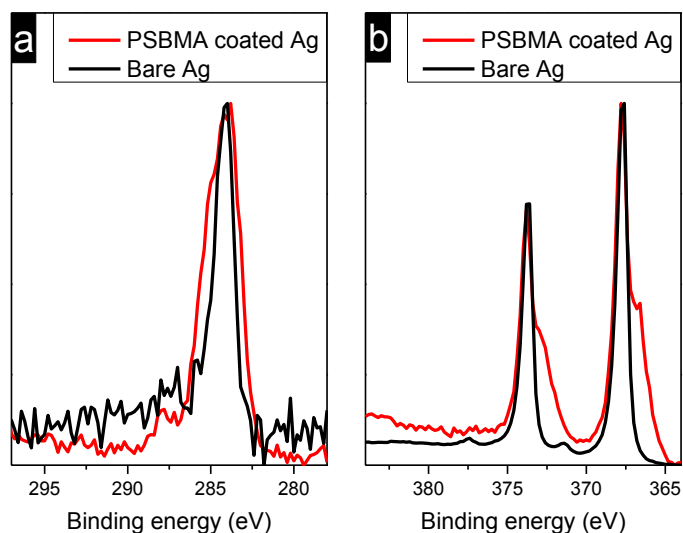


Figure 3.2 Normalized XPS spectra showing (a) C(1s) and (b) Ag(3d) signals from Ag (black) and PSBMA/Ag (red) substrate.

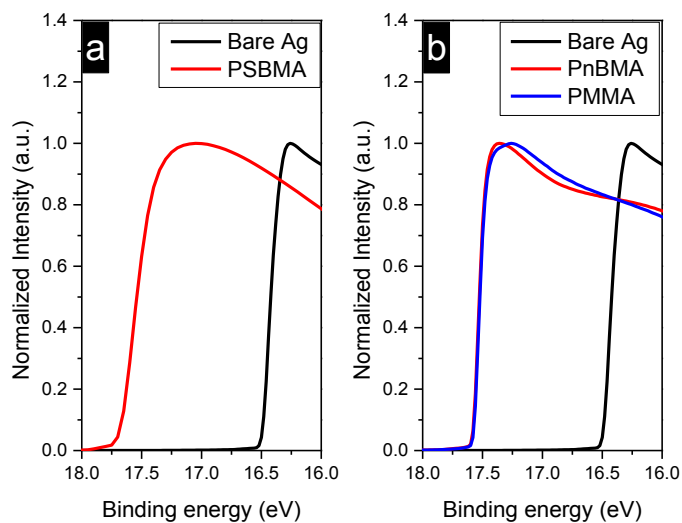


Figure 3.3 (a) UPS spectra of Ag (black) and PSBMA/Ag (red) showed  $E_{Sec}$  shifted to higher binding energy by  $\sim 1$  eV. (b) UPS spectra showing the  $E_{Sec}$  values of both PMMA/Ag and PnBMA/Ag are comparable to that of PSBMA/Ag.

The significant reduction in Ag WF provided by PSBMA implies PSBMA is a potential candidate to modify silver cathode in PSCs. However, attempts to

incorporate PSBMA as a cathode modifier only improved the PCE from 2.5 % to 3.5 % (Figure 3.4). The active layer employed in this study was prepared from a solution of PTB7/PC<sub>71</sub>BM (2:3 wt. ratio) in chlorobenzene/1,8-diiodooctane (at 100:3 vol. ratio, conc. 25 mg/mL), spin-coated at 1000 revolutions per minute (rpm) for 60 s on the PEDOT:PSS (40 nm) covered ITO substrate, followed by overnight vacuuming. Notably, active layer prepared in this way with LiF/Al as the cathode could reach PCE ~ 7.4 % and  $V_{oc}$  ~ 0.74 V.<sup>26</sup> The low  $V_{oc}$  (0.35 V) in our PSBMA modified PSCs suggests weak in-built electric field across the device, implying poor modification of cathode. In addition, the low fill factor (FF ~ 40%) suggested inefficient electron extraction and high contact resistance.

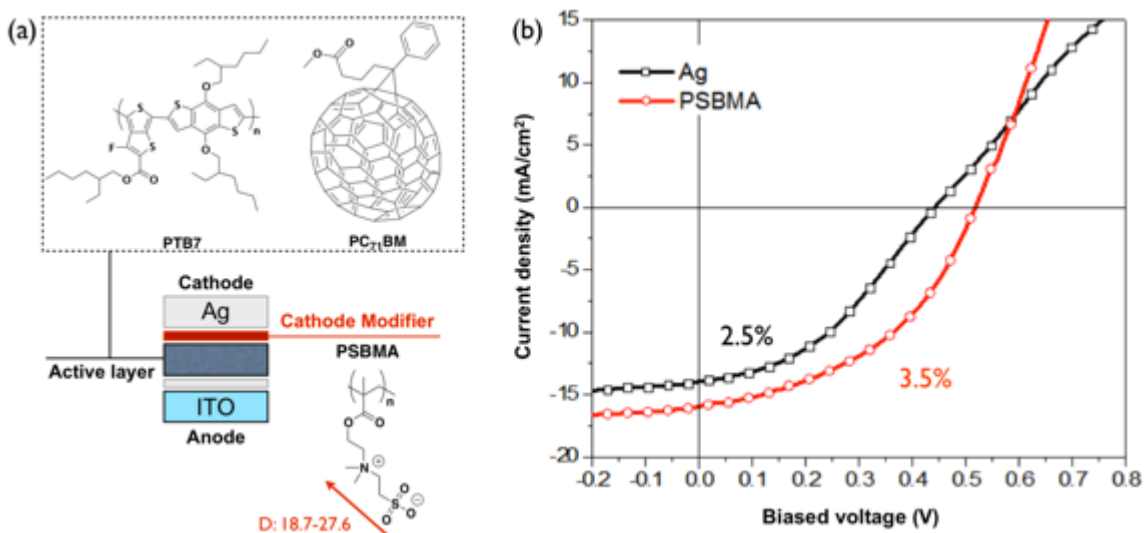


Figure 3.4 (a) Device configuration (inset: chemical structures of PTB7 (donor), PC<sub>71</sub>BM (acceptor), and PSBMA (cathode modifier)). (b) The representative IV curves of unmodified (*black*) and PSBMA-modified (*red*) PSCs.

The “squareness” of the IV curve, represented as the FF values, reflects the extraction efficiency of photogenerated carriers. In the equivalent circuit model, FF is expressed as a function of series ( $R_s$ ) and shut resistance ( $R_{sh}$ ) to describe the

energy loss due to parasite resistance. In particular,  $R_s$  is associated with the bulk and contact resistance of the active layer and electrode, while  $R_{sh}$  correlates to the current leakage from pinholes and edges of devices. The low  $R_{sh}$  values observed in our devices imply non-uniform PSBMA coating on the active layer.

Contact angle experiments using water as the probing liquid were performed to examine film quality of the PSBMA interlayer on the active layer. Typically, unmodified active layer gives a contact angle of  $80^\circ$ , and PSBMA coated silver surface shows a contact angle  $< 20^\circ$ . Surprisingly, PSBMA coated active layer has a higher water contact angle  $\sim 50^\circ$ , suggesting the presence of unmodified active layer at the top surface. Atomic force microscopy (AFM) was employed to probe film coverage at nanoscopic resolution. Height images obtained in tapping mode revealed pinholes in PSBMA coated active layer (Figure 3.9), suggesting the adhesion between PSBMA and the active layer was poor, possibly due to the mismatch of the surface energy between the hydrophilic PSBMA interlayer and the active layer.

Film stability at the active layer-cathode interface has emerged as a key to reach high device efficiencies.<sup>27</sup> At such thin film thickness required for cathode modification to prevent charge-carrier accumulation ( $< 10$  nm), a mismatch in the surface energy between the interlayer and the active layer could lead to dewetting of the interlayers. In fact, although modifiers have been reported to universally change the WF of many types of electrodes,<sup>28</sup> to the best of our knowledge, none have been shown to be applicable to all types of active layers. In particular, there were only few reports on successful cathode modifiers prepared on the P3HT/PCBM-based active layer, which has a more hydrophobic top surface than other low band gap

polymer/PCBM systems. Strategies such as incorporating new functional groups onto the backbone,<sup>20</sup> or adding small molecule surfactants<sup>27</sup> were found to be beneficial in achieving continuous coating of interlayers.

### **3.3 Azulene Copolymers: Synthesis and Cathode Modification**

The physical/chemical properties of PSBMA could be tailored by incorporating comonomers with desired functionalities in a facile one-pot radical polymerization. Copolymerizing SB-methacrylate with hydrophobic methacrylate monomers offers a versatile platform to manipulate the surface tension of PSBMA by controlling the density of the hydrophobic units along the polymer backbone. Here, we describe incorporating azulene-based methacrylate into PSBMA, yielding effective cathode modifiers for PSC applications.

Azulene, compared to conventional fused benzenoids, presents a net dipole  $> 1$  D from the resonance of cyclopentadienyl anion and tropylium cation.<sup>29</sup> Such contribution gives the molecule a dipolar nature with high polarizability and ion/metal complexation capability.<sup>30,31</sup> Moreover, the unique optical and electronic properties render them attractive for charge transport,<sup>32,33</sup> non-linear optics<sup>34,35</sup> and sensor applications.<sup>36</sup> However, up to date, synthetic methods of azulene-based polymers are limited to coupling reactions,<sup>33,37</sup> and azulene is often incorporated in the conjugated backbone as a repeat unit. Attempts to homopolymerize azulene-substituted acrylate or copolymerize it with styrene were unsuccessful.<sup>38</sup> Thus, developing a new monomer amenable to chain-growth polymerization would open a new avenue for polymeric materials with tunable azulene density.



Novel azulene containing monomers, azulene-2-yl methacrylate (1) and triazole azulene methacrylate (2) offer a robust approach to synthesize both homopolymers and copolymers with adjustable azulene density along the backbone (Figure 3.5).<sup>39</sup> Typically, azobis(isobutyronitrile) (AIBN) was used as an initiator, and anisole and freshly TFE were co-solvents employed to maintain solubility during copolymerization to ensure high monomer conversion. Incorporating monomer (1) and (2) into PSBMA, denoted as PASBs and PATSBs, yielded copolymers with favorable solubility in TFE at high azulene content of 50 mol % and > 70 mol %, respectively. In addition, SB offers orthogonal solubility, allowing their facile implementation into devices (Figure 3.5).

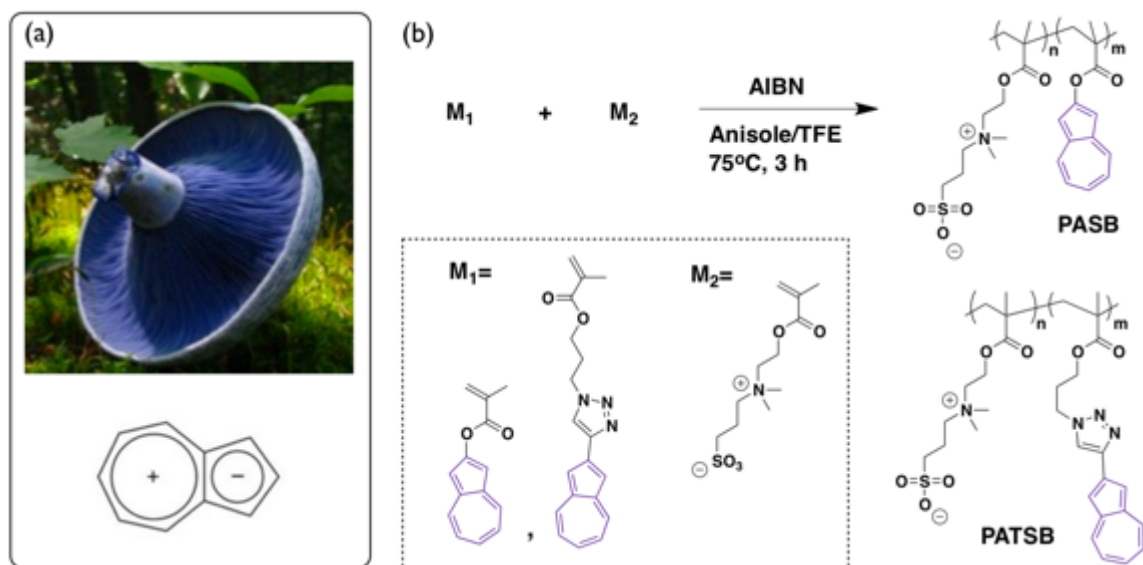


Figure 3.5 (a) Cyclopentadienyl anion and trophium cation resonance contributed to the vibrant blue color of azulene as found in *Lactarius indigo* mushrooms. (b) Synthetic routes to azulene containing sulfobetaine copolymers.

UPS spectra of PASBs and PATSBs coated Ag substrates revealed less reduction in Ag WF ( $\Delta\phi \sim 0.67 - 1.0 \text{ eV}$ ) than PSBMA coated Ag substrates

( $\Delta\phi \sim 1 \text{ eV}$ ) (Figure 3.6). Increasing the azulene composition in either PASBs or PATSBs was found to decrease  $\Delta\phi$ , indicating smaller offsets in the vacuum level with less net dipoles at the organic-Ag interface. We surmise such behavior is due to replacing SB ( $\mu \sim 24\text{D}$ )<sup>17</sup> with the azulene monomers ( $\mu \sim 5.8$  and  $4.0 \text{ D}$  for monomer 1 and 2, respectively).<sup>39</sup> In addition, the overall strength of interfacial dipole depends on the orientations of polar substituents. While studies showed the side chains of PSBMA prefer modest vertical alignment with  $\text{SO}_3$  pointing towards the metal substrate,<sup>17</sup> the orientation of azulene at the metal interface is not yet well understood. It is possible that azulene, with metal complexation capability and preferential  $\pi$ - $\pi$  stacking, presumes a face-on morphology with zero net dipole.

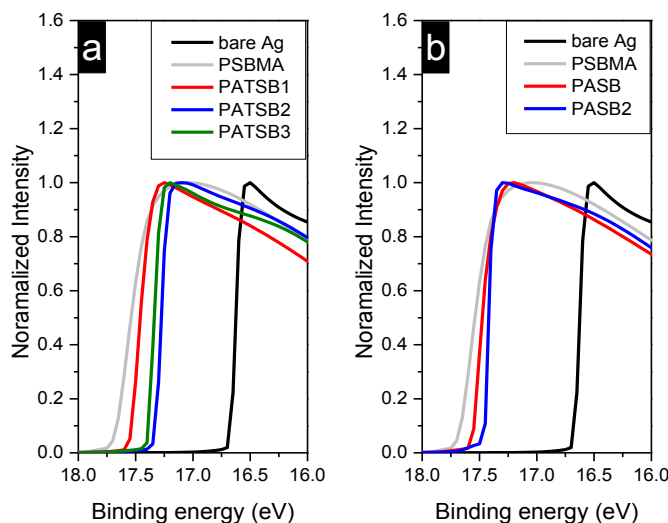


Figure 3.6 UPS spectra of (a) PATSB/Ag and (b) PASB/Ag substrates. PATSB1, PATSB2, and PATSB3 have an azulene composition of 25, 50 and 75 mol %. PASB1 and PASB2 have 25 and 50 mol % of azulene, respectively.

Although PATSBs and PASBs afforded less reduction in Ag WFs, inserting these copolymers as interlayers to modify the Ag cathode significantly improved the

PSC performance (Figure 3.7 and 3.8). Moreover, increasing the azulene density in both PATSB and PASB copolymers led to further enhancement in the PCEs of PTB7/PC<sub>71</sub>BM-based PSCs. The best PCE value of 7.8 % was achieved by using the PATSB-3 (with 75 mol % of azulene) as the cathode modifier. Such trend corresponded to the improvement observed in the film quality: increasing the azulene density led to a more uniform and continuous interlayer coverage on the PTB7/PC<sub>71</sub>BM (Figure 3.9). Notably, under the same azulene ratios (*e.g.*, 25 mol %), PASB interlayers are smoother than those of PATSB, suggesting that monomer (1) rendered the copolymer more hydrophobic than monomer (2). This explains the solubility limit of these copolymers in polar solvents such as TFE, where PASB with > 50 mol % of azulene readily precipitate in TFE, but PATSBs remained soluble even at > 70 mol % of azulene content. Such difference in hydrophobicity is reflected in the performance of PSCs— PASBs outperformed PATSBs given at the same azulene composition. This again marks the importance of designing cathode modifiers with similar surface energy to that of the active layer in order to enhance coating and adhesion of the interlayers.

### 3.4 Conclusions

PSBMA, despite containing high density of polar zwitterionic groups and inducing dramatic change in Ag WF, was a disappointing cathode modifier. The huge surface energy difference between the PSBMA film and the active layer resulted in severe dewetting of the PSBMA interlayer, and directly expose the unmodified active layer to the Ag electrode. To improve the coating quality, azulene moieties were

incorporated in PSBMA to afford PATSB and PASB copolymers. Although less WF reduction was observed in the Ag substrate modified with these copolymers, significant improvements on the device PCEs were obtained while using them as the cathode modifiers in PSCs. Examining the morphology of interlayers via AFM revealed improved film quality in PATSB and PASB interlayers upon increasing the azulene density. Such trend is in accordance to the improvement in device performance, underpinning wettability of the interlayer as a key for modifying cathode in PSC applications.

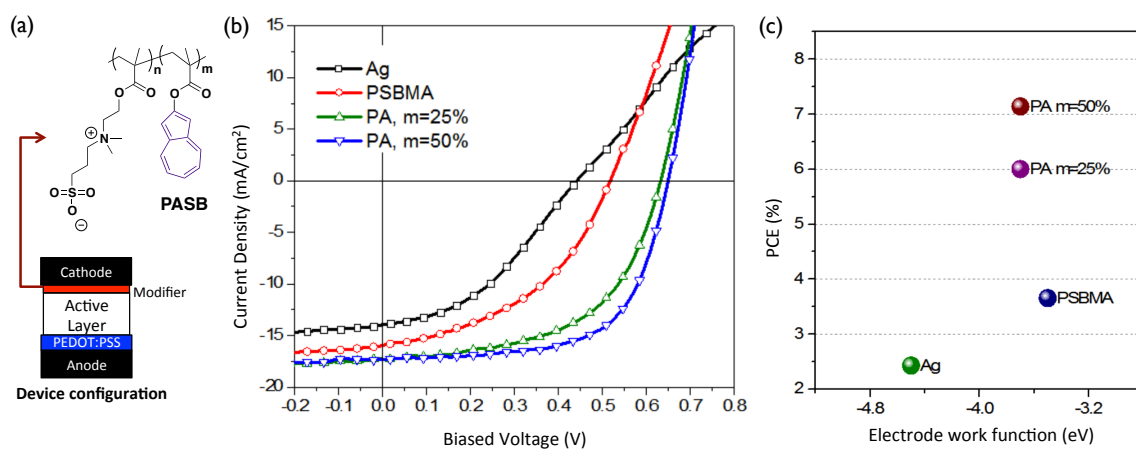


Figure 3.7 (a) Device configuration and the chemical structure of PASB (cathode modifier). (b) Representative IV curves of PASBs modified devices. (c) No obvious trend was observed between the device performance and degree of work function reduction at the cathode interface.

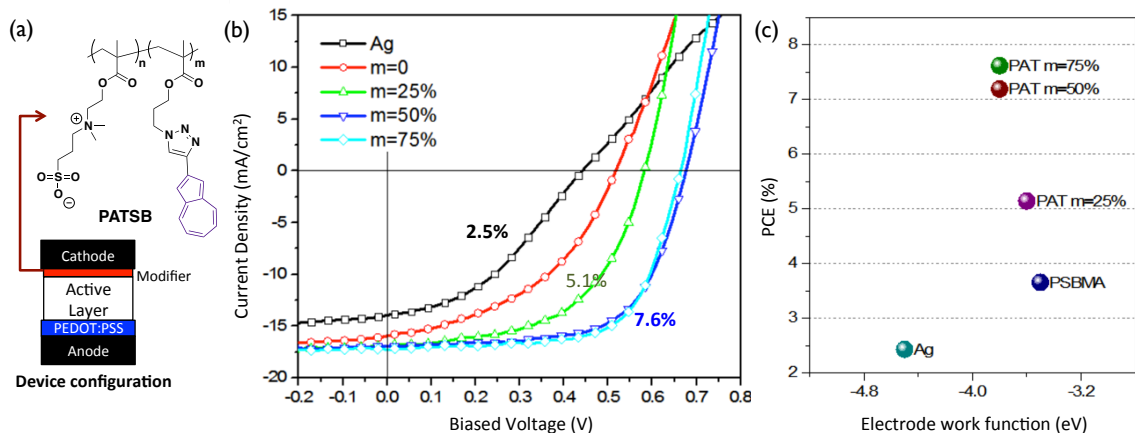


Figure 3.8 (a) Device configuration and the chemical structure of PATSB. (b) Representative IV curves of PATSBs modified solar cells. (c) Work function reduction of the electrode was found not correlate to the device efficiency.

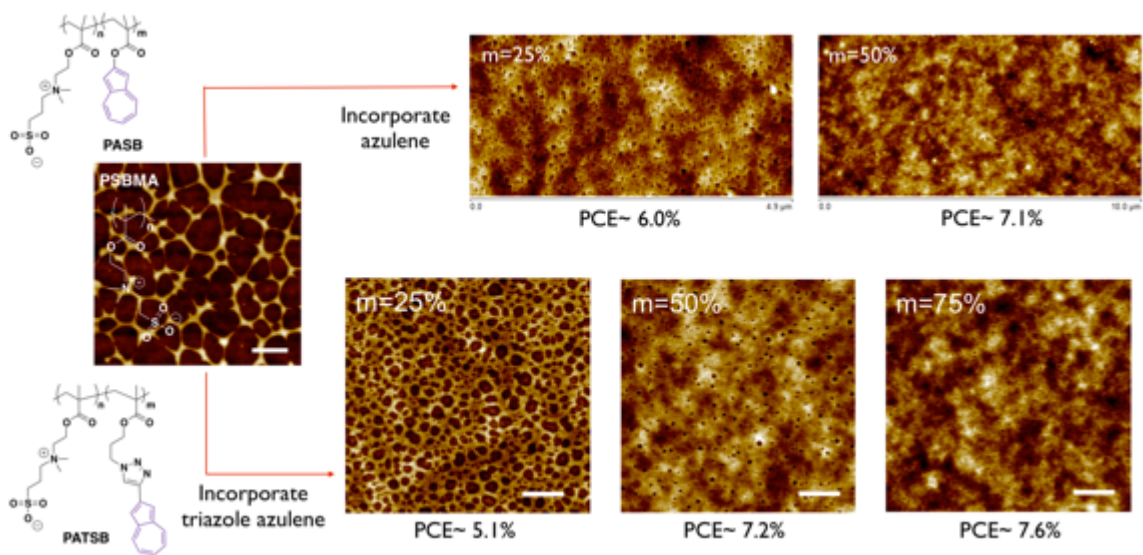


Figure 3.9 AFM height images showing the device PCEs increase with the film quality of PASBs and PATSBs interlayer. Scale bars 1  $\mu\text{m}$ .

### 3.5 References

1. Braun, S.; Salaneck, W. R.; Fahlman, M. *Adv. Mater.* **2009**, *21*, 1450– 1472.
2. Park, S. H.; Roy, A.; Beaupré, S.; Cho, S.; Coates, N.; Moon, J. S.; Moses, D.; Leclerc, M.; Lee, K.; Heeger, A. J. *Nature Photon.* **2009**, *3*, 297–302.

3. Ma, H.; Yip, H.-L.; Huang, F.; Jen, A. K. Y. *Adv. Funct. Mater.* **2010**, *20*, 1371–1388.
4. Li, G.; Zhu, R.; Yang, Y. *Nature Photon.* **2012**, *6*, 153–161.
5. Mihailetschi, V. D.; Blom, P. W. M.; Hummelen, J. C.; Rispens, M. T. *J. Appl. Phys.* **2003**, *94*, 6849.
6. Reese, M. O.; White, M. S.; Rumbles, G.; Ginley, D. S.; Shaheen, S. E. *Appl. Phys. Lett.* **2008**, *92*, 053307.
7. Hung, L. S.; Tang, C. W.; Mason, M. G. *Appl. Phys. Lett.* **1997**, *70*, 152–154.
8. Jabbour, G. E.; Kippelen, B.; Armstrong, N. R. *Appl. Phys. Lett.* **1998**, *73*, 1185–1187.
9. Krebs, F. C.; Gevorgyan, S. A.; Alstrup, J. *J. Mater. Chem.* **2009**, *19*, 5442–5451.
10. Page, Z. A.; Liu, F.; Russell, T. P.; Emrick, T. *Chem. Sci.* **2014**, *5*, 2368–2373.
11. Page, Z. A.; Duzhko, V. V.; Emrick, T. *Macromolecules* **2013**, *46*, 344–351.
12. Duan, C.; Wang, L.; Zhang, K.; Guan, X.; Huang, F. *Adv. Mater.* **2011**, *23*, 1665–1669.
13. Fang, J.; Wallikewitz, B. H.; Gao, F.; Tu, G.; Müller, C.; Pace, G.; Friend, R. H.; Huck, W. T. *J. Am. Chem. Soc.* **2011**, *133*, 683–685.
14. Kumar, A.; Pace, G.; Bakulin, A. A.; Fang, J.; Ho, P. K. H.; Huck, W. T. S.; Friend, R. H.; Greenham, N. C. *Energy Environ. Sci.* **2013**, *6*, 1589–1596.
15. Ouyang, X.; Peng, R.; Ai, L.; Zhang, X.; Ge, Z. *Nature Photon.* **2015**, *9*, 520–524.
16. Page, Z. A.; Liu, Y.; Duzhko, V. V.; Russell, T. P.; Emrick, T. *Science* **2014**, *346*, 441–444.
17. Lee, H.; Puodziukynaite, E.; Zhang, Y.; Stephenson, J. C.; Richter, L. J.; Fischer, D. A.; DeLongchamp, D. M.; Emrick, T.; Briseno, A. L. *J. Am. Chem. Soc.* **2015**, *137*, 540–549.
18. Liu, F.; Page, Z. A.; Duzhko, V. V.; Russell, T. P.; Emrick, T. *Adv. Mater.* **2013**, *25*, 6868–6873.
19. Duan, C.; Zhang, K.; Guan, X.; Zhong, C.; Xie, H.; Huang, F.; Chen, J.; Peng, J.; Cao, Y. *Chem. Sci.* **2013**, *4*, 1298–1307.
20. Oh, S.-H.; Na, S.-I.; Jo, J.; Lim, B.; Vak, D.; Kim, D.-Y. *Adv. Funct. Mater.* **2010**, *20*, 1977–1983.

21. Yeom, H. R.; Heo, J.; Kim, G.-H.; Ko, S.-J.; Song, S.; Jo, Y.; Kim, D. S.; Walker, B.; Kim, J. Y. *Phys. Chem. Chem. Phys.* **2015**, *17*, 2152–2159.
22. Krebs, F. C. *Solar Energy Materials and Solar Cells* **2009**, *93*, 465–475.
23. Yim, J. H.; Joe, S.-Y.; Pang, C.; Lee, K. M.; Jeong, H.; Park, J.-Y.; Ahn, Y. H.; de Mello, J. C.; Lee, S. *ACS Nano* **2014**, *8*, 2857–2863.
24. Seo, J. H.; Yang, R.; Brzezinski, J. Z.; Walker, B.; Bazan, G. C.; Nguyen, T.-Q. *Adv. Mater.* **2009**, *21*, 1006–1011.
25. Salaneck, W. R. *Rep. Prog. Phys.* **1999**, *54*, 1215–1249.
26. Liang, Y.; Xu, Z.; Xia, J.; Tsai, S.-T.; Wu, Y.; Li, G.; Ray, C.; Yu, L. *Adv. Mater.* **2010**, *22*, E135–E138.
27. Kang, H.; Hong, S.; Lee, J.; Lee, K. *Adv. Mater.* **2012**, *24*, 3005–3009.
28. Zhou, Y.; Fuentes-Hernandez, C.; Shim, J.; Meyer, J.; Giordano, A. J.; Li, H.; Winget, P.; Papadopoulos, T.; Cheun, H.; Kim, J.; Fenoll, M.; Dindar, A.; Haske, W.; Najafabadi, E.; Khan, T. M.; Sojoudi, H.; Barlow, S.; Graham, S.; Bredas, J. L.; Marder, S. R.; Kahn, A.; Kippelen, B. *Science* **2012**, *336*, 327–332.
29. Goldman, G. D.; Lemal, D. M. *Journal of Chemical Education*, **1988**, *65*, 923-925
30. Churchill, M. R. *Progress in Inorganic Chemistry*: Hoboken, NJ, USA, 1970; Vol. 11, pp. 53–98.
31. Zieliński, T.; Kędziołek, M. *Chem. Eur. J.* **2008**, *14*, 838–846.
32. Yamaguchi, Y.; Ogawa, K.; Nakayama, K.-I.; Ohba, Y.; Katagiri, H. *J. Am. Chem. Soc.* **2013**, *135*, 19095–19098.
33. Wang, F.; Lai, Y.-H.; Kocherginsky, N. M.; Kostecki, Y. Y. *Org. Lett.* **2003**, *7*, 995–998.
34. Liliana Cristian; Isabelle Sasaki; Pascal G Lacroix, A.; Donnadiou, B.; and, I. A.; Clays, K.; Razus, A. C. *Chem. Mater.* **2004**, 3543–3551.
35. Lacroix, P.; Malfant, I.; Iftime, G.; Razus, A.; Nakatani, K.; Delaire, J. *Chemistry* **2000**, *6*, 2599–2608.
36. Salman, H.; Abraham, Y.; Tal, S.; Meltzman, S.; Kapon, M.; Tessler, N.; Speiser, S.; Eichen, Y. *Eur. J. Org. Chem.* **2005**, *2005*, 2207–2212.
37. Murai, M.; Amir, E.; Amir, R. J.; Hawker, C. J. *Chem. Sci.* **2012**, *3*, 2721.

38. Wada, E.; Nakai, T.; Okawara, M. *Journal of Polymer Science: Polymer Chemistry Edition* **1978**, *16*, 2085–2087.
39. Puodziukynaite, E.; Wang, H.-W.; Lawrence, J.; Wise, A. J.; Russell, T. P.; Barnes, M. D.; Emrick, T. *J. Am. Chem. Soc.* **2014**, *136*, 11043–11049.



**CHAPTER 4**  
**SULFOBETAINE AND PHOSPHORYLCHOLINE ZWITTERIONIC**  
**POLYACETYLENES (ZIPAS)**

**4.1 Introduction**

Sulfobetaine (SB) based polymers now have a track record of enhancing the performance of solar cells as cathode modifiers,<sup>1,2</sup> yet, there are surprisingly few polymeric modifiers hinged on other zwitterionic functionalities. In particular, phosphorylcholine (PC), where the opposite dipole orientation, in comparison to SB, is speculated to yield completely different effect on the metal electrodes. Studies on self-assembled monolayer of small molecules on metal surfaces showed a dipole moment pointing towards (away from) the metal substrate increases (decreases) the work functions (WF) of the underlying metal substrate.<sup>3-5</sup> The net dipole alignment of polymers at interfaces, however, is much more complicated as it depends on the orientation of the polymer chains and processing history. For example, while conjugated polycations reduced WF of gold, polyanions exhibited negligible dipole effect, possibly due to the orientation of charged polymer and distribution of the corresponding counterions.<sup>6,7</sup> Polyzwitterions, without such complications, present a new exciting opportunity to study the effect of dipole orientation on the electronic properties and the cathode engineering in PSCs.

We are interested to incorporate zwitterionic functionalities onto polyacetylene backbones, affording a new class of conjugated polyzwitterions. Polyacetylenes (PAs), a classic conjugated polymer family containing simple  $-(C=C)-$

repeat units as the backbone, exhibit numerous interesting photophysical and electronic properties.<sup>8-11</sup> However, to date, there are only a few reported ionic polyacetylene. Prior examples were prepared by ring-opening metathesis polymerization of cyclooctatetrene derivatives bearing charged groups,<sup>12</sup> and by cyclopolymerization of charged and zwitterionic  $\alpha,\omega$ -bisalkynes.<sup>13,14</sup> Such substitution assists in overcoming solubility problems of conventional PAs. A particularly appealing synthetic strategy involves transition metal-mediated cyclopolymerization 1,6-heptadiynes derivatives, in which substituents are incorporated at the 4-position from the monomer on-set.<sup>15</sup> Pyridine-substituted ruthenium benzylidene metathesis catalysts are found particularly effective in these cyclopolymerizations, affording a polymer backbone composed exclusively of coplanar five-membered rings that extend conjugation length beyond that obtained with other catalytic methods.<sup>16,17</sup>

In this chapter, we describe the synthesis of zwitterionic polyacetylenes (ZIPAs) with pendant sulfobetaine (SB) and phosphorylcholine (PC) functionalities to afford charge-neutral, water soluble, electronically active materials. Such amphiphilic polymers, with hydrophobic backbone and hydrophilic side chains, display interfacial activities and self-assemble into interesting nanostructures in selective solvents. Moreover, the orthogonal solubility of SB- and PC-ZIPAs is enabling for device fabrication with state-of-the-art active layer, reaching an average PCE of 9.2 %.

## 4.2 Preparation and Characterization of ZIPAs

The novel zwitterionic 1,6-heptadiynes monomers were designed and prepared as shown in Figure 4.1 (a). Briefly, M1 was synthesized by reacting 4-hydroxymethyl-1,6-heptadiynes with ethylene chlorophosphate, followed by ring-opening with trimethylamine in anhydrous acetonitrile, affording a white solid in 94% yield. M2 was prepared by ring-opening of 1,3-propanesultone with the tertiary amine precursor, which was obtained from dimethylamine substitution of mesylated 4-hydroxymethyl-1,6-heptadiyne, giving light beige solid in 80% yield.

Polymerization of M1 and M2 was performed in tetrahydrofuran (THF)/2,2,2-trifluoroethanol (TFE) (1:1 v/v) at various monomer-to-catalyst ( $[M]/[Ru]$ ) ratios. The synthesized polymers were precipitated into acetone, and purified via dialysis against water (molecular weight cut off = 1 kDa) for 2 days. The exact monomer conversion was difficult to discern from ill-defined, overlapping NMR signals of monomers and polymers. A typical yield is estimated to be ~50-60% after lyophilization assuming a full monomer conversion.

Both ZIPAs have five-membered repeats microstructures as revealed by  $^{13}C$  NMR spectroscopy. Two well-defined carbon signals at 140.5 and 124.4 ppm from ZIPA-PC in MeOD- $d_4$  (Figure 4.1 (b)) represent the olefinic carbon peaks in the 5-membered ring-based units, whereas 6-membered ring-structures would give 4 alkene peaks. The poor solubility of ZIPA-SB in methanol and water precluded characterization in those solvents. The  $^{13}C$  NMR of ZIPA-SB conducted in TFE- $d_6$  showed the characteristic carbon resonances of the 5-membered ring at 139.6, 72.3, 41.1, and 33.5 ppm. The greater intensity of the side chain signals relative to the

backbone suggests that the zwitterionic groups are better solvated in polar solvents than the hydrophobic conjugated backbones (Figure 4.2).

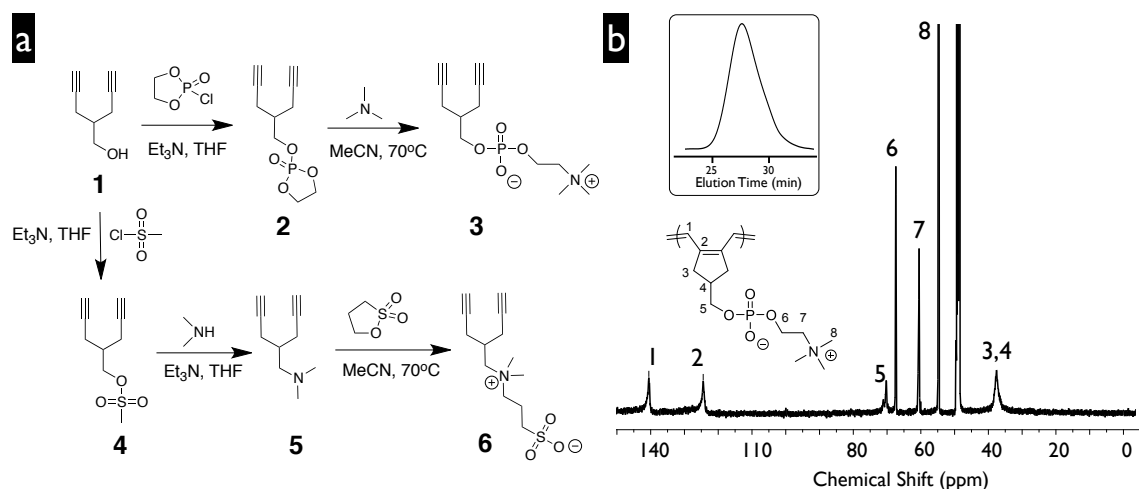


Figure 4.1 (a) Synthetic route to 1,6-heptadiyne monomers with PC (**3**) and SB (**6**) functionalities. (b) <sup>13</sup>C NMR spectra of ZIPA-PC in MeOD-*d*<sub>4</sub>. The inset shows a representative GPC trace of ZIPA-PC.

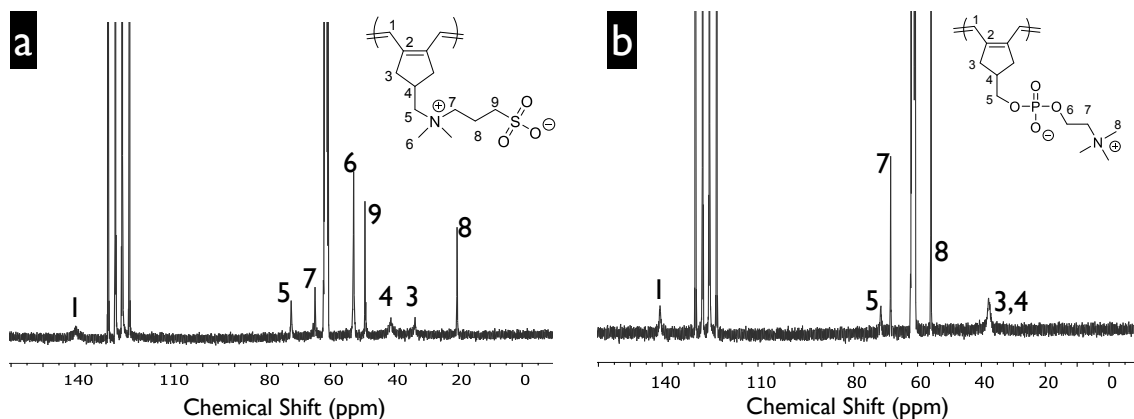


Figure 4.2 <sup>13</sup>C NMR spectra of (a) ZIPA-SB and (b) ZIPA-PC in TFE-*d*<sub>6</sub>. Peaks between 120-130 ppm and at 60 ppm are from TFE.

Molecular weights of synthesized polymers were estimated by gel permeation chromatography (GPC) in the range of ~11 to 45 kDa as summarized in Table 4.1. A monomodal distribution was observed for every synthesized polymer,

suggesting the absence of intermolecular crosslinking. The molecular weight depends on the initial monomer-to-catalyst ratio, however, the polydispersity ( $\mathcal{D} \sim 1.5$ ) is large compare to a typical living polymerization. This could be due to slow initiation, chain transfer<sup>18,19</sup> and decomposition of ruthenium carbenes in alcohol solvents under the given polymerization conditions.<sup>20,21</sup>

Table 4.1 Summary of synthesized ZIPA-PC and ZIPA-SB from M1 and M2, respectively.

Entry <sup>a</sup>	Monomer	[M]/[I]	$M_n$ (kDa) <sup>c</sup>	$\mathcal{D}^c$
1	M1	25	17.8	1.2
2	M1	50	31.0	2.0
3 <sup>b</sup>	M1	50	35.3	1.6
4	M1	100	44.8	1.8
5	M2	25	11.0	1.4
6	M2	50	18.3	1.4
7 <sup>b</sup>	M2	50	12.3	1.5
8	M2	100	26.5	1.4
9	M2	200	31.1	1.6

<sup>a</sup>Polymerization was carried out in 1:1 (v/v) THF/TFE at 0.5 M at 0 °C.

<sup>b</sup>Polymerization was carried out in 1:1 (v/v) DCM/TFE at 0.5 M with 20 mol % 3,6-dichloropyridine relative to GIII at 0 °C. <sup>c</sup>Determined by TFE gel permeation chromatography calibrated by poly(methyl methacrylate) standards.

Thermal properties of SB- and PC-ZIPAs were studied by thermal gravimetric analysis (TGA) and differential scanning calorimetry (DSC) as shown in Figure 4.3. Both polymers were found to be stable up to 240 °C with 2 distinct degradations steps: the first weight loss is associated with the alkene backbone, while the second weight loss is related to the break up of zwitterions. ZIPA-SB was found to burn almost to completion while ZIPA-PC gave residual char  $\sim 20$  wt %. No crystallization peaks were observed for both polymers, suggesting ZIPAs are amorphous, consistent with other reported poly(1,6-heptadiynes). While the  $T_g$  of ZIPA-SB was

undiscernable, ZIPA-PC exhibited a relatively high glass transition temperature ( $T_g$ ) at 95 °C, in contrast to other reported PA derivatives (*e.g.*  $T_g$  of poly(DEDPM) ~26 °C). This is presumably due to PC restricts rotation of the polymer backbone as observed in many other polymers bearing hydrophilic side chains.

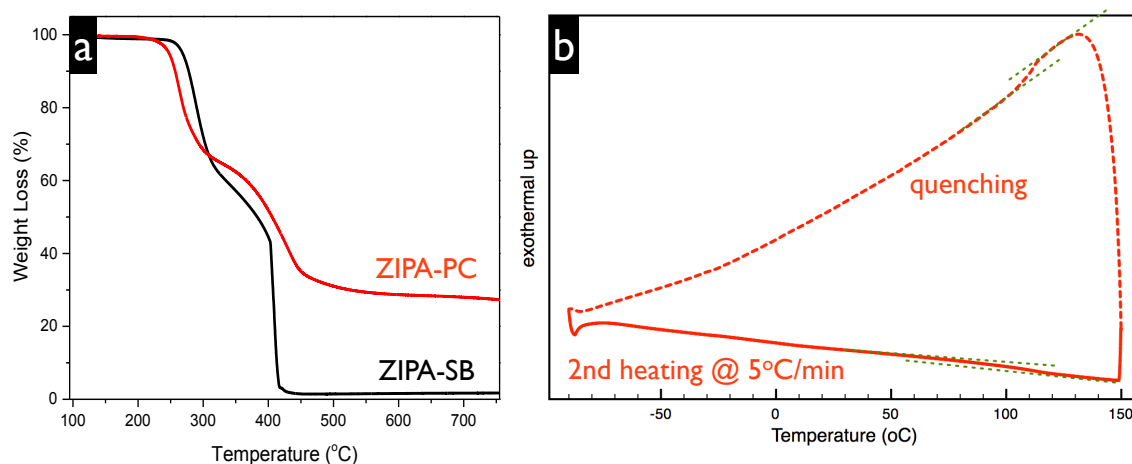


Figure 4.3 (a) TGA traces of ZIPA-SB (*black*) and ZIPA-PC (*red*) showing the polymers are thermal stable up to 240 °C. (b) DSC traces showing the  $T_g$  of ZIPA-PC is at ~ 95 °C.

### 4.3 Solution-driven Assembly of ZIPAs

ZIPA-PC displays good solubility in water and alcohols (*i.e.*, methanol, ethanol and TFE), but ZIPA-SB only dissolves in fluorinated alcohols such as TFE and hexafluoroisopropanol, with limited water solubility. Indeed, the stronger resonance signals from the SB side chain to that of the conjugated backbone in the ZIPA-SB  $^{13}\text{C}$  NMR spectra already indicated a limited solubility of the hydrophobic polymer backbone even in fluorinated solvents as TFE. Despite the presence of hydrophilic SB pendent group, we noticed ZIPA-SB gradually precipitated in deionized water during dialysis. This has been reported in other SB-substituted polymers, where strong electrostatic interactions between sulfonate and ammonium groups rendered the

polymer insoluble.<sup>22</sup> To screen such dipole-dipole interactions, salt (*e.g.*, NaCl) can be added to enhance solubility of ZIPA-SB.

Amphiphilic polymers with an appropriate hydrophobic/hydrophilic balance are particularly interesting because a wide breadth of nanostructures can be fabricated in solution by tuning the polymer solubility. Classic examples include the formation of spherical, cylindrical micelles, and bilayer structures in linear block copolymers<sup>23,24</sup> and grafted copolymers.<sup>25-28</sup> Interestingly, ZIPAs were also amenable to polymer assemblies in solution. Adding isopropanol (IPA, a poor solvent) to ZIPA-SB (1 mg/mL in TFE) led to self-assembled PA nanoribbons as confirmed by the transmission electron microscopy (TEM) and atomic force microscopy (AFM) shown in Figure 4.4 and Figure 4.5. These structures are formed shortly after adding IPA and reached a final width  $\sim 20\text{-}30$  nm and  $\sim 1$   $\mu\text{m}$  in length before precipitation. *Ex situ* TEM studies, performed on aliquots taken from ZIPA-SB solutions with increasing IPA concentrations, showed the ZIPA-SB initially formed spherical nano-objects (at 25 vol% IPA), which gradually aggregated to form nanoribbons ( $> 37.5$  vol% IPA). Such structural transition between the spherical nanoparticles and nanoribbons was reversible by alternately adding TFE and IPA into the solution of ZIPA-SB nanoribbons. This behavior resembles intermicellar fusion, where spherical micelles transform into cylindrical nano-cylinders as observed in block copolymers.<sup>29</sup> We surmise that sulfobetaine are decorating the exterior of the nanostructures, owing to its preferable interaction with TFE and IPA, while PC rendered ZIPA-PC too hydrophilic to possess self-assembly capabilities in the TFE/IPA mixtures (Figure 4.6).

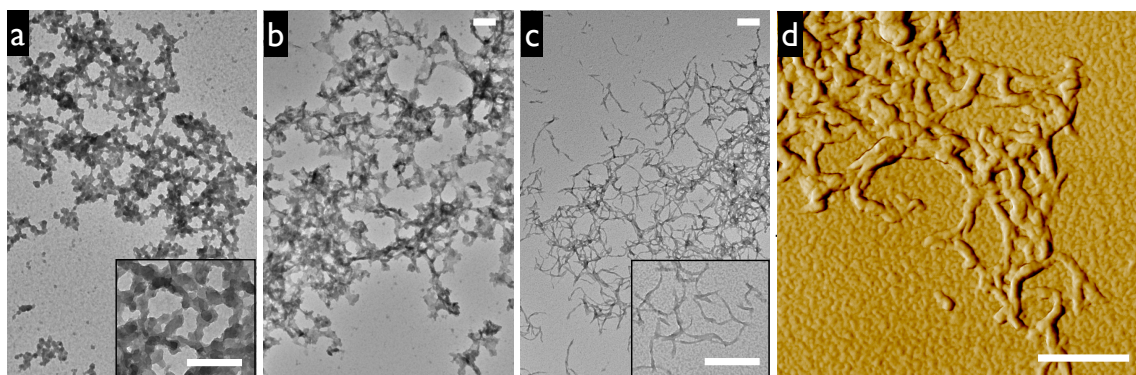


Figure 4.4 TEM images showing the evolution of ZIPA-SB nanostructures in 100  $\mu\text{L}$  of ZIPA-SB at 1 mg/mL in TFE after adding (a) 15  $\mu\text{L}$ , (b) 30  $\mu\text{L}$ , and (c) 60  $\mu\text{L}$  of IPA. (d) The corresponding AFM image of (c). Scale bars 500 nm.

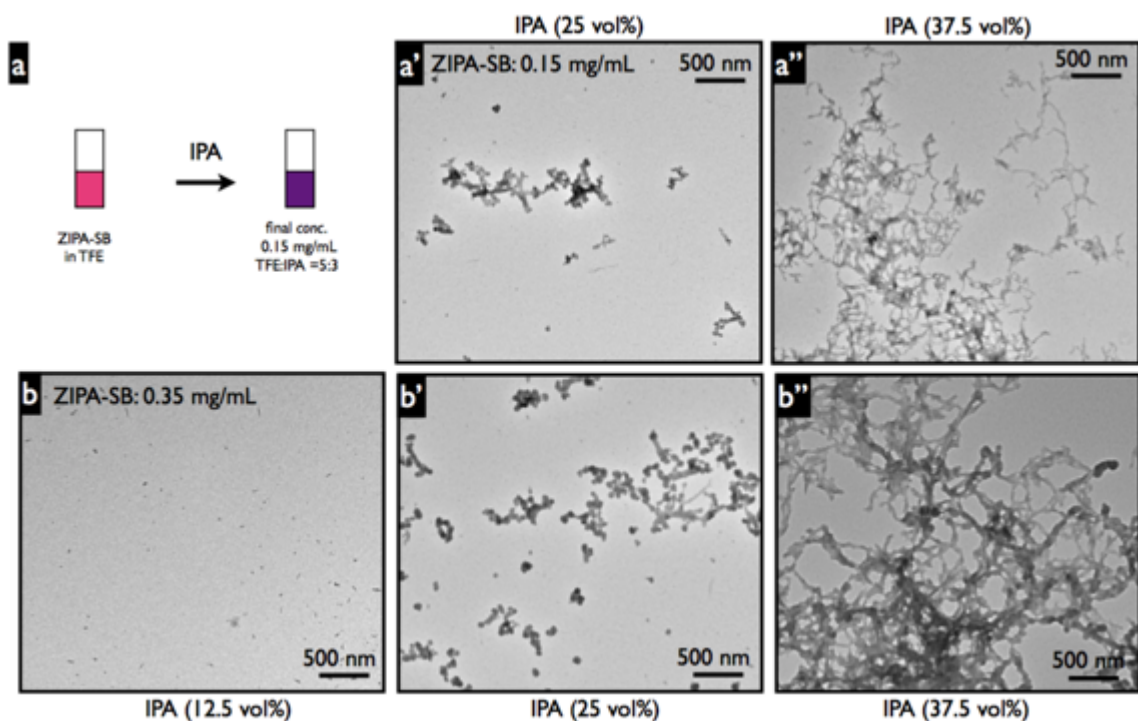


Figure 4.5 Preparation of ZIPA-SB nanofibers and representative TEM images of ZIPA-SB nanostructures at fixed final ZIPA-SB concentration (a' and a'' at 0.15 mg/mL and b series at 0.35 mg/mL) with different vol % of IPA as indicated on the images.



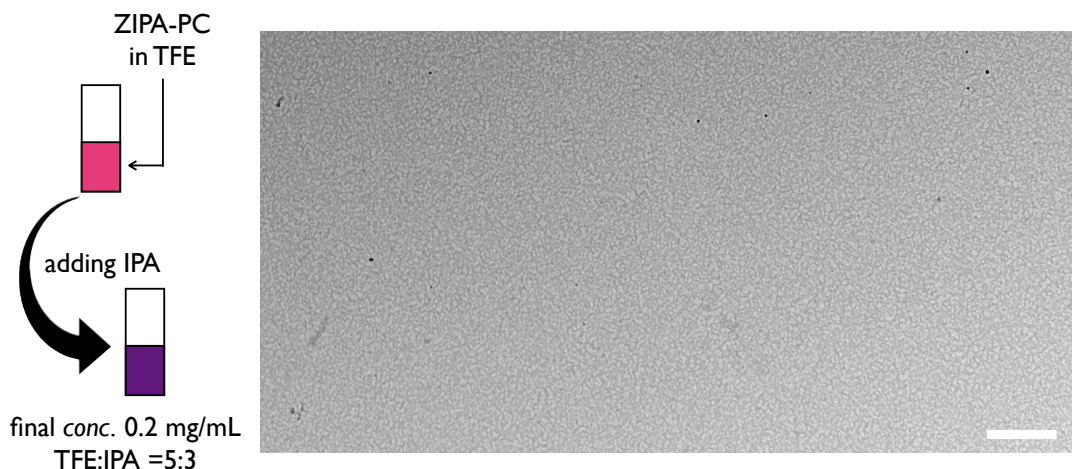


Figure 4.6 Adding IPA to ZIPA-PC solution in TFE (1 mg/mL) led to change in solution color, but no distinct features were observed by TEM from drop-casted solution samples. Scale bar 500 nm.

SB and PC ZIPAs showed similar optoelectronic properties in TFE (0.2 mg/mL) as shown in Figure 4.7 (a). Both polymers displayed distinct 0-1 ( $I_{0-1}$ ) (~525 nm) and 0-0 ( $I_{0-0}$ ) (~560 nm) vibronic transitions in TFE, characteristic absorptions of regioregular poly(1,6-heptadiene)s with exclusively five-membered ring,<sup>17,30</sup> supporting our prior <sup>13</sup>C NMR findings. The weaker  $I_{0-0}$ , in comparison to  $I_{0-1}$ , suggests distortion in the conjugated backbone with limited intra-chain couplings<sup>30</sup> in both SB and PC substituted ZIPAs. Increasing the solvent polarity red-shifts the absorption maximum, possibly due to interaction between the solvent molecules and  $S_0$  to  $S_2$  (0-0) transition dipoles in the polyenes.<sup>8</sup> Notably, the identical absorption onsets of ZIPA-SB and ZIPA-PC in TFE, corresponding to a bandgap of ~2.0 eV, match well with other conjugated poly(1,6-heptadienes),<sup>30,31</sup> suggesting the electronic properties and effective conjugation length are not affected by the pendent zwitterionics.

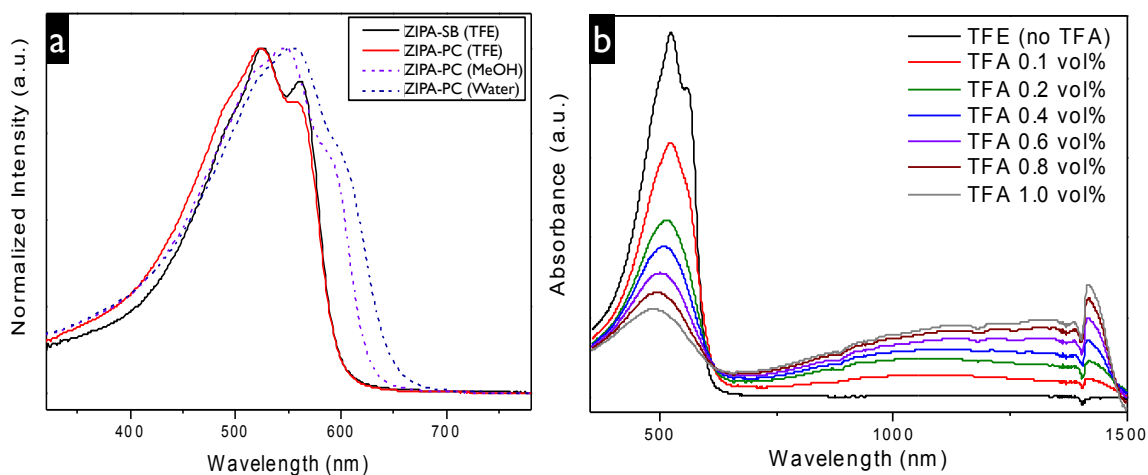


Figure 4.7 UV/Vis absorption spectra of (a) ZIPA-SB and ZIPA-PC in TFE, methanol and water. (b) The evolution of UV/Vis/IR absorption upon doping ZIPA-PC in TFE solution with TFA.

ZIPA-PC can be doped in TFE solution by adding trifluoroacetic acid (TFA), leading to a new absorption band in the IR region and the disappearance of the interband transition in the UV/Vis region (Figure 4.7 (b)). This is attributed to doping agents narrowing the bandgap, and such absorption evolution was observed in other p-doped PAs.

#### 4.4 Electronic Properties of ZIPA films at Silver Interface

Conjugated polymers often exhibit different electronic properties when confined in a thin film geometry. As a result of intermolecular interaction, the UV/Vis spectra of SB and PC ZIPA thin films showed significant red-shifted absorption, in comparison to the absorption of ZIPAs in TFE solution. The band gap of these thin films were calculated to be  $\sim 1.8$  eV (Figure 4.8 (a)).

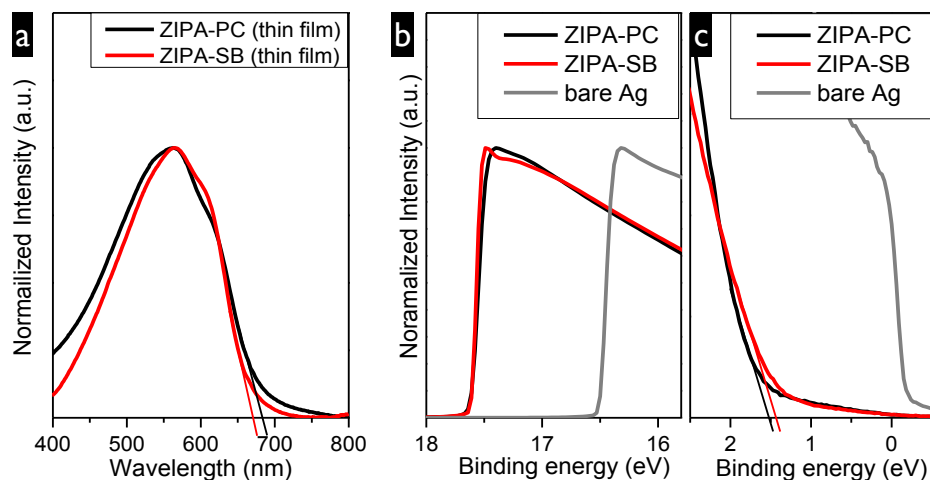


Figure 4.8 (a) UV/Vis absorption spectra of ZIPA-SB and ZIPA-PC thin films, where the tangential lines suggest identical bandgap  $\sim 1.8$  eV. Representative UPS spectra showing (b) the  $E_{\text{Sec}}$  onset, and (c) HOMO energy level of ZIPA-SB and ZIPA-PC.

The electronic characteristics of ZIPA thin films at metal interfaces were examined by ultraviolet photoelectron spectroscopy (UPS) (Figure 4.8 (b) and (c)). By probing the kinetic energy of photoelectrons in UV excited samples, the energy alignment in ZIPA-PC and ZIPA-SB at the silver (Ag) interface was calculated and summarized in Table 4.2. Specifically, a shift in the  $E_{\text{Sec}}$  between the unmodified (*grey*) and ZIPA coated silver substrates (*black and red*) indicates an offsets in the vacuum level ( $\Delta$ ) due to the polar chemical constituents in the film, leading to a change in the work function of silver ( $\Delta\phi$ ). As from the lower binding energy onsets (Figure 4.8 (c)), we can determine the Fermi level ( $E_{\text{F}}$ ) of silver (*grey*) and the highest occupied molecular orbital energy level ( $E_{\text{HOMO}}$ ) of ZIPAs (*black and red*). The energy level of lowest unoccupied molecular orbital ( $E_{\text{LUMO}}$ ) can be estimated from  $E_{\text{HOMO}}$  and the optical band gap ( $E_{\text{g}}$ ) measured from the lower energy onset of UV/Vis spectra (Equation 4.2).

$$E_{\text{vac}} = E_{\text{sec}} - 21.2 \text{ eV} \quad (\text{Equation 4.1})$$

$$E_{\text{LUMO}} = E_{\text{g}} - E_{\text{HOMO}} \quad (\text{Equation 4.2})$$

Table 4.2 Summary of electronic energy levels of ZIPAs at Ag interfaces. (Unit, eV)

Substrate	ZIPA	$E_{\text{g}}$	HOMO	LUMO	$\Delta\Phi$
Ag	ZIPA-SB	1.85	4.8	2.99	1.1
Ag	ZIPA-PC	1.82	4.9	3.08	1.1

Despite the opposite dipole orientation in the zwitterionic moieties of the two polymers, each significantly lowered the Ag WF by  $\sim 1.1$  eV. Notably, we found PC and SB each contributes to such significant change in WF as replacing ZIPAs with phenyl-substituted poly(1,6-heptadiynes) (P-PAs) gave a modest Ag WF reduction ( $\sim 0.5$  eV) (Figure 4.9). Such operation of ZIPA-SB is similar to other SB-functionalized materials.<sup>12,14,38</sup> Although the reduction of work function by ZIPA-PC can be rationalized by assuming the polymer backbones are in more intimate contact with the metal surface with the PC side chains pointing away. However, such opposite orientation for SB- and PC-functionalized materials is not clear. Indeed, the net dipole alignment at the metal-organic interfaces depends on the film preparation, and the self-assembly of polymers, which unfortunately, remains poorly understood.

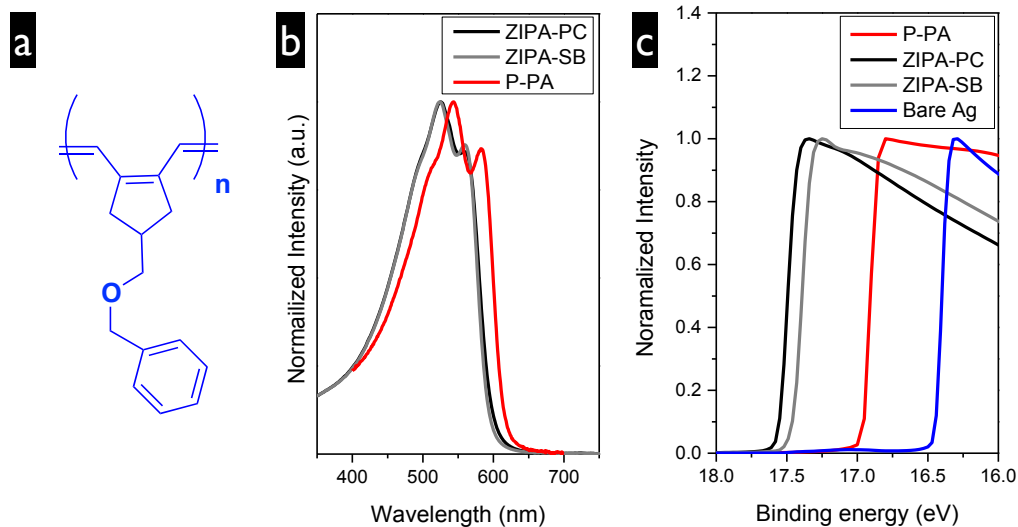


Figure 4.9 (a) The mono-substituted phenyl poly(1,6-heptadiyne) (P-PA). (b) UV/Vis spectra of P-PA (red) in comparison to ZIPAs (black and grey). (c) UPS spectra showing the  $E_{\text{Sec}}$  of Ag (blue), P-PA/Ag (red), and ZIPA/Ag (grey and black).

The average bond orientation on the air surface of ultra-thin ZIPA films ( $\sim 6$  nm) that were deposited onto Ag substrate was probed by Near-edge X-ray absorption fine structure (NEXAFS) spectroscopy. A partial electron yield (PEY) collection mode was used to provide a surface-weighted signal. Spectra were collected across the carbon K-edge at several incident angles, as shown in Figure 4.10. For ZIPA-SB coated Ag, the intensity of the  $1s \rightarrow \pi^*$  resonance at  $\approx 284.5$  eV increases at shallow incident angles where the electric field vector approaches orthogonal to the substrate plane. This result indicates a weak preference for the  $1s \rightarrow \pi^*$  transition to be oriented orthogonal to the substrate plane. Because an acetylene moiety has two  $1s \rightarrow \pi^*$  transitions that are orthogonal to each other and orthogonal to the chain axis, this orientation preference indicates that the chain axis is (mildly) preferentially parallel to the substrate plane for this material. In contrast, ZIPA-PC showed little intensity variation with incident angle (Figure 4.10 (b)),

suggesting an isotropic or tilted orientation of the conjugated backbone. Both ZIPAs exhibit very weak angular dichroism across the  $1s \rightarrow \sigma^*$  region from  $\approx 290$  eV to  $\approx 315$  eV, which is a signature of side chains. The highest intensity was observed at higher incident angles, consistent with a mild C-C skeleton alignment parallel to the substrate. This trend is also more consistent for ZIPA-SB. Studying thinner ZIPA films, which would allow probing the orientation of backbones and side chains at the Ag interface directly, was inconclusive as achieving uniform coating of ZIPAs at  $< 5$  nm on silver was difficult.

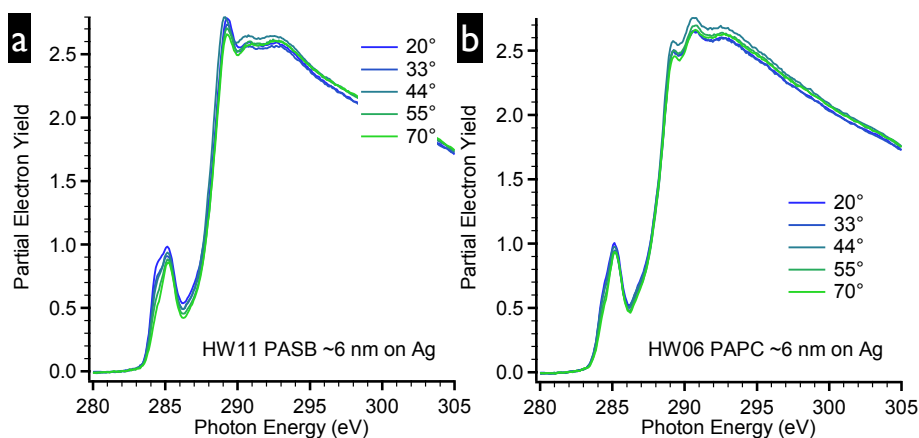


Figure 4.10 The NEXAFS spectra of (a) ZIPA-SB and (b) ZIPA-PC film ( $\sim 5$  nm) on Ag.

#### 4.5 ZIPAs as Cathode Modifiers in PSCs

We were initially surprised to find that solar cells fabricated with ZIPA-SB or ZIPA-PC modified silver cathodes exhibited devices with poor performance. (*i.e.*, power conversion efficiency (PCE  $\sim 2.45\%$ ) (Table 4.4) Inspection of as-spun ZIPAs on active layers by AFM showed evidence of dewetting, attributed to the surface energy mismatch between the hydrophilic ZIPAs and the hydrophobic active layer ([2,6'-4,8-di(5-ethylhexylthienyl)benzo[1,2-*b*;3,3-*b'*]dithiophene) [3-fluoro-2[(2-

ethylhexyl)carbonyl] thieno[3,4-*b*]thiophenediyl]] (PTB7-Th)/[6,6]-phenyl-C<sub>71</sub>-butyric acid methyl ester (PC<sub>71</sub>BM)). ZIPA-SB was especially prone to pinhole formations with large surface roughness (Figure 4.11). Poor film coverage of the interlayer, exposing the active layer to the evaporated cathode leads to low  $V_{oc}$ , FF and, thus, the poor PCE<sup>32</sup> (the black and blue points in Figure 4.12). Fortunately, uniform ZIPA coatings could be achieved on active layers washed with 2-methoxy ethanol (EGME). In a typical device fabrication, the active layer was spin-coated, vacuum dried for 20 min, and prior to the deposition of ZIPA and cathode evaporation, spin-coated with EGME. Such process significantly increased the surface energy of the active layer as evidenced by contact angle measurements using TFE as the probing liquid. EGME, with a slight PC<sub>71</sub>BM solubility, removed some PC<sub>71</sub>BM from the top surface upon washing (Table 4.3), enabling better interlayer coating and adhesion (Figure 4.11). Deposition of a ZIPA-PC or ZIPA-SB layer on EGME washed active layer resulted in devices outperforming the reference cells, reaching an average PCE of ~ 9.2 and 7.9 %, respectively (Table 4.4). The slightly lower performance of the ZIPA-SB interlayer is attributed to its poorer inherent wettability on the active layer.

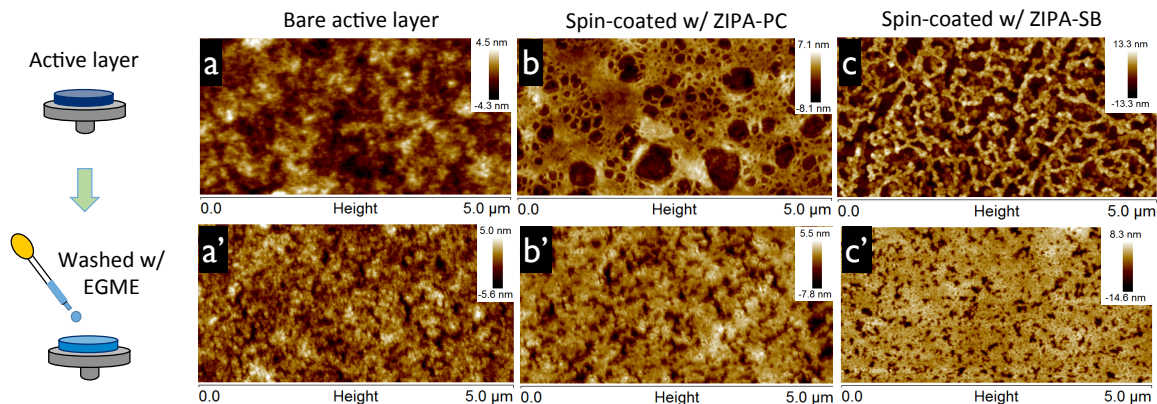


Figure 4.11 AFM height images of active layer (a) before and (a') after EGME washing. (b) and (c) show the surface of ZIPA-PC and ZIPA-SB coated on active layer, respectively. (b') and (c') are ZIPA-PC and ZIPA-SB coated on EGME washed active layer, respectively.

Table 4.3 XPS atomic analysis of the active layer surfaces before and after EGME washing.

XPS <sup>a</sup>	C	S	F
No washing	94.7	4.6	0.7
After washing	91.4	7.1	1.6

<sup>a</sup>Take off angle was 45°

The major enhancement in device efficiency resulted from the  $V_{oc}$  (over 55%) as would be expected from the UPS studies. The reduction in work function of the Ag cathode generates a strong built-in potential gradient across the solar cell, leading to an improved  $V_{oc}$  as well as a higher  $J_{sc}$  and FF, possibly as a result of increased charge extraction efficiency. As the thickness of the polyene film deviates from optimal  $\sim 5$  nm, the solar cell performance deteriorated. While thinner films are less effective in reaching higher  $V_{oc}$ 's, thick interlayers develop S-shape in the IV-curves (Figure 4.13) with decreased FFs and PCEs. Such lowered performance upon increasing film thickness is rationalized by the energy level alignment in the solar cell. The LUMOs



of ZIPA-SB and ZIPA-PC, calculated to be  $\sim 3.0$  eV for both (Table 4.2), are higher than that of PC<sub>71</sub>BM, implying a higher potential barrier for electron collection. This would result in charge accumulation at the active layer/interlayer interface as the interlayer thickness increases.

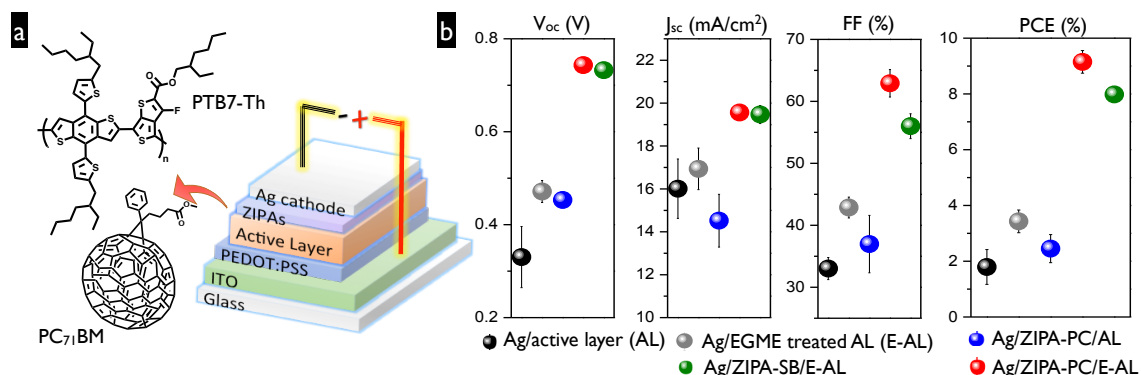


Figure 4.12 (a) The solar cell configuration, and the chemical structure of PTB7-Th (donor) and PC<sub>71</sub>BM (acceptor) (b) The device performances (averaged over 6 devices) with and without ZIPA interlayers.

Table 4.4 Summary of device performances.

Cathode	EGME	V <sub>oc</sub> (V)	J <sub>sc</sub> (mA/cm <sup>2</sup> )	FF (%)	PCE (%)
Ag	no	0.33 (±0.07)	16.0(±1.4)	33.0 (±1.8)	1.79 (±0.62)
Ag	yes	0.47 (±0.02)	16.9 (±1.0)	42.9 (±1.7)	3.43 (±0.41)
Ag/ZIPA-PC (5 nm)	no	0.45 (±0.01)	14.2 (±1.2)	37.0 (±4.6)	2.45 (±0.50)
Ag/ZIPA-SB (5 nm)	yes	0.73 (±0.01)	19.5 (±0.4)	56.0 (±2.0)	7.98 (±0.20)
Ag/ZIPA-PC (5nm)	yes	0.74 (±0.01)	19.5 (±0.1)	62.9 (±2.2)	9.15 (±0.41)

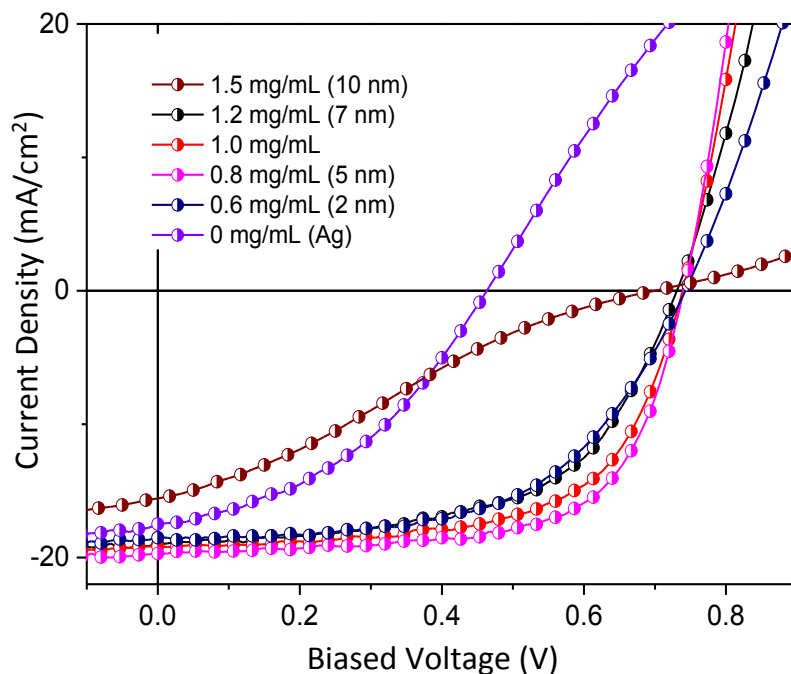


Figure 4.13 The representative IV curves of PSCs with varied ZIPA-PC thickness at the active layer-Ag cathode interface. The optimal thickness at  $\sim 5$  nm gave ZIPA-PC modified solar cells an average performance of 9.2 %.

#### 4.6 Conclusions

SB and PC ZIPAs were prepared by ruthenium catalyzed metathesis cyclopolymerization. This synthesis incorporates of zwitterionic functionality from monomer at the monomer stage and leads exclusively to five-membered ring microstructures. PC renders the polyacetylene product water soluble, while SB functionalized ZIPA displayed salt-responsive solubility. The dipole provided by these zwitterionic moieties proves useful for reducing metal work functions to modify cathodes, allowing for substantial enhancement in PCE. Upon integrating these novel materials into bulk-heterojunction solar cells as electrode interlayers, power conversion efficiencies up to 9.2% were achieved.

## 4.7 References

1. Page, Z. A.; Liu, Y.; Duzhko, V. V.; Russell, T. P.; Emrick, T. *Science* **2014**, *346*, 441–444.
2. Ouyang, X.; Peng, R.; Ai, L.; Zhang, X.; Ge, Z. *Nature Photon.* **2015**, *9*, 520– 524.
3. Campbell, I.; Rubin, S.; Zawodzinski, T.; Kress, J.; Martin, R.; Smith, D.; Barashkov, N.; Ferraris, J. *Phys. Rev. B, Condens. Matter* **1996**, *54*, R14321–R14324.
4. Xavier Crispin; Victor Geskin; Annica Crispin; Jérôme Cornil; Roberto Lazzaroni; William R Salaneck, A.; Jean-Luc Brédas. *J. Am. Chem. Soc.* **2002**, *124*, 8131–8141.
5. Husein, T. A.; Schuster, S.; Egger, D. A. *Adv. Funct. Mater.* **2015**, *25*, 3943–3957.
6. Seo, J. H.; Yang, R.; Brzezinski, J. Z.; Walker, B.; Bazan, G. C.; Nguyen, T.-Q. *Adv. Mater.* **2009**, *21*, 1006–1011.
7. Seo, J. H.; Nguyen, T.-Q. *J. Am. Chem. Soc.* **2008**, *130*, 10042–10043.
8. Christensen, R. L.; Galinato, M. G. I.; Chu, E. F.; Howard, J. N.; Broene, R. D.; Frank, H. A. *J. Phys. Chem. A* **2008**, *112*, 12629–12636.
9. Craig, N. C.; Demaison, J.; Groner, P.; Rudolph, H. D.; Vogt, N. *J. Phys. Chem. A* **2015**, *119*, 195–204.
10. Christensen, R. L.; Faksh, A.; Meyers, J. A.; Samuel, I. D. W.; Wood, P.; Schrock, R. R.; Hultsch, K. C. *J. Phys. Chem. A* **2004**, *108*, 8229–8236.
11. Czekelius, C.; Hafer, J.; Tonzetich, Z. J.; Schrock, R. R.; Christensen, R. L.; Müller, P. *J. Am. Chem. Soc.* **2006**, *128*, 16664–16675.
12. Langsdorf, B. L.; Zhou, X.; Adler, D. H.; Lonergan, M. C. *Macromolecules* **1999**, *32*, 2796–2798.
13. Vygodskii, Y. S.; Shaplov, A. S.; Lozinskaya, E. I.; Vlasov, P. S.; Malyshkina, I. A.; Gavrilova, N. D.; Santhosh Kumar, P.; Buchmeiser, M. R. *Macromolecules* **2008**, *41*, 1919–1928.
14. Choi, D. C.; Kim, S. H.; Lee, J. H.; Cho, H. N.; Choi, S. K. *Macromolecules* **1997**, *30*, 176–181.
15. Sung-Hyun Kim; Yun-Hi Kim; Hyun-Nam Cho; Soon-Ki Kwon; Hwan-Kyu Kim, A.; Sam-Kwon Choi. *Macromolecules* **1996**, *29*, 5422–5426.

16. Kumar, P. S.; Wurst, K.; Buchmeiser, M. R. *J. Am. Chem. Soc.* **2008**, *131*, 387–395.
17. Kang, E.-H.; Lee, I. S.; Choi, T.-L. *J. Am. Chem. Soc.* **2011**, *133*, 11904–11907.
18. Bielawski, C. W.; Grubbs, R. H. *Progress in Polymer Science* **2007**, *32*, 1–29.
19. Choi, T. L.; Grubbs, R. H. *Angew. Chem. Int. Ed.* **2003**, *42*, 1743–1746.
20. Trnka, T. M.; Morgan, J. P.; Sanford, M. S.; Wilhelm, T. E.; Scholl, M.; Choi, T. L.; Ding, S.; Day, M. W.; Grubbs, R. H. *J. Am. Chem. Soc.* **2003**, *125*, 2546–2558.
21. Kang, E.-H.; Yu, S. Y.; Lee, I. S.; Park, S. E.; Choi, T.-L. *J. Am. Chem. Soc.* **2014**, *136*, 10508–10514.
22. Page, Z. A.; Duzhko, V. V.; Emrick, T. *Macromolecules* **2013**, *46*, 344–351.
23. Förster, S.; Antonietti, M. *Adv. Mater.* **1998**, *10*, 195–217.
24. Zhang, M.; Drechsler, M.; Müller, A. H. E. *Chem. Mater.* **2004**, *16*, 537–543.
25. Breitenkamp, K.; Emrick, T. *J. Am. Chem. Soc.* **2003**, *125*, 12070–12071.
26. Wang, C.; Li, G.; Guo, R. *Chem. Commun.* **2005**, 3591–3593.
27. Kratz, K.; Breitenkamp, K.; Hule, R.; Pochan, D. *Macromolecules* **2009**, *42*, 3227–3229.
28. Qiu, X.-Y.; Jiang, M.-W.; Guo, C.-G.; He, Y.-J.; Wang, C.-Q. *Carbohydrate Polymers* **2012**, *87*, 2306–2312.
29. Koh, H.-D.; Park, S.; Russell, T. P. *ACS Nano* **2010**, *4*, 1124–1130.
30. Kang, E.-H.; Choi, T.-L. *ACS Macro Lett.* **2013**, *2*, 780–784.
31. Kang, E.-H.; Lee, I.-H.; Choi, T.-L. *ACS Macro Lett.* **2012**, *1*, 1098–1102.
32. Chang, Y.-M.; Zhu, R.; Richard, E.; Chen, C.-C.; Li, G.; Yang, Y. *Adv. Funct. Mater.* **2012**, *22*, 3284–3289.

## CHAPTER 5

### SUMMARY AND OUTLOOK

In chapter 2, the solution-driven assembly of a low band gap polymer (PCDTBT) into nanofibers was investigated. These suspended nanofibers were formed from packing of smaller crystallite units, giving valuable insight into the ordering of conjugated polymers in solution-processed thin films, such as in ternary PSCs.<sup>1</sup> This study showed the packing and the morphology of conjugated polymers in solution can be controlled by the solvent quality. Such method offers new opportunities for low cost and large area device fabrication.

In chapter 3 and 4, the interfacial properties of novel polyzwitterions were investigated. These materials were applied as interlayers to modify the work function of silver (Ag) cathode. Uniform interlayer coating was crucial to obtain high performance devices. Increasing the hydrophobicity of the interlayer (Chapter 3), or decreasing the surface energy of the active layer (Chapter 4) led to smooth interlayers resulting in increased device efficiency. Notably, improving the interlayer film quality on the active layer also increases device lifetime (Appendix A. 1).

Sulfobetaine (SB)- and phosphorylcholine (PC)-based zwitterionic poly(acetylene)s (ZIPAs) were found to significantly reduce the work function of Ag. This finding suggests that the net dipole moment of both SB- and PC-ZIPA is pointing away from the metal surface, despite the opposite charge orientation in the SB and PC zwitterions. Compared to SB-ZIPA, PC-ZIPA exhibited better coating on the active layer and displayed higher solubility in a range of polar solvents, rendering PC a

promising functional group for cathode modification. Detailed understanding of the mechanism behind the work function reduction afforded by the PC pendent groups, and comparative studies of other PC-polymers as electrode modifiers should lead to more high performance cathode modifiers.

A general approach to tune the work function of electrode by using conventional polymers suitable for mass production, or specialty polymers with low oxygen and water permeability, may prove useful in fabricating devices at industrial level. An exciting opportunity involves adding conductive polar nanoparticles to such commercially available polymers. In these hybrid electrode modifiers, the nanoparticles modify the work function, as well as prevent the thin film from dewetting. Preliminary results showed that both SB and PC functionalized gold nanoparticles are effective cathode modifiers (see Appendix A.2-6). The combination of zwitterionic surface ligands and the inherent functionalities of the nanoparticles (*e.g.*, surface plasmon, non-bleaching fluorescence) can open pathways for multi-mode energy harvesting devices.

1. Gu, Y.; Wang, C.; Liu, F.; Chen, J.; Dyck, O. E.; Duscher, G.; Russell, T. P. *Energy Environ. Sci.* **2014**, *7*, 3782–3790.

## CHAPTER 6

### EXPERIMENTAL PROCEDURES

#### 6.1 Preparation of PCDTBT Nanofibers

PCDTBT was dissolved in chloroform ( $\text{CHCl}_3$ ) at a concentration of 1mg/mL, then filtered through a 0.45  $\mu\text{m}$  syringe filter. This stock solution (0.5 mL) was transferred to a brass tube and the solvent was evaporated; dichloromethane (DCM), a marginal solvent was then added to give a final polymer concentration of 1 mg/mL. The solution was degassed and sealed under nitrogen (using Teflon tape at joints). It was then heated in an oven to 110°C for 2 h, after which the oven was turned off and the vessel was allowed to cool to room temperature at a rate of 20 °C/min, the solution was aged in dark for one day giving a dark purple solution. The brass metal tube, purchased from Home Depot, is assembled from Female Pipe Elbow (IFA-700) with 1/8 inch FIP and Brass Pipe Plug (LFA-710) with 1/8 inch MIP.

As the temperature used in the procedure (110°C) is well above the boiling point of DCM, secure sealing of the vessel is highly recommended. We found that a brass plug, as described above, with a Teflon tape seal was viable for these purposes. Heating performed in either an oil bath or oven allowed the experiments to be repeatedly performed without incident in our laboratories.



Figure 6.1 The metal vessel used in preparing the PCDTBT nanofibers

## 6.2 Solar Cell Fabrication Procedures

### 6.2.1 PSCs with azulene copolymers as the cathode interlayer

Solar Cell Fabrication and Measurements. Indium tin oxide (ITO) coated glass substrates ( $20 \pm 2$  ohms/sq) (Thin Film Devices, Inc.) were sonicated in detergent (Mucasol®, Sigma Aldrich), DI-water, acetone, isopropanol and dried in an oven before use. PEDOT:PSS (Clevios P VP AI 4083) was spin-coated on UV-Ozone treated ITO at 3500 rpm for 30 min (~35 nm film) and annealed at 150°C for 30 min in air. PTB7 (10 mg, from 1-Material, Inc.) and PC71BM (15 mg, Nano-C, Inc) were dissolved in 1 mL of o-dichlorobenzene with 30  $\mu$ L of diiodooctane as the additive. The solution was spin-coated on top of PEDOT:PSS at 1000 rpm for 60 s, then dried under vacuum ( $10^{-6}$  Torr) overnight. The interlayer was subsequently applied by spin coating from 0.6 mg/mL (0.4 mg/mL for PATSB-3) TFE solution at 4000 rpm for 40 s. Silver was evaporated under  $6 \times 10^{-7}$  Torr at 0.3 Å/s for the first 10 nm, followed by 0.5-1 Å/s until 100 nm thickness was reached.



### **6.2.2 Devices with ZIPA as the cathode interlayer**

ITO-coated glass was purchased from Thin Film Devices (145 nm, 20 ohms/sq.). A typical cleaning procedure involves ultrasonically cleaning with detergent, deionized (DI) water, acetone, and 2-propanol. The substrates are left in the oven to dry overnight and UV-ozoned (UVO) for 20 min prior to spin-coating of PEDOT:PSS (Celvios™) at 3.5 krpm. The substrates were dried in air at 150 °C before transferring to glove box to deposit the active layer. The active layer solution was prepared from PTB7-TH (1-Material, Inc.) and PC<sub>71</sub>BM (Nano-C, Inc.) at a 35:65 weight ratio, 25 mg/mL, in chlorobenzene/diiodooctane (DIO) (3 vol%) and stirred overnight at 55°C before use. The active layer was spin-coated at 1 krpm, 60 s and dried in vacuum 15 min to remove excess DIO before pretreating the surface by spin-coating of 2-methoxyethyl ethanol (EGME, Sigma Aldrich, anhydrous) at 4 krpm. ZIPAs in TFE were directly spin-coated onto the active layer at 4 krpm and dried under vacuum (10<sup>-6</sup>Torr) overnight, followed by deposition of cathode (Ag, 100 nm at 0.2-2 Å/s). The rate and total thickness were monitored with a quartz crystal microbalance (QCM).

### **6.3 Measuring Power Conversion Efficiency of Solar Cells**

The solar cell device was measured under simulated AM1.5G irradiation (100 mW/cm<sup>2</sup>) using Newport 91160 300-W Solar Simulator (Xe lamp). An AM1.5G filter was used and the light intensity was calibrated with an NREL-calibrated Si solar cell equipped with a KG-5 filter. The light exposure area (3.025 mm<sup>2</sup>) of the devices was defined by using a photomask with an aperture.

## **6.4 Instrumentation**

### **6.4.1 Polymer molecular weight determination**

The molecular weight of PCDTBT was determined by high temperature gel permeation chromatography (GPC) (Polymer Laboratories PL-220) with a refractive index detector. Experiments were performed at 135°C using 1,2,4-trichlorobenzene (Aldrich) as solvent, and results were based on calibration with polystyrene standards.

Zwitterionic polymers were characterized by GPC in 2,2,2-trifluoroethanol (TFE) with 0.02 M sodium trifluoroacetate at 40 °C on a Agilent 1260 infinity system with a refractive index detector, a isocratic pump, equipped with a 50 mm x 8 mm PSS PFG guard column, three 300 mm x 7.5 mm PSS PFG analytical linear M columns with a 7 µm particle size (Polymer Standards Service). The GPC was calibrated with poly(methyl methacrylate) standards.

### **6.4.2 Thermal analysis**

Thermal gravimetric analysis was performed on TGA 2950 (TA Instrument), while dynamic Scanning calorimetry was conducted by DSC 2910 (TA Instrument) with a scanning rate at 10 °C/min under nitrogen flow.

### **6.4.3 Optical and electronic properties analysis**

The UV/Vis absorption was recorded on Shimadzu UV-3600 and a Hitachi U-3010 spectrometer. Fluorescence measurements were recorded on a PerkinElmer LS-55 fluorimeter or PTI QM-30.

UPS were performed on Omicron technology Model ESCA+S with a He I (21.2 eV) excitation source and a PHI QUANTUM 2000 ESCA hemispherical analyzer. The analyzer chamber was maintained at  $< 8 \times 10^{-9}$  mbar. A sample bias of  $-3$  V was applied to avoid charging during measurements, thus, all the raw spectra were positively shifted by 3 eV.

#### **6.4.4 Morphology characterization**

Grazing incidence X-ray scattering characterization of the films was performed at the Stanford Synchrotron Radiation Lightsource (SSRL) on beam lines 2-1, and 11-3. The scattering intensity was recorded on a 2-D image plate (MAR-345) with a pixel size of  $150 \mu\text{m}$  ( $2300 \times 2300$  pixels). The samples were  $\sim 10$  mm long in the direction of the beam path, and the detector was located at a distance of 400 mm from the sample center (distance calibrated using a Lanthanum hexaboride standard).

TEM was conducted on JEOL 2000 FX MARK II with  $\text{LaB}_6$  lamp. The samples were prepared by drop-casting the PA-SB fibers solutions on carbon covered copper grids.

#### **6.4.5 Interface characterization**

Film thickness of azulene copolymers was measured by ellipsometry (Gaertner®-LSE 2020-AK).

Contact angle measurements were obtained using a VCA Optima surface analysis system with a drop size of  $0.5 \mu\text{L}$ . Contact angles were taken immediately

after droplet deposition on the surface, and averaged over three drops in various locations on the sample.

X-ray photoelectron spectroscopy (XPS) was recorded from Physical Electronics, Inc. USA (PHI) Quantum 2000 Scanning ESCA microprobe at 45° take off angle.

The uniformity and surface morphology of thin films on active layers were examined under the atomic force microscope (AFM) (Nanoscope III, Digital Instrument Co., Santa Barbara, CA) in tapping mode utilizing SiN tips.

The carbon K-edge NEXAFS spectra were recorded in partial electron yield mode at beamline U7A of the National Synchrotron Light Source of Brookhaven National Laboratory, probing the top 2-4 nm of the film with a grid bias of -50 V. Series of incident angles were measured with respect to sample normal to reveal polymer orientation at the interfaces. To avoid intensity variations from spot size at different angles, data are normalized to the post-edge intensity at 330 eV.

## APPENDIX

### UTILIZING GOLD NANOPARTICLES AS ELECTRODE MODIFIERS

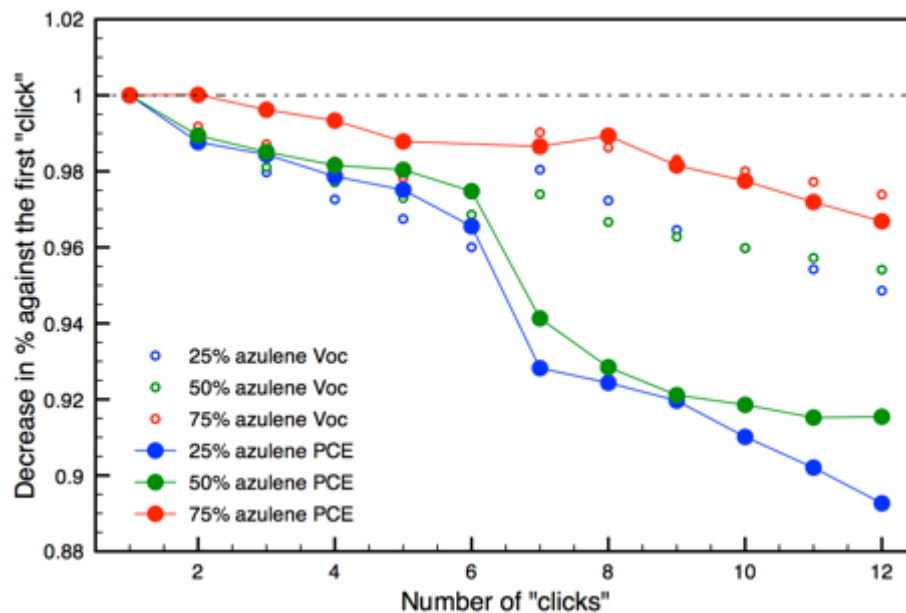


Figure A. 1 The graph showing the decrease in solar cell performance upon successive measurements. PATSBs were used as cathode modifiers. It was found that increasing the azulene density improves interlayer uniformity as well as device stability.

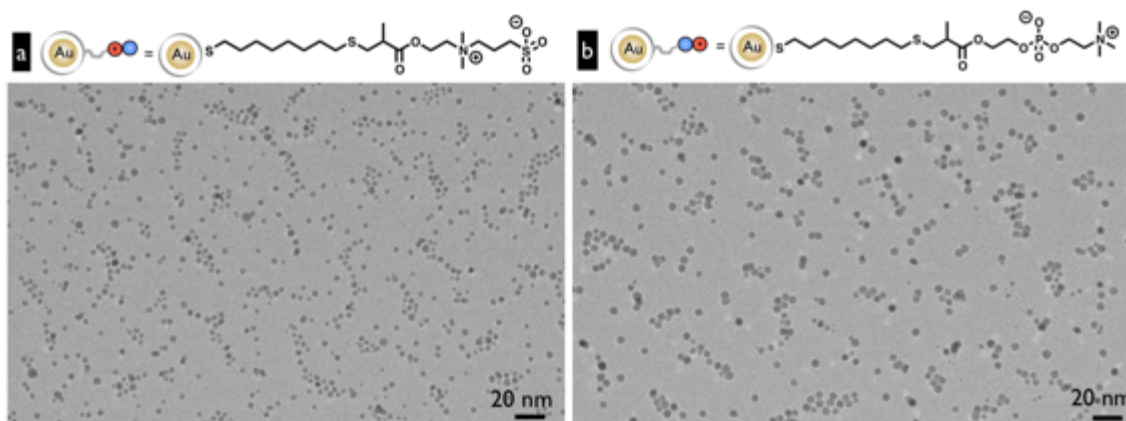


Figure A. 2 Chemical structures and TEM images of (a) sulfobetaine functionalized gold nanoparticles (SB Au-NPs), and (b) phosphorylcholine functionalized gold nanoparticles (PC Au-NPs).

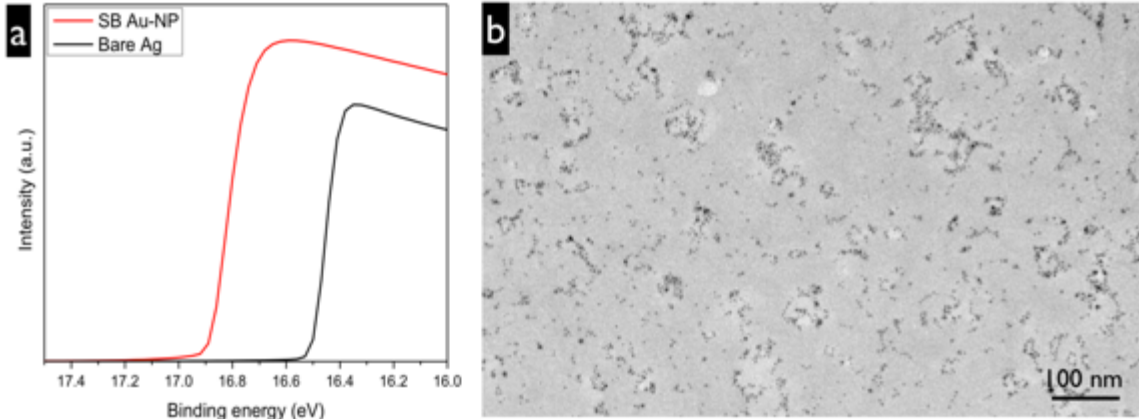


Figure A. 3 (a) UPS spectra of Ag (*black*) and SB Au-NP/Ag (*red*) substrate. A 0.4 eV WF reduction of Ag was observed. (b) TEM image revealing non-uniform coverage of SB Au-NPs on active layer.

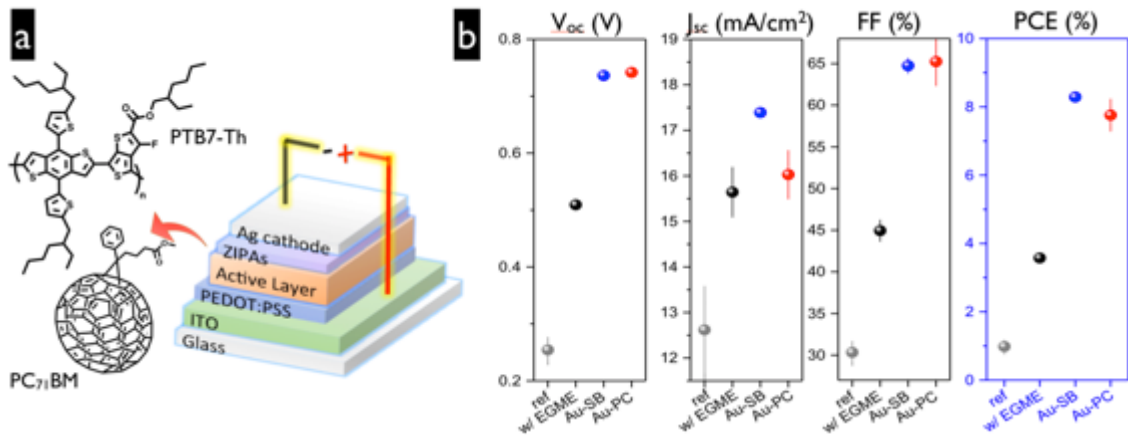


Figure A. 4 (a) Device configuration and chemical structures of PTB7-Th (donor) and PC<sub>71</sub>BM (acceptor). (b) Summary of solar cell performances.

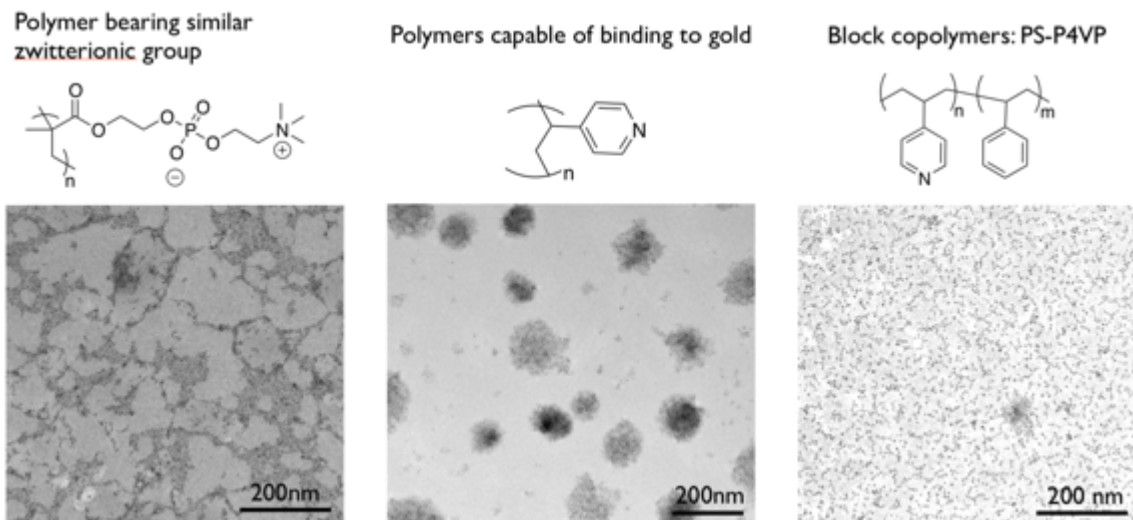


Figure A. 5 TEM images showing the dispersion of PC Au-NPs in corresponding polymer matrices.

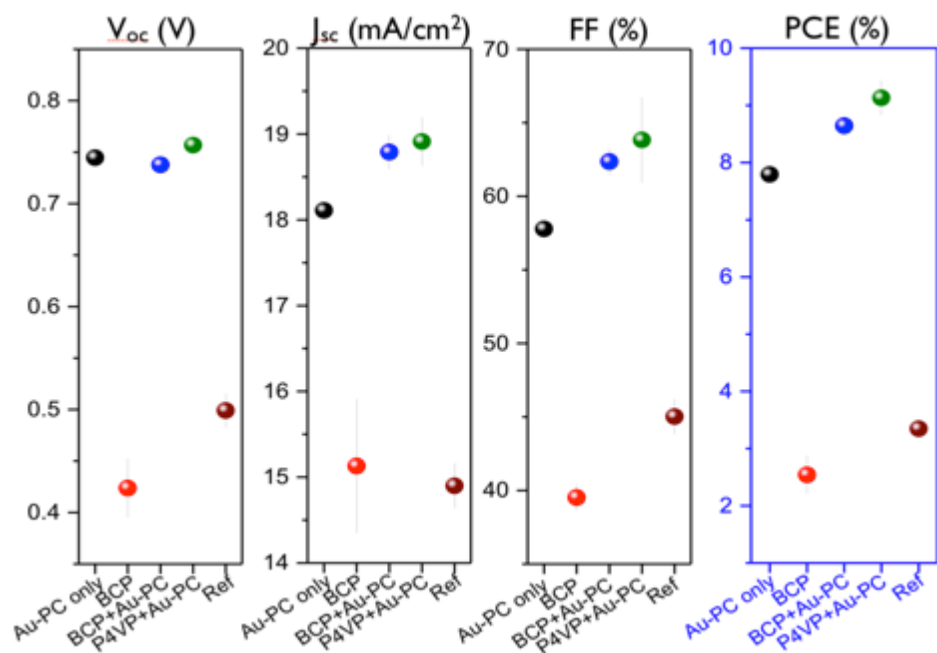


Figure A. 6 Performance of solar cells employing hybrid interlayers: PC Au-NPs with PS-P4VP block copolymers and P4VP.

## BIBLIOGRAPHY

- Bao, Z.; Dodabalapur, A.; Lovinger, A. J. Soluble and Processable Regioregular Poly(3-Hexylthiophene) for Thin Film Field-Effect Transistor Applications with High Mobility. *Appl. Phys. Lett.* **1996**, *69*, 4108–4110.
- Becquerel, A. E. Memoire Sur Les Effects D'Electriques Produits Sous L'Influence Des Rayons Solaires. *Annalen der Physick und Chemie* **1841**, *54*, 35–42.
- Beiley, Z. M.; Hoke, E. T.; Noriega, R.; Dacuña, J.; Burkhard, G. F.; Bartelt, J. A.; Salleo, A.; Toney, M. F.; McGehee, M. D. Morphology-Dependent Trap Formation in High Performance Polymer Bulk Heterojunction Solar Cells. *Adv. Energy Mater.* **2011**, *1*, 954–962.
- Berson, S.; De Bettignies, R.; Bailly, S.; Guillerez, S. Poly (3-Hexylthiophene) Fibers for Photovoltaic Applications. *Adv. Funct. Mater.* **2007**, *17*, 1377–1384.
- Bielawski, C. W.; Grubbs, R. H. Living Ring-Opening Metathesis Polymerization. *Progress in Polymer Science* **2007**, *32*, 1–29.
- Blouin, N.; Michaud, A.; Gendron, D.; Wakim, S.; Blair, E.; Neagu-Plesu, R.; Belletête, M.; Durocher, G.; Tao, Y.; Leclerc, M. Toward a Rational Design of Poly(2,7-Carbazole) Derivatives for Solar Cells. *J. Am. Chem. Soc.* **2008**, *130*, 732–742.
- Blouin, N.; Michaud, A.; Leclerc, M. A Low-Bandgap Poly (2, 7-Carbazole) Derivative for Use in High-Performance Solar Cells. *Adv. Mater.* **2007**, *19*, 2295– 2300.
- Braun, S.; Salaneck, W. R.; Fahlman, M. Energy-Level Alignment at Organic/Metal and Organic/Organic Interfaces. *Adv. Mater.* **2009**, *21*, 1450–1472.
- Breitenkamp, K.; Emrick, T. Novel Polymer Capsules From Amphiphilic Graft Copolymers and Cross-Metathesis. *J. Am. Chem. Soc.* **2003**, *125*, 12070–12071.
- Briseno, A. L.; Mannsfeld, S. C. B.; Shamberger, P. J.; Ohuchi, F. S.; Bao, Z.; Jenekhe, S. A.; Xia, Y. Self-Assembly, Molecular Packing, and Electron Transport in N- Type Polymer Semiconductor Nanobelts. *Chem. Mater.* **2008**, *20*, 4712–4719.
- Bundgaard, E.; Krebs, F. C. Low Band Gap Polymers for Organic Photovoltaics. *Solar Energy Materials and Solar Cells* **2007**, *91*, 954-985.
- Campbell, I.; Rubin, S.; Zawodzinski, T.; Kress, J.; Martin, R.; Smith, D.; Barashkov, N.; Ferraris, J. Controlling Schottky Energy Barriers in Organic Electronic Devices Using Self-Assembled Monolayers. *Phys. Rev. B, Condens. Matter* **1996**, *54*, R14321–R14324.



- Chang, Y.-M.; Zhu, R.; Richard, E.; Chen, C.-C.; Li, G.; Yang, Y. Electrostatic Self-Assembly Conjugated Polyelectrolyte-Surfactant Complex as an Interlayer for High Performance Polymer Solar Cells. *Adv. Funct. Mater.* **2012**, *22*, 3284–3289.
- Chapin, D. M.; Fuller, C. S.; Pearson, G. L. A New Silicon P-N Junction Photocell for Converting Solar Radiation Into Electrical Power. *J. Appl. Phys.* **1954**, *25*, 676–677.
- Chen, D.; Liu, F.; Wang, C.; Nakahara, A.; Russell, T. P. Bulk Heterojunction Photovoltaic Active Layers via Bilayer Interdiffusion. *Nano Lett.* **2011**, *11*, 2071–2078.
- Chen, D.; Nakahara, A.; Wei, D.; Nordlund, D.; Russell, T. P. P3HT/PCBM Bulk Heterojunction Organic Photovoltaics: Correlating Efficiency and Morphology. *Nano Lett.* **2011**, *11*, 561–567.
- Chen, W.; Xu, T.; He, F.; Wang, W.; Wang, C.; Strzalka, J.; Liu, Y.; Wen, J.; Miller, D. J.; Chen, J.; et al. Hierarchical Nanomorphologies Promote Exciton Dissociation in Polymer/Fullerene Bulk Heterojunction Solar Cells. *Nano Lett.* **2011**, *11*, 3707–3713.
- Cho, N.; Yip, H.-L.; Hau, S. K.; Chen, K.-S.; Kim, T.-W.; Davies, J. A.; Zeigler, D. F.; Jen, A. K. Y. N-Doping of Thermally Polymerizable Fullerenes as an Electron Transporting Layer for Inverted Polymer Solar Cells. *J. Mater. Chem.* **2011**, *21*, 6956–6961.
- Cho, S.; Lee, K.; Yuen, J.; Wang, G.; Moses, D.; Heeger, A. J.; Surin, M.; Lazzaroni, R. Thermal Annealing-Induced Enhancement of the Field-Effect Mobility of Regioregular Poly(3-Hexylthiophene) Films. *J. Appl. Phys.* **2006**, *100*, 114503.
- Choi, D. C.; Kim, S. H.; Lee, J. H.; Cho, H. N.; Choi, S. K. A New Class of Conjugated Ionic Polyacetylenes .3. Cyclopolymerization of Alkyldipropargyl(4-Sulfobutyl)Ammonium Betaines by Transition Metal Catalysts. *Macromolecules* **1997**, *30*, 176–181.
- Choi, T. L.; Grubbs, R. H. Controlled Living Ring-Opening-Metathesis Polymerization by a Fast-Initiating Ruthenium Catalyst. *Angew. Chem. Int. Ed.* **2003**, *42*, 1743–1746.
- Christensen, R. L.; Faksh, A.; Meyers, J. A.; Samuel, I. D. W.; Wood, P.; Schrock, R. R.; Hultsch, K. C. Optical Spectroscopy of Long Polyenes. *J. Phys. Chem. A* **2004**, *108*, 8229–8236.
- Christensen, R. L.; Galinato, M. G. I.; Chu, E. F.; Howard, J. N.; Broene, R. D.; Frank, H. A. Energies of Low-Lying Excited States of Linear Polyenes. *J. Phys. Chem. A* **2008**, *112*, 12629–12636.

- Churchill, M. R. Transition Metal Complexes of Azulene and Related Ligands. In; Progress in Inorganic Chemistry: Hoboken, NJ, USA, 1970; Vol. 11, pp. 53–98.
- Craig, N. C.; Demaison, J.; Groner, P.; Rudolph, H. D.; Vogt, N. Electron Delocalization in Polyenes: a Semiexperimental Equilibrium Structure for (3E)-1, 3, 5-Hexatriene and Theoretical Structures for (3Z, 5Z)-, (3E, 5E)-, and (3E, 5Z)-1, 3, 5, 7-Octatetraene. *J. Phys. Chem. A* **2015**, *119*, 195–204.
- Crispin, X.; Geskin, V.; Crispin, A.; Cornil, J.; Lazzaroni, R.; Salaneck, W.R.; Brédas, J. L. Characterization of the Interface Dipole at Organic/ Metal Interfaces. *J. Am. Chem. Soc.* **2002**, *124*, 8131–8141.
- Czekelius, C.; Hafer, J.; Tonzetich, Z. J.; Schrock, R. R.; Christensen, R. L.; Müller, P. Synthesis of Oligoenes That Contain Up to 15 Double Bonds From 1,6-Heptadiynes. *J. Am. Chem. Soc.* **2006**, *128*, 16664–16675.
- Di Nuzzo, D.; Aguirre, A.; Shahid, M.; Gevaerts, V. S.; Meskers, S. C.; Janssen, R. A. Improved Film Morphology Reduces Charge Carrier Recombination Into the Triplet Excited State in a Small Bandgap Polymer-Fullerene Photovoltaic Cell. *Adv. Mater.* **2010**, *22*, 4321–4324.
- Du, C.; Li, W.; Duan, Y.; Li, C.; Dong, H.; Zhu, J.; Hu, W.; Bo, Z. Conjugated Polymers with 2,7-Linked 3,6-Difluorocarbazole as Donor Unit for High Efficiency Polymer Solar Cells. *Polym. Chem.* **2013**, *4*, 2773–2782.
- Duan, C.; Wang, L.; Zhang, K.; Guan, X.; Huang, F. Conjugated Zwitterionic Polyelectrolytes and Their Neutral Precursor as Electron Injection Layer for High- Performance Polymer Light-Emitting Diodes. *Adv. Mater.* **2011**, *23*, 1665–1669.
- Duan, C.; Zhang, K.; Guan, X.; Zhong, C.; Xie, H.; Huang, F.; Chen, J.; Peng, J.; Cao, Y. Conjugated Zwitterionic Polyelectrolyte-Based Interface Modification Materials for High Performance Polymer Optoelectronic Devices. *Chem. Sci.* **2013**, *4*, 1298–1307.
- Ellison, D. J.; Lee, B.; Podzorov, V. Surface Potential Mapping of SAM-Functionalized Organic Semiconductors by Kelvin Probe Force Microscopy. *Adv. Mater.* **2011**, *23*, 502–507.
- Fang, J.; Wallikewitz, B. H.; Gao, F.; Tu, G.; Müller, C.; Pace, G.; Friend, R. H.; Huck, W. T. Conjugated Zwitterionic Polyelectrolyte as the Charge Injection Layer for High-Performance Polymer Light-Emitting Diodes. *J. Am. Chem. Soc.* **2011**, *133*, 683–685.
- Förster, S.; Antonietti, M. Amphiphilic Block Copolymers in Structure-Controlled Nanomaterial Hybrids. *Adv. Mater.* **1998**, *10*, 195–217.

- Fritts, C. E. On a New Form of Selenium Cell, and Some Electrical Discoveries Made by Its Use. *American Journal of Science* **1883**, s3-26, 465–472.
- Goldman, G. D.; Lemal, D. M. Synthesis of Azulene, a Blue Hydrocarbon. *Journal of Chemical Education*, **1988**, 65, 923-925.
- Green, M. A.; Emery, K.; Hishikawa, Y.; Warta, W.; Dunlop, E. D. Solar Cell Efficiency Tables (Version 45). *Progress in Photovoltaics* **2015**, 23, 1–9.
- Greiner, M. T. Universal Energy-Level Alignment of Molecules on Metal Oxides. *Nat. Mater.* **2011**, 11, 76–81.
- Gu, Y.; Wang, C.; Liu, F.; Chen, J.; Dyck, O. E.; Duscher, G.; Russell, T. P. Guided Crystallization of P3HT in Ternary Blend Solar Cell Based on P3HT:PCPDTBT:PCBM. *Energy Environ. Sci.* **2014**, 7, 3782–3790.
- Gu, Y.; Wang, C.; Russell, T. P. Multi-Length-Scale Morphologies in PCPDTBT/PCBM Bulk-Heterojunction Solar Cells. *Adv. Energy Mater.* **2012**, 2, 683–690.
- Guan, X.; Zhang, K.; Huang, F.; Bazan, G. C.; Cao, Y. Amino N-Oxide Functionalized Conjugated Polymers and Their Amino-Functionalized Precursors: New Cathode Interlayers for High-Performance Optoelectronic Devices. *Adv. Funct. Mater.* **2012**, 22, 2846–2854.
- Halls, J. J. M.; Walsh, C. A.; Greenham, N. C.; Marseglia, E. A.; Friend, R. H.; Moratti, S. C.; Holmes, A. B. Efficient Photodiodes From Interpenetrating Polymer Networks. *Nature* **1995**, 376, 498–500.
- He, C.; Zhong, C.; Wu, H.; Yang, R.; Yang, W.; Huang, F.; Bazan, G. C.; Cao, Y. Origin of the Enhanced Open-Circuit Voltage in Polymer Solar Cells via Interfacial Modification Using Conjugated Polyelectrolytes. *J. Mater. Chem.* **2010**, 20, 2617–2622.
- He, Z.; Wu, H.; Cao, Y. Recent Advances in Polymer Solar Cells: Realization of High Device Performance by Incorporating Water/Alcohol-Soluble Conjugated Polymers as Electrode Buffer Layer. *Adv. Mater.* **2014**, 26, 1006–1024.
- He, Z.; Xiao, B.; Liu, F.; Wu, H.; Yang, Y.; Xiao, S.; Wang, C.; Russell, T. P.; Cao, Y. Single-Junction Polymer Solar Cells with High Efficiency and Photovoltage. *Nature Photon.* **2015**, 9, 174–179.
- He, Z.; Zhang, C.; Xu, X.; Zhang, L.; Huang, L.; Chen, J.; Wu, H.; Cao, Y. Largely Enhanced Efficiency with a PFN/Al Bilayer Cathode in High Efficiency Bulk Heterojunction Photovoltaic Cells with a Low Bandgap Polycarbazole Donor. *Adv. Mater.* **2011**, 23, 3086–3089.

- He, Z.; Zhong, C.; Huang, X.; Wong, W.-Y.; Wu, H.; Chen, L.; Su, S.; Cao, Y. Simultaneous Enhancement of Open-Circuit Voltage, Short-Circuit Current Density, and Fill Factor in Polymer Solar Cells. *Adv. Mater.* **2011**, *23*, 4636–4643.
- He, Z.; Zhong, C.; Su, S.; Xu, M.; Wu, H.; Cao, Y. Enhanced Power-Conversion Efficiency in Polymer Solar Cells Using an Inverted Device Structure. *Nature Photon.* **2012**, *6*, 591–595.
- Hiramoto, M.; Fujiwara, H.; Yokoyama, M. P-I-N Like Behavior in Three-Layered Organic Solar Cells Having a Co-Deposited Interlayer of Pigments. *J. Appl. Phys.* **1992**, *72*, 3781.
- Hoppe, H.; Glatzel, T.; Niggemann, M.; Schwinger, W. Efficiency Limiting Morphological Factors of MDMO-PPV: PCBM Plastic Solar Cells. *Thin Solid Films* **2006**, *511-512*, 587-592
- Hoppe, H.; Niggemann, M.; Winder, C.; Kraut, J. Nanoscale Morphology of Conjugated Polymer/Fullerene-Based Bulk-Heterojunction Solar Cells. *Adv. Funct. Mater.* **2004**, *14*, 1005–1011.
- Hung, L. S.; Tang, C. W.; Mason, M. G. Enhanced Electron Injection in Organic Electroluminescence Devices Using an Al/LiF Electrode. *Appl. Phys. Lett.* **1997**, *70*, 152–154.
- Husein, T. A.; Schuster, S.; Egger, D. A. The Effects of Embedded Dipoles in Aromatic Self-Assembled Monolayers. *Adv. Funct. Mater.* **2015**, *25*, 3943–3957.
- Ihn, K. J.; Moulton, J.; Smith, P. Whiskers of Poly(3-Alkylthiophene)S. *J. Polym. Sci. B Polym. Phys.* **1993**, *31*, 735–742.
- Ishii, H.; Sugiyama, K.; Ito, E.; Seki, K. Energy Level Alignment and Interfacial Electronic Structures at Organic/Metal and Organic/Organic Interfaces. *Adv. Mater.* **1999**, *11*, 605–625.
- Jabbour, G. E.; Kippelen, B.; Armstrong, N. R. Aluminum Based Cathode Structure for Enhanced Electron Injection in Electroluminescent Organic Devices. *Appl. Phys. Lett.* **1998**, *73*, 1185–1187.
- Kang, E.-H.; Choi, T.-L. Coil-to-Rod Transition of Conjugated Polymers Prepared by Cyclopolymerization of 1,6-Heptadiynes. *ACS Macro Lett.* **2013**, *2*, 780–784.
- Kang, E.-H.; Lee, I. S.; Choi, T.-L. Ultrafast Cyclopolymerization for Polyene Synthesis: Living Polymerization to Dendronized Polymers. *J. Am. Chem. Soc.* **2011**, *133*, 11904–11907.

- Kang, E.-H.; Lee, I.-H.; Choi, T.-L. Brush Polymers Containing Semiconducting Polyene Backbones: Graft-Through Synthesis via Cyclopolymerization and Conformational Analysis on the Coil-to-Rod Transition. *ACS Macro Lett.* **2012**, *1*, 1098–1102.
- Kang, E.-H.; Yu, S. Y.; Lee, I. S.; Park, S. E.; Choi, T.-L. Strategies to Enhance Cyclopolymerization Using Third-Generation Grubbs Catalyst. *J. Am. Chem. Soc.* **2014**, *136*, 10508–10514.
- Kang, H.; Hong, S.; Lee, J.; Lee, K. Organic Electronics: Electrostatically Self-Assembled Nonconjugated Polyelectrolytes as an Ideal Interfacial Layer for Inverted Polymer Solar Cells. *Adv. Mater.* **2012**, *24*, 3005–3009.
- Kim, J. S.; Lee, J. H.; Park, J. H.; Shim, C.; Sim, M.; Cho, K. High-Efficiency Organic Solar Cells Based on Preformed Poly(3-Hexylthiophene) Nanowires. *Adv. Funct. Mater.* **2010**, *21*, 480–486.
- Kiriy, N.; Jähne, E.; Adler, H.-J.; Schneider, M.; Kiriy, A.; Gorodyska, G.; Minko, S.; Jehnichen, D.; Simon, P.; Fokin, A. A.; et al. One-Dimensional Aggregation of Regioregular Polyalkylthiophenes. *Nano Lett.* **2003**, *3*, 707–712.
- Koh, H.-D.; Park, S.; Russell, T. P. Fabrication of Pt/Au Concentric Spheres From Triblock Copolymer. *ACS Nano* **2010**, *4*, 1124–1130.
- Kratz, K.; Breitenkamp, K.; Hule, R.; Pochan, D. PC-Polyolefins: Synthesis and Assembly Behavior in Water. *Macromolecules* **2009**, *42*, 3227–3229.
- Krebs, F. C. Fabrication and Processing of Polymer Solar Cells: a Review of Printing and Coating Techniques. *Solar Energy Materials and Solar Cells* **2009**, *93*, 394–412.
- Krebs, F. C. Polymer Solar Cell Modules Prepared Using Roll-to-Roll Methods: Knife-Over-Edge Coating, Slot-Die Coating and Screen Printing. *Solar Energy Materials and Solar Cells* **2009**, *93*, 465–475.
- Krebs, F. C.; Gevorgyan, S. A.; Alstrup, J. A Roll-to-Roll Process to Flexible Polymer Solar Cells: Model Studies, Manufacture and Operational Stability Studies. *J. Mater. Chem.* **2009**, *19*, 5442–5451.
- Kumar, A.; Pace, G.; Bakulin, A. A.; Fang, J.; Ho, P. K. H.; Huck, W. T. S.; Friend, R. H.; Greenham, N. C. Donor-Acceptor Interface Modification by Zwitterionic Conjugated Polyelectrolytes in Polymer Photovoltaics. *Energy Environ. Sci.* **2013**, *6*, 1589–1596.

- Kumar, P. S.; Wurst, K.; Buchmeiser, M. R. Factors Relevant for the Regioselective Cyclopolymerization of 1, 6-Heptadiynes, N, N-Dipropargylamines, N, N-Dipropargylammonium Salts, and Dipropargyl Ethers by RuIV– Alkylidene-Based Metathesis Initiators. *J. Am. Chem. Soc.* **2008**, *131*, 387–395.
- Lacroix, P.; Malfant, I.; Iftime, G.; Razus, A.; Nakatani, K.; Delaire, J. Azo-Azulene Derivatives as Second-Order Nonlinear Optical Chromophores. *Chemistry* **2000**, *6*, 2599–2608.
- Langsdorf, B. L.; Zhou, X.; Adler, D. H.; Lonergan, M. C. Synthesis and Characterization of Soluble, Ionically Functionalized Polyacetylenes. *Macromolecules* **1999**, *32*, 2796–2798.
- Lee, H.; Puodziukynaite, E.; Zhang, Y.; Stephenson, J. C.; Richter, L. J.; Fischer, D. A.; DeLongchamp, D. M.; Emrick, T.; Briseno, A. L. Poly(Sulfobetaine Methacrylate)S as Electrode Modifiers for Inverted Organic Electronics. *J. Am. Chem. Soc.* **2015**, *137*, 540–549.
- Li, C.-Z.; Chueh, C.-C.; Ding, F.; Yip, H.-L.; Liang, P.-W.; Li, X.; Jen, A. K. Y. Doping of Fullerenes via Anion-Induced Electron Transfer and Its Implication for Surfactant Facilitated High Performance Polymer Solar Cells. *Adv. Mater.* **2013**, *25*, 4425–4430.
- Li, G.; Shrotriya, V.; Huang, J.; Yao, Y.; Moriarty, T.; Emery, K.; Yang, Y. High-Efficiency Solution Processable Polymer Photovoltaic Cells by Self-Organization of Polymer Blends. *Nat. Mater.* **2005**, *4*, 864–868.
- Li, G.; Yao, Y.; Yang, H.; Shrotriya, V.; Yang, G.; Yang, Y. “Solvent Annealing” Effect in Polymer Solar Cells Based on Poly(3-Hexylthiophene) and Methanofullerenes. *Adv. Funct. Mater.* **2007**, *17*, 1636–1644.
- Li, G.; Zhu, R.; Yang, Y. Polymer Solar Cells. *Nature Photon.* **2012**, *6*, 153–161.
- Li, L.; Lu, G.; Yang, X. Improving Performance of Polymer Photovoltaic Devices Using an Annealing-Free Approach via Construction of Ordered Aggregates in Solution. *J. Mater. Chem.* **2008**, *18*, 1984–1990.
- Liang, Y.; Xu, Z.; Xia, J.; Tsai, S.-T.; Wu, Y.; Li, G.; Ray, C.; Yu, L. For the Bright Future-Bulk Heterojunction Polymer Solar Cells with Power Conversion Efficiency of 7.4%. *Adv. Mater.* **2010**, *22*, E135–E138.
- Liliana Cristian; Isabelle Sasaki; Pascal G Lacroix, A.; Donnadiou, B.; and, I. A.; Clays, K.; Razus, A. C. Donating Strength of Azulene in Various Azulen-1-Yl- Substituted Cationic Dyes: Application in Nonlinear Optics. *Chem. Mater.* **2004**, 3543–3551.
- Liu, F.; Gu, Y.; Jung, J. W.; Jo, W. H.; Russell, T. P. On the Morphology of Polymer-Based Photovoltaics. *J. Polym. Sci. B Polym. Phys.* **2012**, *50*, 1018–1044.

- Liu, F.; Gu, Y.; Wang, C.; Zhao, W.; Chen, D.; Briseno, A. L.; Russell, T. P. Efficient Polymer Solar Cells Based on a Low Bandgap Semi-Crystalline DPP Polymer-PCBM Blends. *Adv. Mater.* **2012**, *24*, 3947–3951.
- Liu, F.; Page, Z. A.; Duzhko, V. V.; Russell, T. P.; Emrick, T. Conjugated Polymeric Zwitterions as Efficient Interlayers in Organic Solar Cells. *Adv. Mater.* **2013**, *25*, 6868–6873.
- Liu, F.; Zhao, W.; Tumbleston, J. R.; Wang, C.; Gu, Y.; Wang, D.; Briseno, A. L.; Ade, H.; Russell, T. P. Understanding the Morphology of PTB7:PCBM Blends in Organic Photovoltaics. *Adv. Energy Mater.* **2013**, *4*, 1301377.
- Liu, J.; Arif, M.; Zou, J.; Khondaker, S. I.; Zhai, L. Controlling Poly (3-Hexylthiophene) Crystal Dimension: Nanowhiskers and Nanoribbons. *Macromolecules* **2009**, *42*, 9390–9393.
- Liu, S.; Zhang, K.; Lu, J.; Zhang, J.; Yip, H.-L.; Huang, F.; Cao, Y. High-Efficiency Polymer Solar Cells via the Incorporation of an Amino-Functionalized Conjugated Metallopolymer as a Cathode Interlayer. *J. Am. Chem. Soc.* **2013**, *135*, 15326–15329.
- Liu, Y.; Page, Z. A.; Russell, T. P.; Emrick, T. Finely Tuned Polymer Interlayers Enhance Solar Cell Efficiency. *Angew. Chem. Int. Ed.* **2015**, *54*, 11485–11489.
- Lu, X.; Hlaing, H.; Germack, D. S.; Peet, J.; Jo, W. H.; Andrienko, D.; Kremer, K.; Ocko, B. M. Bilayer Order in a Polycarbazole-Conjugated Polymer. *Nat. Commun.* **2012**, *3*, 795.
- Ma, H.; Yip, H.-L.; Huang, F.; Jen, A. K. Y. Interface Engineering for Organic Electronics. *Adv. Funct. Mater.* **2010**, *20*, 1371–1388.
- McCulloch, B.; Ho, V.; Hoarfrost, M.; Stanley, C.; Do, C.; Heller, W. T.; Segalman, R. A. Polymer Chain Shape of Poly (3-Alkylthiophenes) in Solution Using Small-Angle Neutron Scattering. *Macromolecules* **2013**, *46*, 1899–1907.
- Mihailetchi, V. D.; Blom, P. W. M.; Hummelen, J. C.; Rispen, M. T. Cathode Dependence of the Open-Circuit Voltage of Polymer:Fullerene Bulk Heterojunction Solar Cells. *J. Appl. Phys.* **2003**, *94*, 6849.
- Murai, M.; Amir, E.; Amir, R. J.; Hawker, C. J. Azulene-Based Conjugated Polymers: Unique Seven-Membered Ring Connectivity Leading to Stimuli-Responsiveness. *Chem. Sci.* **2012**, *3*, 2721.
- Na, S.-I.; Kim, T.-S.; Oh, S.-H.; Kim, J.; Kim, S.-S.; Kim, D.-Y. Enhanced Performance of Inverted Polymer Solar Cells with Cathode Interfacial Tuning via Water-Soluble Polyfluorenes. *Appl. Phys. Lett.* **2010**, *97*, 223305.

- Oh, J. Y.; Shin, M.; Lee, T. I.; Jang, W. S.; Min, Y.; Myoung, J.-M.; Baik, H. K.; Jeong, U. Self-Seeded Growth of Poly (3-Hexylthiophene)(P3HT) Nanofibrils by a Cycle of Cooling and Heating in Solutions. *Macromolecules* **2012**, *45*, 7504– 7513.
- Oh, S.-H.; Na, S.-I.; Jo, J.; Lim, B.; Vak, D.; Kim, D.-Y. Water-Soluble Polyfluorenes as an Interfacial Layer Leading to Cathode-Independent High Performance of Organic Solar Cells. *Adv. Funct. Mater.* **2010**, *20*, 1977–1983.
- Ouyang, X.; Peng, R.; Ai, L.; Zhang, X.; Ge, Z. Efficient Polymer Solar Cells Employing a Non-Conjugated Small-Molecule Electrolyte. *Nature Photon.* **2015**, *9*, 520– 524.
- Padinger, F.; Rittberger, R. S.; Sariciftci, N. S. Effects of Postproduction Treatment on Plastic Solar Cells. *Adv. Funct. Mater.* **2003**, *13*, 85–88.
- Page, Z. A.; Duzhko, V. V.; Emrick, T. Conjugated Thiophene-Containing Polymer Zwitterions: Direct Synthesis and Thin Film Electronic Properties. *Macromolecules* **2013**, *46*, 344–351.
- Page, Z. A.; Liu, F.; Russell, T. P.; Emrick, T. Rapid, Facile Synthesis of Conjugated Polymer Zwitterions in Ionic Liquids. *Chem. Sci.* **2014**, *5*, 2368–2373.
- Page, Z. A.; Liu, Y.; Duzhko, V. V.; Russell, T. P.; Emrick, T. Fulleropyrrolidine Interlayers: Tailoring Electrodes to Raise Organic Solar Cell Efficiency. *Science* **2014**, *346*, 441–444.
- Park, S. H.; Roy, A.; Beaupré, S.; Cho, S.; Coates, N.; Moon, J. S.; Moses, D.; Leclerc, M.; Lee, K.; Heeger, A. J. Bulk Heterojunction Solar Cells with Internal Quantum Efficiency Approaching 100%. *Nature Photon.* **2009**, *3*, 297–302.
- Peet, J.; Kim, J. Y.; Coates, N. E.; Ma, W. L.; Moses, D.; Heeger, A. J.; Bazan, G. C. Efficiency Enhancement in Low-Bandgap Polymer Solar Cells by Processing with Alkane Dithiols. *Nat. Mater.* **2007**, *6*, 497–500.
- Perlin, J. From Space to Earth — the Story of Solar Electricity; Harvard University Press, 1999.
- Peters, C. H.; Sachs-Quintana, I. T.; Kastrop, J. P.; Beaupré, S.; Leclerc, M.; McGehee, M. D. High Efficiency Polymer Solar Cells with Long Operating Lifetimes. *Adv. Energy Mater.* **2011**, *1*, 491–494.
- Puodziukynaite, E.; Wang, H.-W.; Lawrence, J.; Wise, A. J.; Russell, T. P.; Barnes, M. D.; Emrick, T. Azulene Methacrylate Polymers: Synthesis, Electronic Properties, and Solar Cell Fabrication. *J. Am. Chem. Soc.* **2014**, *136*, 11043–11049.
- Qiu, L.; Lee, W. H.; Wang, X.; Kim, J. S.; Lim, J. A.; Kwak, D.; Lee, S.; Cho, K. Organic Thin-Film Transistors Based on Polythiophene Nanowires Embedded in Insulating Polymer. *Adv. Mater.* **2009**, *21*, 1349–1353.



- Qiu, X.-Y.; Jiang, M.-W.; Guo, C.-G.; He, Y.-J.; Wang, C.-Q. Self-Assembled Nano- Wire of an Amphiphilic Biodegradable Oligosaccharide-Based Graft Copolymer in Water. *Carbohydrate Polymers* **2012**, *87*, 2306–2312.
- Reese, M. O.; White, M. S.; Rumbles, G.; Ginley, D. S.; Shaheen, S. E. Optimal Negative Electrodes for Poly(3-Hexylthiophene): [6,6]-Phenyl C61-Butyric Acid Methyl Ester Bulk Heterojunction Photovoltaic Devices. *Appl. Phys. Lett.* **2008**, *92*, 053307.
- Rivnay, J.; Mannsfeld, S. C.; Miller, C. E.; Salleo, A.; Toney, M. F. Quantitative Determination of Organic Semiconductor Microstructure From the Molecular to Device Scale. *Chem. Rev.* **2012**, *112*, 5488–5519.
- Saga, T. Advances in Crystalline Silicon Solar Cell Technology for Industrial Mass Production. *NPG Asia Mater* **2010**, *2*, 96–102.
- Salaneck, W. R. Photoelectron Spectroscopy of Polyconjugated Polymer Surfaces and Interfaces. *Rep. Prog. Phys.* **1999**, *54*, 1215–1249.
- Salman, H.; Abraham, Y.; Tal, S.; Meltzman, S.; Kapon, M.; Tessler, N.; Speiser, S.; Eichen, Y. 1,3-Di(2-Pyrrolyl)Azulene: an Efficient Luminescent Probe for Fluoride. *Eur. J. Org. Chem.* **2005**, *2005*, 2207–2212.
- Samitsu, S.; Shimomura, T.; Heike, S.; Hashizume, T.; Ito, K. Effective Production of Poly (3-Alkylthiophene) Nanofibers by Means of Whisker Method Using Anisole Solvent: Structural, Optical, and Electrical Properties. *Macromolecules* **2008**, *41*, 8000–8010.
- Samitsu, S.; Shimomura, T.; Heike, S.; Hashizume, T.; Ito, K. Field-Effect Carrier Transport in Poly (3-Alkylthiophene) Nanofiber Networks and Isolated Nanofibers. *Macromolecules* **2010**, *43*, 7891–7894.
- Samitsu, S.; Shimomura, T.; Ito, K. Nanofiber Preparation by Whisker Method Using Solvent-Soluble Conducting Polymers. *Thin Solid Films* **2008**, *516*, 2478–2486.
- Sariciftci, N. S.; Braun, D.; Zhang, C.; Srdanov, V. I. Semiconducting Polymer-Buckminsterfullerene Heterojunctions: Diodes, Photodiodes, and Photovoltaic Cells. *Appl. Phys. Lett.* **1993**, *62*, 585-587.
- Seo, J. H.; Nguyen, T.-Q. Electronic Properties of Conjugated Polyelectrolyte Thin Films. *J. Am. Chem. Soc.* **2008**, *130*, 10042–10043.
- Seo, J. H.; Yang, R.; Brzezinski, J. Z.; Walker, B.; Bazan, G. C.; Nguyen, T.-Q. Electronic Properties at Gold/Conjugated-Polyelectrolyte Interfaces. *Adv. Mater.* **2009**, *21*, 1006–1011.

- Sirringhaus, H.; Brown, P. J.; Friend, R. H.; Nielsen, M. M.; Bechgaard, K.; Langeveld-Voss, B. M. W.; Spiering, A. J. H.; Janssen, R. A. J.; Meijer, E. W.; Herwig, P.; et al. Two-Dimensional Charge Transport in Self-Organized, High-Mobility Conjugated Polymers. *Nature* **1999**, *401*, 685–688.
- Steim, R.; Ameri, T.; Schilinsky, P.; Waldauf, C.; Dennler, G.; Scharber, M.; Brabec, C. J. Organic Photovoltaics for Low Light Applications. *Solar Energy Materials and Solar Cells* **2011**, *95*, 3256–3261.
- Sun, J.; Zhu, Y.; Xu, X.; Lan, L.; Zhang, L.; Cai, P.; Chen, J.; Peng, J.; Cao, Y. High Efficiency and High Voc Inverted Polymer Solar Cells Based on a Low-Lying HOMO Polycarbazole Donor and a Hydrophilic Polycarbazole Interlayer on ITO Cathode. *J. Phys. Chem. C* **2012**, *116*, 14188–14198.
- Sung-Hyun Kim; Yun-Hi Kim; Hyun-Nam Cho; Soon-Ki Kwon; Hwan-Kyu Kim, A.; Sam-Kwon Choi. Unusual Optical Absorption Behavior, Polymer Structure, and Air Stability of Poly(1,6-Heptadiyne)s with Substituents at the 4-Position. *Macromolecules* **1996**, *29*, 5422–5426.
- Szarko, J. M.; Guo, J.; Liang, Y.; Lee, B.; Rolczynski, B. S.; Strzalka, J.; Xu, T.; Loser, S.; Marks, T. J.; Yu, L.; et al. When Function Follows Form: Effects of Donor Copolymer Side Chains on Film Morphology and BHJ Solar Cell Performance. *Adv. Mater.* **2010**, *22*, 5468–5472.
- Tang, C. W. Two-Layer Organic Photovoltaic Cell. *Appl. Phys. Lett.* **1986**, *48*, 183–185.
- Tang, Z.; Tress, W.; Bao, Q.; Jafari, M. J.; Bergqvist, J.; Ederth, T.; Andersson, M. R.; Inganäs, O. Improving Cathodes with a Polymer Interlayer in Reversed Organic Solar Cells. *Adv. Energy Mater.* **2014**, *4*, 1400643.
- Traiphol, R.; Charoenthai, N.; Sriksirin, T.; Kerdeharoen, T.; Osotchan, T.; Maturros, T. Chain Organization and Photophysics of Conjugated Polymer in Poor Solvents: Aggregates, Agglomerates and Collapsed Coils. *Polymer* **2007**, *48*, 813–826.
- Treat, N. D.; Chabiny, M. L. Phase Separation in Bulk Heterojunctions of Semiconducting Polymers and Fullerenes for Photovoltaics. *Annu Rev Phys Chem* **2014**, *65*, 59–81.
- Trnka, T. M.; Morgan, J. P.; Sanford, M. S.; Wilhelm, T. E.; Scholl, M.; Choi, T. L.; Ding, S.; Day, M. W.; Grubbs, R. H. Synthesis and Activity of Ruthenium Alkylidene Complexes Coordinated with Phosphine and N-Heterocyclic Carbene Ligands. *J. Am. Chem. Soc.* **2003**, *125*, 2546–2558.
- van Duren, J. K. J.; Yang, X.; Loos, J.; Bulle-Lieuwma, C. W. T.; Sieval, A. B.; Hummelen, J. C.; Janssen, R. A. J. Relating the Morphology of Poly(P-Phenylene Vinylene)/Methanofullerene Blends to Solar-Cell Performance. *Adv. Funct. Mater.* **2004**, *14*, 425–434.

- van Reenen, S.; Kouijzer, S.; Janssen, R. Origin of Work Function Modification by Ionic and Amine-Based Interface Layers. *Adv. Mater. Interfaces* **2014**, *1*, 1400189.
- Vygodskii, Y. S.; Shaplov, A. S.; Lozinskaya, E. I.; Vlasov, P. S.; Malyshkina, I. A.; Gavrilova, N. D.; Santhosh Kumar, P.; Buchmeiser, M. R. Cyclopolymerization of N, N-Dipropargylamines and N, N-Dipropargyl Ammonium Salts. *Macromolecules* **2008**, *41*, 1919–1928.
- Wada, E.; Nakai, T.; Okawara, M. Synthesis and Polymerization of Acrylates Containing Azulene Structure. *Journal of Polymer Science: Polymer Chemistry Edition* **1978**, *16*, 2085–2087.
- Wang, C.; Li, G.; Guo, R. Multiple Morphologies From Amphiphilic Graft Copolymers Based on Chitooligosaccharides as Backbones and Polycaprolactones as Branches. *Chem. Commun.* **2005**, 3591–3593.
- Wang, F.; Lai, Y.-H.; Kocherginsky, N. M.; Koster, Y. Y. The First Fully Characterized 1,3-Polyazulene: High Electrical Conductivity Resulting From Cation Radicals and Polycations Generated Upon Protonation. *Org. Lett.* **2003**, *7*, 995–998.
- Wu, P.-T.; Xin, H.; Kim, F. S.; Ren, G.; Jenekhe, S. A. Regioregular Poly(3-Pentylthiophene): Synthesis, Self-Assembly of Nanowires, High-Mobility Field-Effect Transistors, and Efficient Photovoltaic Cells. *Macromolecules* **2009**, *42*, 8817–8826.
- Xin, H.; Kim, F. S.; Jenekhe, S. A. Highly Efficient Solar Cells Based on Poly(3-Butylthiophene) Nanowires. *J. Am. Chem. Soc.* **2008**, *130*, 5424–5425.
- Yamaguchi, Y.; Ogawa, K.; Nakayama, K.-I.; Ohba, Y.; Katagiri, H. Terazulene: a High-Performance N-Type Organic Field-Effect Transistor Based on Molecular Orbital Distribution Control. *J. Am. Chem. Soc.* **2013**, *135*, 19095–19098.
- Yeom, H. R.; Heo, J.; Kim, G.-H.; Ko, S.-J.; Song, S.; Jo, Y.; Kim, D. S.; Walker, B.; Kim, J. Y. Optimal Top Electrodes for Inverted Polymer Solar Cells. *Phys. Chem. Chem. Phys.* **2015**, *17*, 2152–2159.
- Yim, J. H.; Joe, S.-Y.; Pang, C.; Lee, K. M.; Jeong, H.; Park, J.-Y.; Ahn, Y. H.; de Mello, J. C.; Lee, S. Fully Solution-Processed Semitransparent Organic Solar Cells with a Silver Nanowire Cathode and a Conducting Polymer Anode. *ACS Nano* **2014**, *8*, 2857–2863.
- Yu, G.; Gao, J.; Hummelen, J. C.; Wudl, F.; Heeger, A. J. Polymer Photovoltaic Cells: Enhanced Efficiencies via a Network of Internal Donor-Acceptor Heterojunctions. *Science* **1995**, *270*, 1789–1791.

- Zhang, F.; Jespersen, K. G.; Björström, C.; Svensson, M.; Andersson, M. R.; Sundström, V.; Magnusson, K.; Moons, E.; Yartsev, A.; Inganäs, O. Efficiency Enhancement in Low-Bandgap Polymer Solar Cells by Processing with Alkane Dithiols. *Nat. Mater.* **2007**, *6*, 497–500.
- Zhang, K.; Guan, X.; Huang, F.; Cao, Y. Performance Study of Water/Alcohol Soluble Polymer Interface Materials in Polymer Optoelectronic Devices. *Acta Chim. Sinica* **2012**, *70*, 2489.
- Zhang, M.; Drechsler, M.; Müller, A. H. E. Template-Controlled Synthesis of Wire-Like Cadmium Sulfide Nanoparticle Assemblies Within Core–Shell Cylindrical Polymer Brushes. *Chem. Mater.* **2004**, *16*, 537–543.
- Zhou, Y.; Fuentes-Hernandez, C.; Shim, J.; Meyer, J.; Giordano, A. J.; Li, H.; Winget, P.; Papadopoulos, T.; Cheun, H.; Kim, J.; et al. A Universal Method to Produce Low-Work Function Electrodes for Organic Electronics. *Science* **2012**, *336*, 327–332.
- Zieliński, T.; Kędziorek, M. Bisamides Derived From Azulene-1, 3-and-5, 7-Dicarboxylic Acids as New Building Blocks for Anion Receptors. *Chem. Eur. J.* **2008**, *14*, 838–846.